Spring 4-15-2019

Modeling multiphase flow and substrate deformation in nanoimprint manufacturing systems

Andrew Cochrane
University of New Mexico

Follow this and additional works at: https://digitalrepository.unm.edu/nsms_etds

Part of the Engineering Physics Commons, Fluid Dynamics Commons, and the Nanoscience and Nanotechnology Commons

Recommended Citation

Andrew Cochrane

Candidate

Nanoscience and Microsystems Engineering

Department

This dissertation is approved, and it is acceptable in quality and form for publication:

Approved by the Dissertation Committee:

P. Randall Schunk
, Chairperson

Peter Vorobieff

Dimiter Petsev

Roger T. Bonnecaze

_____

_____

_____

_____

_____

Modeling multiphase flow and substrate deformation in nanoimprint manufacturing systems

by

Andrew Cochrane

B.S.E., ME & EE, University Alaska Anchorage, 2012

M.S., NSMS, University of New Mexico, 2013

DISSERTATION

Submitted in Partial Fulfillment of the

Requirements for the Degree of

Doctor of Philosophy
in

Nanoscience and Microsystems Engineering

The University of New Mexico

Albuquerque, New Mexico

May, 2019

Dedication

To you, the reader, that you may read and add to your understanding.

To my mentors, who helped me on to this path.

Acknowledgments

I am grateful to many people for their part in my doctoral experience. Foremost, Randy Schunk, whose instructive feedback on my writing not only made this manuscript possible, but also taught me an understanding of technical composition that I had never before imagined. Randy, besides advising me in the development of this project, made sure I got the chance to present my work at conferences and taught me to engage my audience by telling a story. Kristianto Tjiptowidjojo, whose patience I tested with many questions about Goma and the finite element method, helped me understand how to demonstrate that I value the time of my colleagues by asking good questions. Weston Ortiz, in whose capable hands I leave the maintenance of the Schunk group computer resources, showed me how to find even the most inscrutable of bugs in C code. Discussions with Akhilesh Jain, Roger Bonnecaze and Shrawan Singhal helped me decide what direction to go with the research. The students, faculty and staff of the NASCENT ERC provided an atmosphere of friendly collaboration and a shared vision that illuminated the context of the project. Many people provided thoughtful questions and criticism that helped hone the story in this manuscript: Steve Brueck, Tito Busani, Stefi Weisburd, Rekha Rao, Robert Malakhov, Mahmoud Behzadirad, Preyom Dey, Juan Faria, Xuemei Wang, Daniel Hariprasad, Rich Martin, Andrew Spann, Yang Ban and certainly more.

Modeling multiphase flow and substrate deformation in nanoimprint manufacturing systems

by

Andrew Cochrane

B.S.E., ME & EE, University Alaska Anchorage, 2012

M.S., NSMS, University of New Mexico, 2013

Ph.D., NSME, University of New Mexico, 2019

Abstract

Nanopatterns found in nature demonstrate that macroscopic properties of a surface are tied to its nano-scale structure. Tailoring the nanostructure allows those macroscopic surface properties to be engineered. However, a capability-gap in manufacturing technology inhibits mass-production of nanotechnologies based on simple, nanometer-scale surface patterns. This gap represents an opportunity for research and development of nanoimprint lithography (NIL) processes. NIL is a process for replicating patterns by imprinting a fluid layer with a solid, nano-patterned template, after which ultraviolet cure solidifies the fluid resulting in a nano-patterned surface. Although NIL has been demonstrated to replicate pattern features as small as 4 nm, there are significant challenges in using it to produce nanotechnology. Ink-jet deposition methods deliver the small fluid volumes necessary to produce the nanopattern, and drop volumes can be tuned to what the pattern requires. However the drops trap pockets of gas as they merge and fill the template, and due to relatively slow

gas dissolution, reduce processing throughput. Capillary forces that arise from the gas-liquid interfaces drive non-uniform gap closure and the resulting variations in residual layer reduces process yield or degrades product performance.

This thesis develops reduced-order models for fluid flow and structural mechanics of the imprint process for NIL. Understanding key phenomena of gas trapping and residual layer non-uniformity drives model development to better understand how throughput and yield can be improved. Reynolds lubrication theory, the *disperse* type of multiphase flow, and a lumped-parameter model of dissolution unite to produce a two-phase flow model for NIL simulations of 10,000 drops per cm^2. Qualitative agreement between simulation and experiment provides a modicum of validation of this model for flow in NIL simulations. The two-phase model simulations predicts that both dissolution and viscous resistance affect throughput.

The coupling of a reduced-order model for 3D structural mechanics with the two-phase flow model enables simulations of drop merger on a free-span tensioned web. Challenges in improving the structural model lead to formulation of a 2D model for which sources of instability are more easily discovered and understood. Inextensible cylindrical shell theory and lubrication theory combine into a model for the elastohydrodynamics of a rolling-imprint modality of NIL. Foil-bearing theory describes the lubrication layer that forms between a thin, tensioned web moving past another surface. Reproduction of the results of foil-bearing theory validates this coupled model and reveals a highly predictable region of uniformity that provides low shear stress conditions ideal for UV-cure. These results show theoretical limitations that are used to construct a processing window for predicting process feasibility.

Contents

CONTENTS

List of Figures

Chapter 1

Introduction

Iridescence is an optical effect that can be described as the change of color with viewing or lighting angle and is a consequence of thin-film interference or diffraction patterns that are created when nano-featured structures interact with light waves. Figure 1.1 shows examples of iridescence and demonstrates an example of nano-featured patterns found in nature. While optical nanotechnology can be engineered
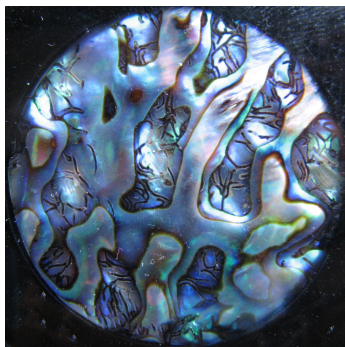
(a) Polished abalone[110].

(b) Golden Stag Beetle. Photographed by Fir0002/Flagstaffotos[45].

Figure 1.1: Examples of natural iridescence

by design of the nanoscale constitutive patterns to produce useful optical effects, many other types of nanotechnology can be like-wise designed around chemistry or other physics at the nanoscale. However, commercial production of materials and devices that take advantage of such nanoscale designs requires a cost model that can be met with only high-throughput manufacturing processes. In this thesis, predictive models for process design and scale-up are pursued as a means of accelerating adoption of commercially viable nanotechnology.

Nanotechnology, as defined by the National Nanotechnology Initiative, is the manipulation of matter at the nanoscale, a context in which at least one spatial dimension is between 1 nm and 100 nm. Many tools are available to produce minute samples of nano-featured material. The scanning electron microscope (SEM) is one such tool that can directly write patterns by a milling process, knocking away material atoms at a time, by blasting the working piece with electrons that have been accelerated to high speeds. Unfortunately the serial nature of these tools poses an significant barrier to using them to efficiently produce large areas of nano-patterned surfaces. Imagine carving Mount Rushmore with a single pickaxe.

The challenge addressed in this work is the engineering design and development of a manufacturing system called **j**et-and-**f**lash **i**mprint **l**ithography (J-FIL) that can produce nano-patterned material for commercially viable enterprises. Roll-to-Roll (R2R) production lines achieve high material throughput by implementing continuous processes that convert an unprocessed roll of material into a roll of new material, like paper becoming newspaper in a modern printing press. A R2R modality of the J-FIL process, similar in form to the creation of newsprint, is envisioned as a new high-speed and low-cost patterning process for nanotechnology production. The level of precision necessary for such a process is attainable only with rigorous engineering design supported by accurate physics-based models. The goal of this work is to produce a process simulator created from models of fluid and structural mechanics.

The development of manufacturing-scale processes requires the concerted organization of both experimental development and physics-based design. Modern industry cannot afford classic 'Edisonian' approaches to process development because the many necessary experimental iterations are time intensive and monetarily exhaustive. So a tradition of process modeling has matured as production cycles have shortened and product specifications have become more precise[62]. As with laboratory device discovery, physics-based design approaches have made countless contributions (e.g. [69] [103] [89] [101] [14] [23] [107]) to the state-of-the-art of manufacturing processes from which the discipline of manufacturing engineering[1] has emerged. Physics-based design principles are developed by iteratively comparing computer simulations built from physical models against experimental process visualizations. This will be the subject of Chapter 2. The rest of this chapter conducts a limited overview of nanoscale phenomena and the advance of industry towards high-volume nanotechnology production.

1.1 Overview of Nanoscale Phenomena and Nanotechnology Industry

This chapter provides a review of manufacturing approaches that are related to or support J-FIL, as a context for subsequent model development. This review reveals the roots of production challenges which are addressed in the subsequent chapters. Moreover, examples of nanoscale phenomena in nature are presented to demonstrate some of the potential of nanoscale phenomena if available in high volume and at low cost. An exemplar device demonstrates that a simple construction can benefit a vast market if it can be produced efficiently.

---

[1]for example the Masters in Manufacturing Engineering at UNM. http://mfg.unm.edu

Chapter 2 presents a variety of flow modeling approaches that leads up to a novel model for flow in production. Analysis of the ideal process reveals that flow in J-FIL must account for the high viscosity difference between gas and liquid and dissolution of the former into the latter. Several different model implementations lead to an expedient computer model that captures two-phase flow properties and gas trapping effects. Experimental process visualizations as well as previously validated model results demonstrate a degree of validation of the flow model.

Chapter 3 gives an account of the development of models for substrate structural mechanics. The successful coupling of a structural model with the two-phase flow model and the implementation of this coupled model predicts an exciting possibility for improving the J-FIL process.

1.1.1   Nanoscale phenomena

The idea of nanotechnology may have been first popularized by a famous contemporary physicist, Richard Feynman, who during the winter break of December 1959, in a dinner talk about the future directions of scientific study, spoke about opportunities at the nanoscale. "When we get to the very, very small world - say circuits of seven atoms - we have a lot of new things that would happen that would represent completely new opportunities for design[44]." To a practicing engineer today, it seems obvious how different design at this scale would be, but to the layman, it might not be so plain. Physical effects linked to quantization of energy, interactions with light and chemical stability are just a few subjects to consider, and those hardly address the means of constructing the circuit of seven atoms.

In the nearly 60 years since Feynman gave this talk, the highly interdisciplinary field of nanoscience has begun to unravel the design choices that emerge when designing at this small scale, exposing many ways that macroscopic material behavior

is influenced by seemingly subtle nanoscale changes. Material features with characteristic lengths on the order of 10-100 nanometers interact with light in remarkable ways, affecting the reflectivity, transmissivity and absorptivity of a material or surface, for instance the thin-film of oil on water in Figure 1.2. Mass and volume are

Figure 1.2: Thin film of oil floating on water[82].
For this iridescent oil stain, the color of the reflected light is a result of constructive interference of light waves in the oil film. The color that is observed is controlled by the film thickness, the angle of incidence of the light source and the viewing angle.

directly proportional to length cubed, so properties like inertia and effects of gravity are dominated by surface forces as size shrinks. *Surface roughness* takes on a whole new meaning at the nanoscale because atoms that make up surfaces create an unavoidably rough surface, consequently motion control systems like screws and hinges that rely on smooth contact are no longer ideal. Piezo-electric materials, capacitive combs, and thermal chevrons are used for motion actuation while compliant mechanisms are used for kinematic control. Because of the challenge and complexity of designing at the nanoscale, the practice of copying biological nano-systems, called biomimetics, is an effective shortcut to attaining the nano-structure that supports complicated material behaviors found in nature. But to produce systems that take advantage of nanoscale phenomena which have not been observed in nature, engi-

neers use mathematical models that aggregate nanoscale systems over large areas to predict their macro-scale effects.

1.1.2   Producing Nanotechnology

Today nano-patterning is used primarily in the semiconductor industry to pack as many transistors onto as small a surface as possible. The incredible pace of this industry has advanced the optical lithography techniques and equipment precision to a level where they can produce complicated 3D nano-devices that require many aligned patterning steps. The expense and the limited production rate pose a barrier for using these systems to produce simple materials. As nanoscience has exposed new possibilities in advanced, nano-patterned materials, a gap in mass production capability has also appeared, where nano-enabled materials are wanted in greater volumes than semiconductor devices yet with less feature complexity.

Devices like optical films, solar panels, batteries, antennas, organic semiconductor devices can be manufactured on cost-effective and flexible substrates. Some of these devices merely improve with nano-patterned complexity, but for those optical films that depend on having sufficient substance to interact with light, the thin, flexible form will require nano features to overcome minimum thickness requirements[79]. To be competitive in their markets, these devices-loaded products must be low-cost and available in large quantities. Since the cost of optical lithography techniques is often excessive for producing these products, interest has arisen around nanoimprint lithography.

Nanoimprint lithography is the transfer of a nanopattern from a template onto a substrate by direct contact with a mediating pattern transfer fluid. The fluid takes the negative shape of the pattern and is solidified thermally or by polymerization with ultraviolet illumination. Low viscosity photo-polymerizable etch resists enables

NIL to replicate nanopatterns over larger 1-10 cm^2 areas at low cost. For many applications, the thickness of the patterned material must be on the order of the feature size, and so follows a broad overview of thin-film manufacturing processes, to provide some context on the relative limits of nanomanufacturing processes.

1.2   Thin-Films

Perhaps the simplest nano-enabled material is a thin-film, like the oil film in Figure 1.2. A thin-film is a layer of material that can be as thin as a single atom.

Thin-films are essential in many industries. Protective coatings, adhesive layers, optical films, magnetic films, and even decorative patterns are all functional thin-film coatings. Produced at a smaller scale, thin-films are also the basis for many high-technology materials, such as semi-conductor devices including integrated circuits, laser components, LEDs and quantum dot containing films. The disparity in precision of layer thickness has led to bifurcation in industry where traditional process that have been the subject of years research and development are forgone for new technologies that sacrifice processing rate for enhanced precision. There are many ways to produce thin films, but not all are equal.

1.2.1   Liquid Coating and Roll-to-Roll Processes

The liquid film coatings industry employs roll-to-roll (R2R) processes in which liquid is metered into a film and then solidified onto a substrate as it is wound from one roll onto another. These process can be performed at extraordinary speeds of up to 10's of meters per second. Partly because of their speed, R2R processes high-throughput production and associated lower cost enable their product markets. There are many ways to accomplish the fluid deposition necessary for R2R coating processes, includ-

(a) Slot-Die Coating

(b) Kiss Coating

(c) Gravure Coating

(d) Dip Coating

(e) Knife Coating
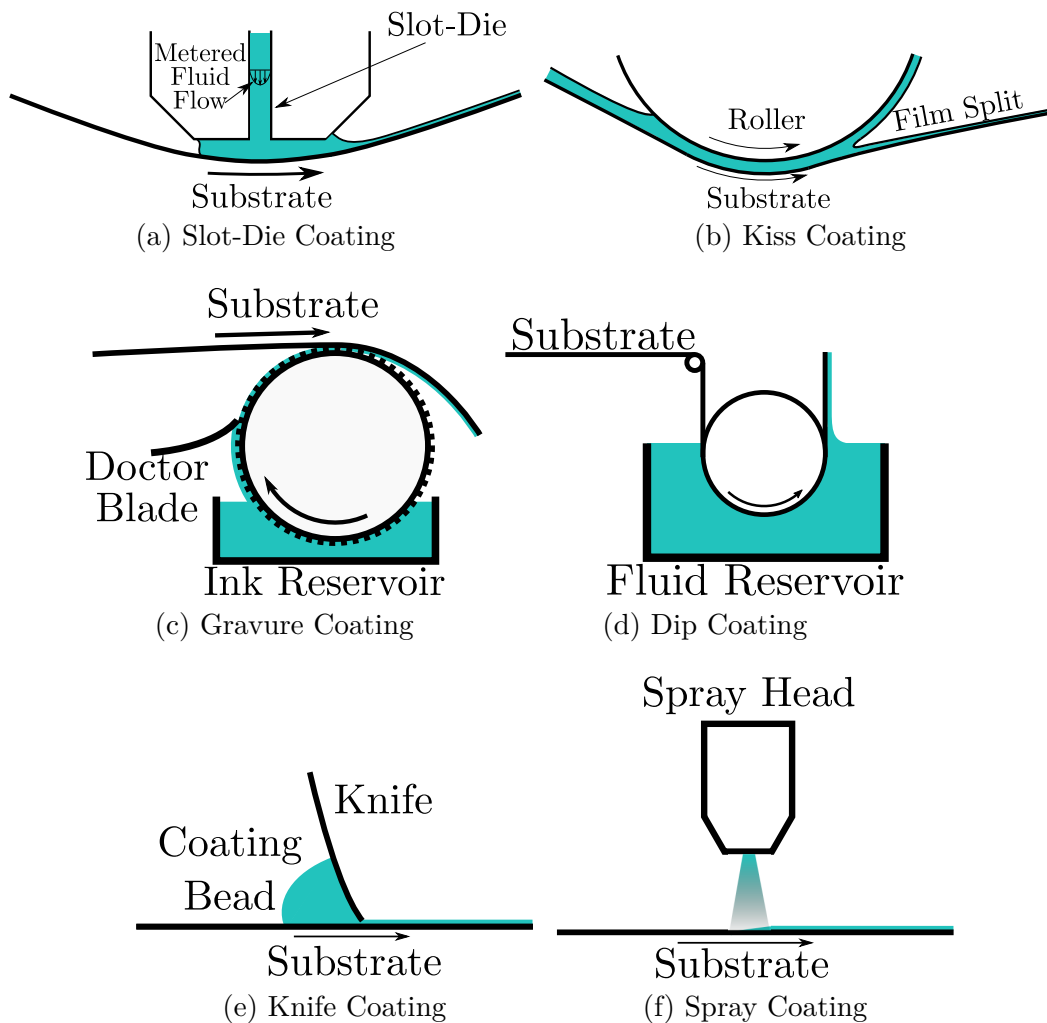
(f) Spray Coating

Figure 1.3: Several process types used for liquid film coating.

ing but not limited to slot-die coating, kiss coating, gravure coating, dip coating, knife coating and spray coating, all shown in Figure 1.3. A recent review of R2R processes reports that state of the art of advanced micro-gravure is capable of generating dry films as thin as 20 nm using highly engineered liquid for a specific application in sensors[86]. Typically these processes create wet films with thicknesses in the 10-100 micron range, which generally dry to 1-10 micron thick coatings depending on the solid content or curing species load. New devices based on nanoscale effects continue

to specify thinner and thinner films[60] beyond which are typically achievable in this high-speed R2R systems.

1.2.2   Nano-Thin Film Coatings

For nano-thin film applications, physical deposition techniques have been refined to specific processes like atomic layer deposition (ALD) and molecular beam epitaxy (MBE). At the very minimum of achievable thickness, ALD is used for layer thicknesses that require atomic precision, shown by schematic in Figure 1.4b. Atomic
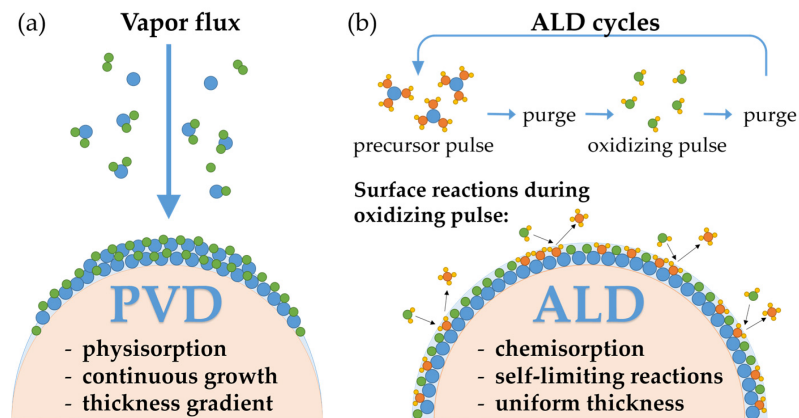
Figure 1.4: Comparison of physical vapor deposition to atomic layer deposition. Image in print[88].

layer deposition (ALD) can be achieved in systems that deliver the material to the surface as a gas but chemically limit deposition by alternating the chemical atmosphere. MBE, shown in Figure 1.5, evaporates a material towards a substrate where the material then deposits at highly precise rates. Both of these processes rely on environmental conditions other than air at standard temperature and pressure so they require complicated atmospheric control apparatus. While both MBE and ALD have been extended to R2R modalities, they are typically much slower than traditional R2R deposition techniques. Liquid coating methods produce nanotechnology
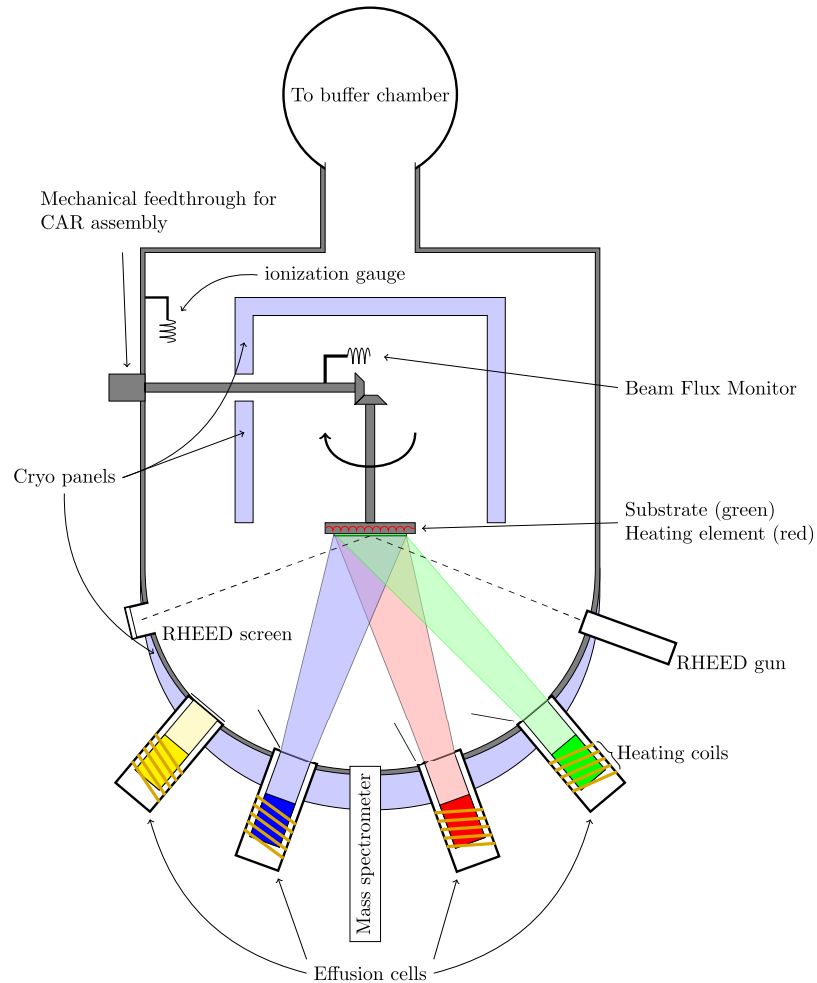
Figure 1.5: MBE schematic[84]

by including nano-dots, nano-rods, nano-tubes, or nano-sheets in the solutions they deposit. So state-of-the-art coatings techniques can produce nano-enabled films. However, lack of patterning limits functionality because patterns enable the higher order complexity that is necessary for useful devices. The potential for nano patterning is discussed next to motivate the development of a high speed nano-patterning process.

1.3 Nanopatterning

(a) Blue Morpho Butterfly[72]
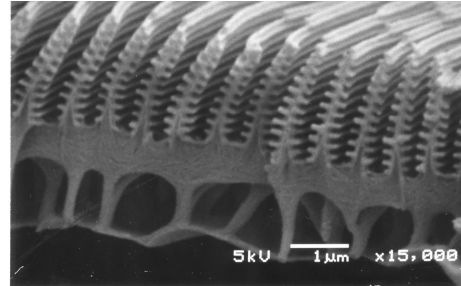
(b) Nanostructure of Blue Morpho Butterfly Wings[118]

Figure 1.6: Nano-featured structure provides *structural color* to the wings of the blue morpho butterfly.

A nano-featured pattern can be included in a thin coating as a step in creating nano-enabled materials that have more specific macroscopic attributes. A compelling example from nature is shown in Figure 1.6a. The iridescent blue color of morpho butterfly wings is a direct result of the nanostructered surface in Figure 1.6b. The color of a nano-featured material is directly related to the optical property of reflectance, and nano-structures can be designed to imbue the material with very specific optical properties.

In mobile computing, electrical power is consumed by many systems, but displays are one of the largest power consumers. Applying optical nanotechnology to the display systems can save power in the case of some light emitting diode (LED) based panels. Backing mirrors that are placed behind active-matrix organic LED (AMOLED) improve how the emitted light is directed, but they also reflect light from the environment, reducing the contrast quality of the screen[57]. A circular polarizer on the viewing surface achieves an anti-reflection effect because the circular polarizer prevents the circularly polarized, reflected light from passing back through it[57].

The circular polarizer is made up of a wiregrid polarizer and a quarter wave plate. Conventionally, a chemical technique creates atom-scale wiregrid polarizers from charge-carrier laden polymers, stretched and aligned by thermal annealing[106]. These conventional wiregrid polarizers absorb a significant fraction of emitted light that would otherwise enhance the display efficiency[106]. So an opportunity to improve display performance arises in the production of wiregrid polarizers that absorb less light. The wiregrid polarizer requires a much simpler structure than that of the blue morpho butterfly wings, and can be produced by a process called nanoimprint lithography.
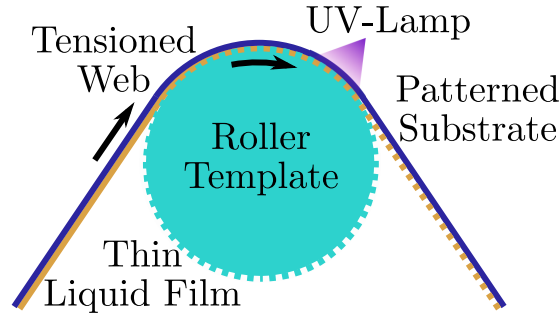
Figure 1.7: Schematic diagram of roll-to-roll nanoimprint lithography.

Nanoimprint lithography (NIL) patterns a substrate by direct contact between a nano-featured master template and a pattern transfer material. To transfer a nano-featured pattern, the master template is imprinted into a fluid transfer material, forcing the transfer liquid to form an interface with the master. The transfer material is solidified then the master is removed, leaving behind a solid, nano-featured layer of transfer material on the substrate. A rolling imprint modality of NIL is show in Figure 1.7.

Jet-and-Flash Imprint Lithography (J-FIL) is a particular form of NIL, in which the pattern transfer material is a photoresist and is deposited onto the substrate by a precision inkjet system. Photoresist is a chemical solution that solidifies when a light-initiated chemical reaction cause the monomer elements to polymerize. Because

of the monomers low molecular weight and the low-viscosity solution, they can flow into nano-features with critical dimensions as small as 4 nm[74] without significant pressure.

Nanopatterning is an essential step in creating materials with structure at the nanoscale; however, it is unusual that a layer of nano-patterned cured photoresist is a useful device. For some applications, like semiconductor processing, the pattern may be used as a mask to etch or dope the substrate, while for other applications, the pattern may be used as a foundation, built upon by subsequent processing steps. As such, nano-patterning processes must be designed to be incorporated with other processing steps so they can be used to create useful components or devices.

Sreenivasan[112] outlined several high volume manufacturing applications of J-FIL and detailed their characteristic feature size, precision, and speed requirements. Among them are next generation display components, higher density storage media, computer processors and memory, hybrid materials for novel nanoscale switching circuits, and even biomaterials for drug delivery. The required feature sizes range from 20 nm to 50 nm, alignment precisions range from 3 nm to 5 μm and throughput ranges from 20 wafers per hour (WPH) to 600 WPH or 30 shots per hour (SPH) to 2000 SPH. Since these materials are traditionally patterned with optical lithographic techniques, Sreenivasan went on to argue the case for using imprint lithography as the primary process in production.

The semiconductor industry has driven the advance of optical lithography as a patterning process for over 30 years advancing it from patterning discrete semiconductor devices to microprocessors to the latest generation of advanced computer processors that possess nanoscale features[112]. For the semiconductor industry today optical lithographic patterning techniques are the workhorse for manufacturing the processors for desktop computers, smartphones, tablets, super computers and every device that participates in a telecommunications network. The industry relies

on optical lithography to produce ever more advanced processors, but the challenges associated with patterning below the wavelength of light are becoming expensive for even the semiconductor industry to solve[112]. Several alternatives have been identified by the International Technology Roadmap for Semiconductors (ITRS), an organization that tracks technology for the manufacture of semiconductor devices[63]. The ITRS is tracking these alternatives because of a growing chorus that current optical lithography techniques are physically incapable of producing smaller-featured patterns[63]. However the semiconductor industry still keeps finding ways to subvert the physical laws that should restrain optical lithography from advancing the next generation of processors[63]. Nonetheless, the sheer cost of these workarounds has resulted in valid business interest in alternative patterning techniques, dubbed Next Generation Lithography (NGL) techniques[63].

NGL technologies include extreme ultraviolet lithography (EUVL), Directed Self Assembly (DSA), maskless lithography and NIL[63]. Of these, EUVL is the most like traditional optical lithography and so would be the easiest integrated into current fabrication lines[27]. Unfortunately implementation of EUVL is problematic for several reasons, specifically sources have low power and the materials for lenses, resists and masks are onerous to work with[116][115]. Maskless lithography writes the pattern directly with thousands of electron beams simultaneously which provides some speedup, however the key roadblocks are increasing speed without reducing accuracy of pattern placement[63]. DSA achieves small feature sizes for etch resists with lamellar structures of phase separated polymeric materials[63]. In the application of DSA to semiconductor manufacturing, a relatively large guide pattern is printed by some lithography technique so that the lamellar structures form in between, but sufficiently small defectivity rates have yet to be demonstrated[63]. Since NIL works by direct contact, when registering multiple layers overlay is achieved by deformation of template and substrate, but precision is not yet adequate for future critical levels[63]. The direct contact used in NIL require sufficient time to eliminate

associated defects, so both registration and processing rates are key roadblocks for NIL in the semiconductor industry[63] and the work of this thesis aims to address the processing rate challenges.

1.3.1 History of Nanoimprint Lithography

Today, NIL can be achieved by the transfer of nanopatterns from a patterned template directly into a photopolymer film, after which the polymer is cured by an ultraviolet flash. Combining highly precise inkjet systems with NIL and roll-to-roll manufacturing yields products that resemble those of both nano-patterned devices and nano-thin coatings. NIL builds on the basic idea of block printing Technologically, it descends from compact disc (CD) laser lens replication systems and photoresist chemistry.

To reach consumers, a reliable process was needed to create the precise optical systems for cameras and later CD players. Originally applied to the reproduction of flat surfaces for mirrors, replication was used by researchers in Mullard (a brand name of Philips) research labs in England using thermoplastics to recreate aspherical optics[59]. The ultraviolet (UV) curing of photopolymer to produce a high quality lens was first communicated by researchers in the optical engineering department of the Polaroid corporation to produce 6 to 8 lenses per day[42]. Building on the work of Polaroid, researchers in the Philips Research Laboratory in the Netherlands developed a manufacturing process in which the UV curing of a polymer was used to produce aspherical lenses for the Compact Disc system[16]. The Philips process resulted in manufactured lens geometries with a tolerance less than 0.2 µm at a rate of roughly 1 lens per minute, an early instance of the use of UV cured imprint manufacturing with near nanoscale precision. In addition to optical disk systems, these lenses were found in televisions and projectors, and many other devices which have

been broadly integrated into society.

In 1995, the pursuit of a low-cost process for producing nanofeatured patterns led semiconductor device builders in the Electrical and Computer Engineering (ECE) department at the University of Minnesota to mimic the hot-embossing replication process to create nanopatterns in the thermoplastic, poly-methyl-methacrylate (PMMA), using a pattern with 100 nm features[30]. This process requires application of pressures with the potential to damage the template while the features of a patterned template were filled, but it also demonstrated that imprint lithography could be used to transfer patterns onto non-flat surfaces[31]. A partnership between Georgia Institute of Technology and Sandia National Laboratories set about the task of establishing design rules[96][97] for the use of this hot-embossing process. The group demonstrated that changes in temperatures during hot-embossing cause it to suffer from pattern regularity requirements[98], thereby detracting from its manufacturing viability. Furthermore, hot embossing places constraints on types of materials that can be used due to thermal residual stresses that would warp or destroy patterned nanofeatures[112].

Meanwhile, researchers at Philips research laboratory, seeking to further the strengths of the replication process in the semiconductor industry, developed a process that could reliably transfer thin-layer patterns into semiconductors with a photopolymer rather than a thermoplastic[53]. Researchers at the University of Texas at Austin took the process a step further and used the pattern with a dry etch to transfer the pattern into a silicon wafer[3], and would go on to investigate alternative ways to apply the photopolymer to the substrate. In a quest to improve replication speed, they discovered that a large number of small drops would pose much less viscous resistance to the filling of the template-substrate gap[33][34][90]. These advance led to what is now known as Jet-and-flash imprint lithography (J-FIL).

J-FIL is the term coined for NIL processes using drop-on-demand delivery systems or ink-jet heads to dispense low viscosity, UV-curable resist onto the substrate. The fundamental steps of the J-FIL process are controlled dispense of photo-polymer drops via ink-jet, template filling during imprint, UV-cure (flash), and finally separation of the template from the patterned substrate, each depicted in Figure 1.8. Initially J-FIL was used with rigid semiconductor wafers and flat templates in a

| (a) Ink-jet | (b) Pattern Fill | (c) UV Cure | (d) Lift-off |
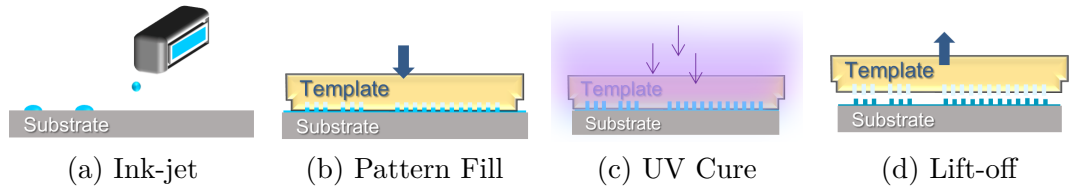
Figure 1.8: Schematic diagram of jet-and-flash imprint lithography (J-FIL), integrable with wafer-scale/roll-to-roll processes. **(a)** Photoresist applied to substrate via precise ink-jet. **(b)** Photoresist drops merge and fill patterned template. **(c)** Photoresist is cured with ultraviolet light. **(d)** Template is separated from patterned template.

stepping fashion [108].

| (a) Step-and-Repeat | (b) Basic | (c) Wrapped | (d) Belt |
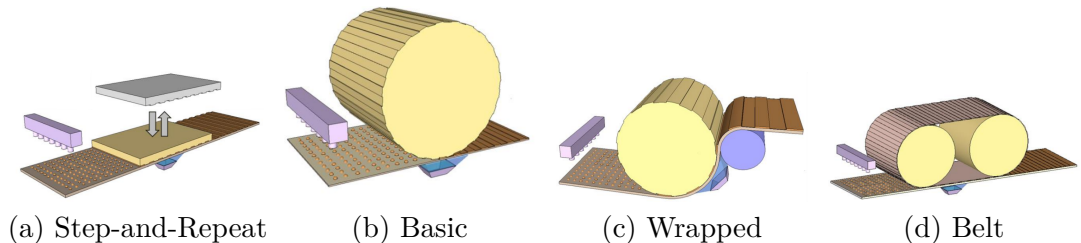
Figure 1.9: Schematic diagram of J-FIL modalities. Reproduced from *Akhilesh Jain's dissertation*. **(a)** A flat pattern is pressed into a tensioned web or flat substrate. **(b)** A patterned cylinder imprints a flat substrate. **(c)** A tensioned web is wrapped around a cylindrical imprint roll. **(d)** A patterned belt is pressed against a tensioned web or flat substrate.

J-FIL Modalities For incorporation into R2R processes, the J-FIL process can be implemented in one of several modalities. Figure 1.9a shows that patterns on flat surfaces can be used to imprint a web by a step-and-repeat process. The roller may be patterned so that the web can be imprinted by a cylindrical mold as shown in Figure 1.9b. To improve the throughput of the process the web can be wrapped around the roller as in Figure 1.9c. Further increase of throughput may be achieved by use of a patterned belt as in Figure 1.9d, providing increased imprint time over the wrapped mode for equal web speeds. These modalities are explored in greater detail by Jain[11]. To expedite the development of an efficient computational model of J-FIL, it helps to break the process into three separate physical regimes, feature-fill, UV-cure and separation. Figure 1.10 depicts the breakdown.The key physics and
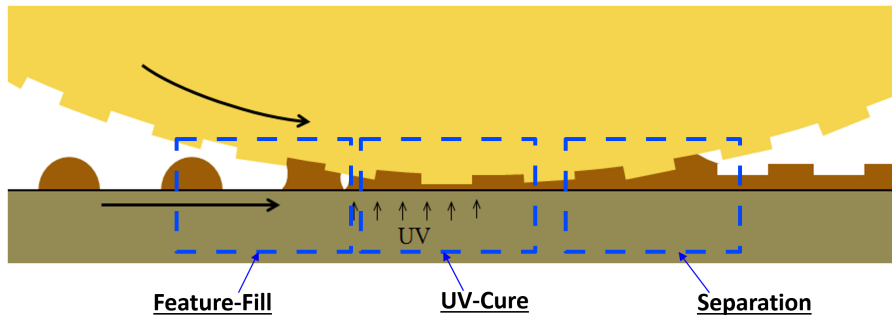
Figure 1.10: Three physical regimes of NIL. Liquid drops merge and fill the pattern in the feature-fill regime. The photoresist is exposed to UV light and cured in the UV-cure regime. The crack between the solid material and the template is propagated toward the confined UV-cure region in the separation regime.

physical phenomena underpinning the feature-fill regime include capillary hydrodynamics, substrate deformation, two-phase flow, gas diffusion and template filling. During the UV-cure regime, photo-induced polymer cross-linking becomes important along with the associated liquid-to-solid phase change, volume change and the development of residual stresses. During the separation process, stiction forces between the mask and substrate become important and the deformation of features due to both the separation forces and the residual stresses can alter the shape of the

nanofeatures. Jain[64] provides a more detailed description of each regime as they pertain to several roll-to-roll configurations.

The vision for J-FIL is to use it to produce the nano-featured patterns in films thin enough to meet semiconductor device needs. Ideally, structures will be mass produced on either rigid or flexible substrates at standard ambient temperature and pressure. However challenges persist in its implementation and it is still far from ready to replace conventional photo-lithography processes in semiconductor fabrication plants. The difficulty in achieving nanometer-scale alignment between two centimeter-scale deformable surfaces while imprinting a third medium is extraordinary. Local deformations caused by thermal expansion, viscous drag and compressive stress result in significant local variations in position of both substrate and template. The goal of mastering overlay alignment must be reached before NIL is used for devices that require multi-layer, 3D configurations[8].

J-FIL can be applied more immediately to single layer applications. The goals of faster processing and reduced defectivity are perhaps more readily achieved, but are still not trivial. As the drops merge together they trap gas which must be dissolved to avoid non-fill defects. Still other sources of defects exist. Investigation into defect root causes have revealed two defect pathologies of random defects and repeater defects[108]. Random defects do not repeat and manifest in the film by a one-time non-fill defect. Repeater defects are observed with every repetition of the imprint process. Defects that originate during imprint of the photoresist can be attributed to damage of the template, infiltration by contaminants or incomplete gas dissolution. Damage to the template most often arises due to repeated contact with the substrate over time. The issue of template damage can be mitigated by imprinting a set of daughter templates from the expensive mother template[104]. Contaminants can be introduced to the process through either the photoresist or the environment and then deposit either onto the template or into the patterned substrate. In any case,

prevention of gap closure by large contaminants leads to non-fill defects. A smaller contaminant may become lodged in the template and locally prevent filling also leading to non-fill defects. The manufacturing equipment has been identified as a likely source of such contaminants[108], and care must be taken in the equipment design to minimize such threatening particle detachment.

Once particle-related defects are minimized, defects related to the natural evolution of the process are identified. Once the resist has cured, a residual layer of material is left between the template and substrate and is not part of the pattern. If the pattern is to be used as an etch mask, the residual layer thickness (RLT) uniformity is of key concern and can affect the etch uniformity. Such non-uniformity will at best diminish the quality of the product or at worst make it completely unusable. The use of drop-on-demand technology and flexible materials aggravates the pursuit of a uniform RLT due to the increased influence of capillary action. Since this residual layer is formed as the drops merge together, a model of the drop merger process is developed to guide process engineering efforts. As the drops merge together they trap gas, which must be dissolved before curing or otherwise the gas pockets will result in relatively large patches of unfilled template and uncovered substrate. The current method for addressing these issues is to control the processing rate, thus providing precise timing for the residual layer to become uniform and for the trapped gas to dissolve[68][109][2]. The models developed in Chapters 2 and 3 of this thesis will provide guidance for process design.

1.4 NASCENT

The National Science Foundation (NSF) has instituted a nanosystems engineering research center (NERC) for the creation of **na**nomanufacturing **s**ystems for mobile **c**omputing and **en**ergy **t**echnolgies (NASCENT). NASCENT is a collaboration be-

tween several Universities including the University of New Mexico and the University
of California at Berkeley and is led by the University of Texas at Austin. The vision
of the NERC is to provide resources needed to bridge the technology valley of death
(Figure 1.11) that lies between nanotechnological proof-of-concepts developed in a
public, academic context and successful technology commercialization by a company
in the private sector. Therefore, the primary products of NASCENT are small-scale,
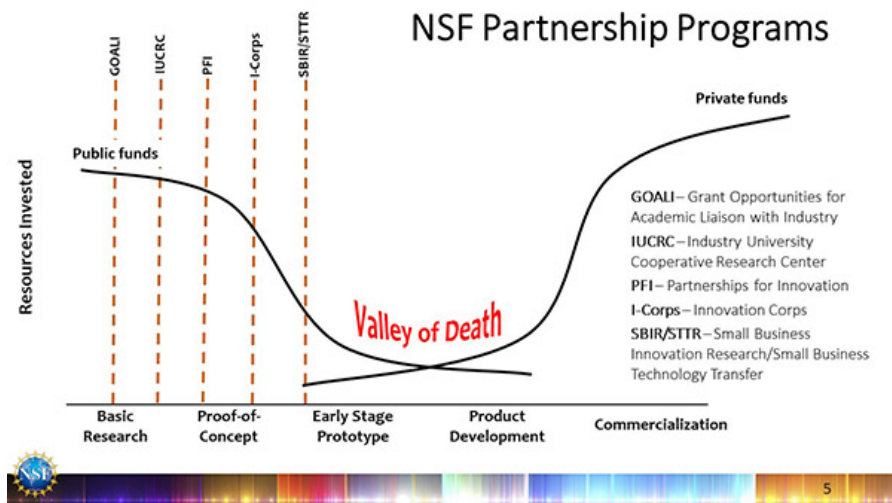
Figure 1.11: NSF viewgraph[35] describing investment over product lifetime, from
initial R & D through commercialization. The mission of the NASCENT ERC to to
reduce costs associated with early prototyping of nanotechnology-based devices by
providing facilities and expertise for designing commercial manufacturing systems.

NIL manufacturing lines (testbeds) that are equipped with comprehensive metrol-
ogy instrumentation. The testbeds serve as a path to industrial process scale-up for
nano-enabled products base on novel nanotechnology Research thrusts of the NERC
have been organized to address patterning and functional materials as well as metrol-
ogy and yield enhancement. All efforts within these thrusts are directed to support
the development of wafer-based and roll-to-roll NIL testbeds. The work of this thesis
supports development of basic knowledge and system level science by computational
modeling fluid and structural mechanics of NIL.

1.4.1 Manufacturing-Scale Simulator

The NASCENT ERC will provide an experiment oriented testbed for third parties to use to develop their processes based on nanoimprint lithography technology. The testbeds developed through NASCENT research will provide a variety of feedback systems for on- and off-line process improvement. The purpose of computational modeling for the testbeds is twofold: first modeling will provide initial insight into the effects of process parameters, and second it can be used to create rule sets for in-line feedback control loops. To this end models are developed and tested against manufacturing scale processes knowledge in support of the production of exemplar devices.

The term *manufacturing-scale* as used in this document refers to the scale large enough to provide meaningful representation of a process suitable for commercial production In contrast, a lab scale process is limited in its capacity to be used for commercially viable production nano-enabled materials or devices. Manufacturing scale simulations will predict macro-scale phenomena that arise in processing due to aggregation of many nano and micro-scale phenomena.

Exemplar devices are used as a case study for development of the testbeds of the NASCENT ERC. These devices unite the research teams in areas of manufacturability, measurement and modeling with common goals of feature size, process parameters and device performance[7]. The devices test the systems capabilities to fabricate nano features as well as the measurement tools performance in measuring those materials. A functional production line built around an exemplar device also enables the success of the NASCENT ERC to meet its goal of providing capability to design manufacturing processes for commercial operations.

The wiregrid polarizer is an optical device that can be fabricated as a thin film, but also requires a nano-featured pattern, they are often used to increase the effi-

ciency of display panels by increasing the transmittance of the panel view-screen[105].
The **w**ire**g**rid **p**olarizer (WGP) can be fabricated in a two step process: first the film
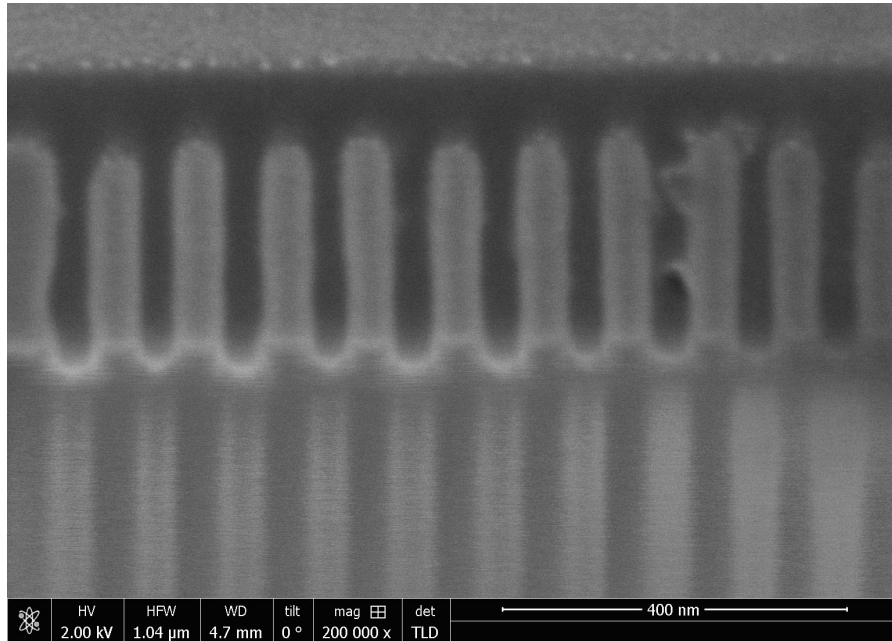
Figure 1.12: Scanning electron microscope cross-section of the imprinted pattern to
be used as the template for a wiregrid-polarizer.

is imprinted with a uniform array of ridges, and second a conductive material is deposited at an angle so that it builds up on one side of the ridges, effectively creating
an array of wires[106]. For the NASCENT ERC, a common WGP design specifies
rectangular ridges with the width of each ridge being 50 nm and the height of each
ridge being 100, where the center to center distance between each plateau is 100 nm.

1.5 Methodology

The purpose of this dissertation is to provide a tool set for increasing the understanding of gas trapping phenomena and the factors that influence residual layer
thickness uniformity through numerical models and computational investigations.

Understanding of key physics of the J-FIL process will guide the determination of the most important operating conditions. The approach is computer-aided modeling by solving partial differential equations governing fluid mechanics and substrate deformation during the imprint stage. The numerical models are rooted in the solution of the differential equations using Galerkin's finite element method (GFEM). Details of the modeling approach and the solution methods are presented in the following chapters. Typical results of the simulator are illustrated in Figure 1.13. Typically fluid

(a) Comparing Fluid Pressure   (b) Merger of Four-Hundred Drops
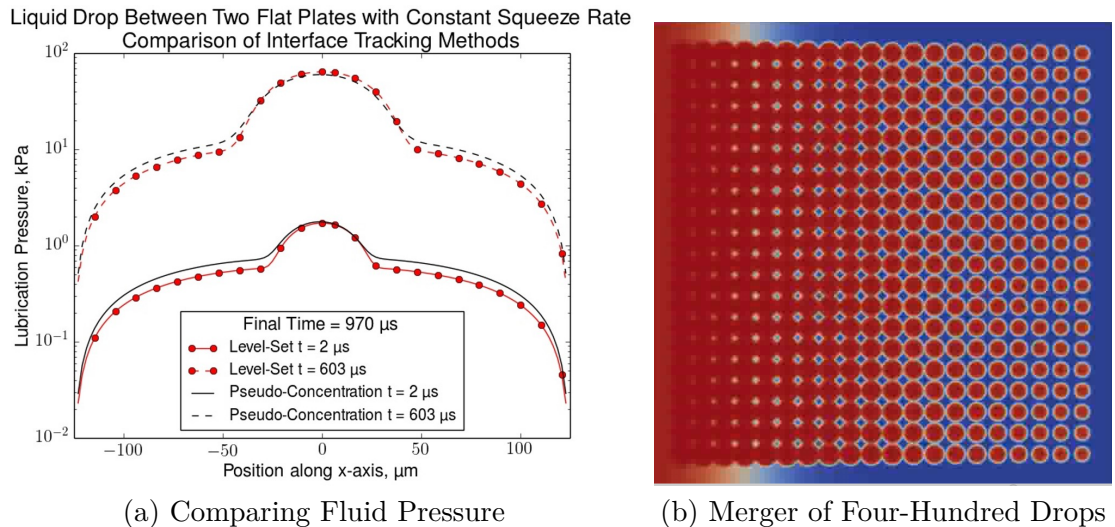
Figure 1.13: Example Simulation Results

mechanics are modeled with the Navier-Stokes equations and structural mechanics are modeled with Cauchy momentum equations and stress-strain constitutive relationships. A comprehensive simulation that implements these equations would entail discretization of nanoscale features over centimeter scale domains, resulting in a system that is, today, computationally expensive and perhaps even intractable. Results must be readily available or attainable for modeling to be relevant in design. There are two paths to such expediency: pre-computing complex models and storing results in a lookup database or reducing model complexity and allowing simulations to be completed with rapidity. While precision, accuracy and completeness of physics are

advantages of complex models, they are hamstrung by computational expense. If a system is to be modified outside of the scope of any precomputed results, designers must allocate significant time and computational resources to attain new results. On the other hand, models of reduced complexity, or reduced-order models, allow studies that modify systems at will. Reduced-order models carry the cost of reduced flexibility, because of the assumptions built-in with the reduced complexity. This increase in flexibility carries a cost that limits the scope of what sort of modification to the model system can be made. To reduce model order, simplifications are made that lump physics together using rigorous scaling arguments, however these simplifications impose an envelope of accuracy that might be pushed by system designers as they use such a tool to understand the process they are designing. This work develops reduced-order models of two-phase fluid mechanics and couples them with reduced-order structural mechanics models. While reduced-order models provide simplified equations for describing a system, the non-ideal geometries of real-life systems require discretization and numerical solution methods.

A numerical analysis software, Goma 6.0[102][2] is used to achieve computational solutions of the reduced order models. Goma 6.0 provides the software architecture and many example implementations of physical differential equations within the Galerkin finite element method (G-FEM or just FEM) framework. Decomposition of the geometry into a finite number of contiguous and non-overlapping elements provides the discretization. The FEM converts continuum partial differential equations to discrete ordinary differential equations (ODEs). Newton-Raphson method linearizes the ODEs into a set of linear algebra equations. Computational linear algebra solves the linearized systems. The solutions are stored in mesh database files. Post-processing software queries the solution databases to generate visualizations of the the results.

---

[2]https://github.goma.io

In any manufacturing process design, the goal is to maximize throughput and process yield. Throughput is the product of processing rate and material width, while yield refers to how much of the processed material meets the finished product specifications. The rate and yield limiting effects of drop merger manifest in the necessity of waiting for trapped gas to dissolve or for the photoresist to flow through the extremely narrow gap. Throughput and yield are typically competing outcomes, because increasing the rate, will reduce yield and vice-versa. Increasing the material width on the other hand is a handy way to increase throughput without changing the rate or yield. The processing equipment will limit the width increase, and so should be planned before the equipment is constructed. Once the equipment is built, the question to answer then is, "how can rate by optimized to maximize yield?" To answer this question, reduced-order models are developed so that the effects of parameter variation on process output can be studied expediently and the most important factors identified. The feature-fill regime is broken down into three distinct problem types; fluid flow in the gap, deformation of the substrate and filling of the features. This separation facilitate development of independent model development for each type, although they do need to be coupled to most fully understand the process. The scope of this dissertation is limited to the fluid flow in the gap and structural deformation problems along with their coupling.

Chapter 2

Multiphase flow model for NIL

2.1 Introduction

The patterning of surfaces with features smaller than 100 nm is of great importance to the printed electronics, semiconductor and related manufacturing industries, in which low-cost production of nanometer-scale features over large areas is necessary to meet evolving market demands[81]. Jet-and-flash imprint lithography (J-FIL)[4], shown in Figure 2.1, is a form of ultraviolet (UV) nanoimprint lithography (NIL)[30], that has been rapidly advanced to meet these demands[53]. Computational modeling of J-FIL is developed here to further advance the understanding of the challenges that remain in its application.

2.1.1 Physical Description

Pictured in Figure 2.1, J-FIL involves the interaction between solutions of photo-active monomer and solvent in a liquid phase interspersed with a gas phase in a thin, closing gap between a substrate and a patterned template[34].

(a) Ink-jet (b) Pattern Fill (c) UV Cure (d) Lift-off
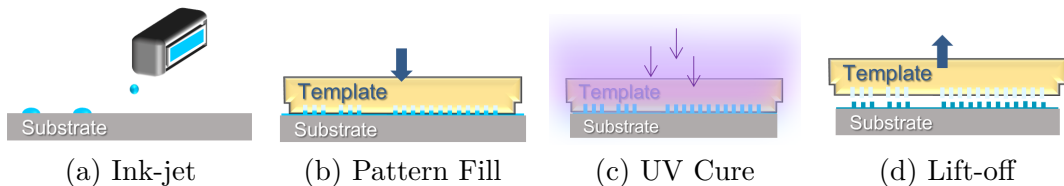
Figure 2.1: Schematic diagram of jet-and-flash imprint lithography (J-FIL), inte-grable with wafer-scale/roll-to-roll processes. **(a)** Photoresist applied to substrate via precise ink-jet. **(b)** Photoresist drops merge and fill patterned template. **(c)** Photoresist is cured with ultraviolet light. **(d)** Template is separated from patterned template.

Figure 2.1a represents the first step of the J-FIL process in which 1000s of radius $\mathcal{O}(10\text{-}100~\text{µm})$ drops are dispensed over relatively large areas $\mathcal{O}(10~\text{cm}^2)$ in non-uniform arrays, registered with the pattern to be imprinted, so as to distribute the liquid where it can efficiently fill the template with minimal waste. The combination of applied pressure and capillary forces exerted by the liquid bridges closes the gap between the surfaces as the drops merge and features fill, depicted in Figure 2.1b.

This process creates a two-phase flow of immiscible fluids in an exceedingly thin $\mathcal{O}(15~\text{nm})$ gap before the liquid fills its designated volume, depicted in Figure 2.2a. Ideally, all gas has been eliminated from the gap, the liquid has filled the tem-

(a) Side View (b) Top View
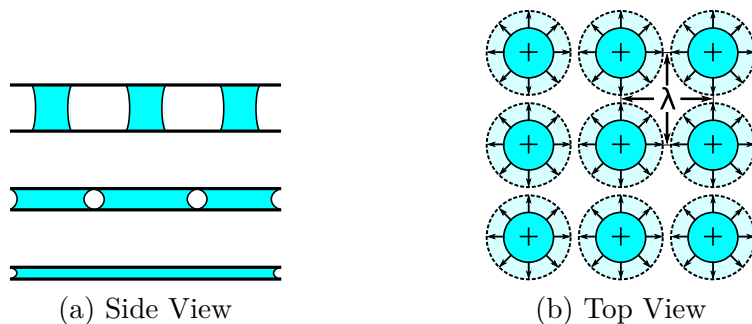
Figure 2.2: **(a)** Side view of drops merging during pattern fill. **(b)** Top view of drop interface evolution during pattern fill.

(a) Pressure profile across a pocket of trapped gas

(b) Pressure induced deformation

(c) Non-uniform residual layer

(d) Uniform residual layer
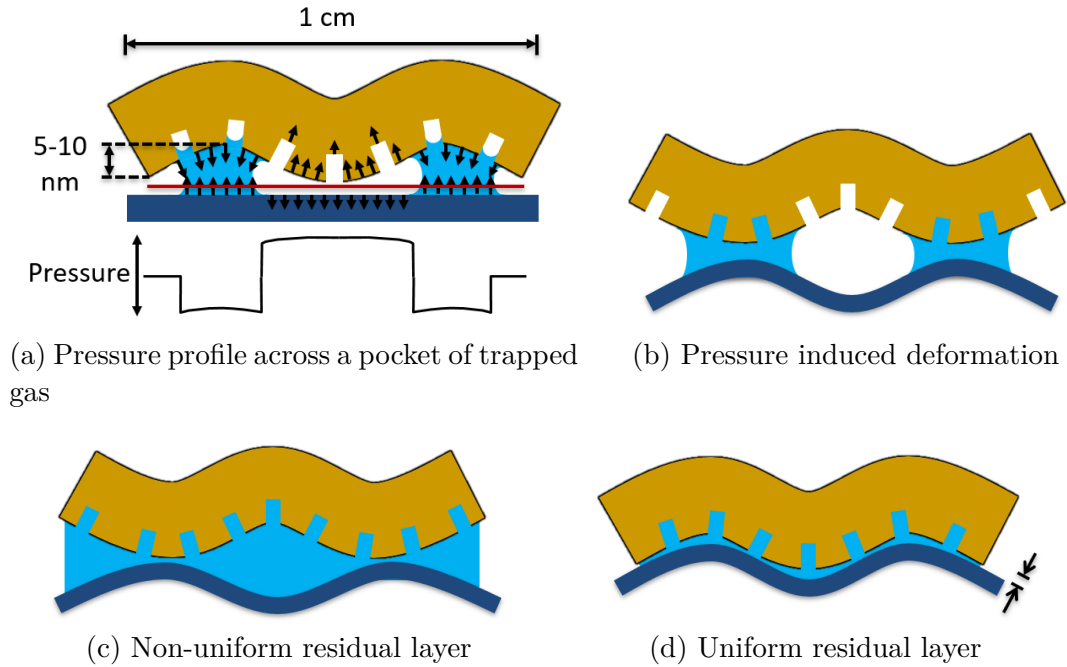
Figure 2.3: Capillary forces and the residual layer thickness.

plate and the residual layer below the features is uniform over the print area before the liquid is cured with UV light[114] (Figure 2.1c). This feature-filling regime of J-FIL includes merger of liquid photoresist drops that are several orders of magnitude larger than the features into which they flow. Low contact angle between the photoresist and substrate allows the drops to spread significantly once deposited. As soon as the drops form liquid bridges between the template and substrate, surface tension forces acting at the gas-liquid interfaces pull the materials together. The viscous resistance increases as the gap shrinks and gas-liquid interfaces evolve to trap gas pockets creating a gas-liquid matrix(c.f. Figures 2.2a, 2.3a). The advancing gas-liquid interfaces compress the gas pockets which locally push the substrate and template apart, depicted in Figure 2.3b. Any trapped gas prevents the liquid from entering the nano-features and causes non-fill defects to occur. With enough time and pressure, the gas dissolves completely into the liquid photoresist, but as in Figure

(a) t = 0 ms : Drops bridge gap

(b) t = 220 ms : Drops trap gas

(c) t = 240 ms : Gas compresses and dissolves

(d) t = 1.26 s : Gas phase eliminated
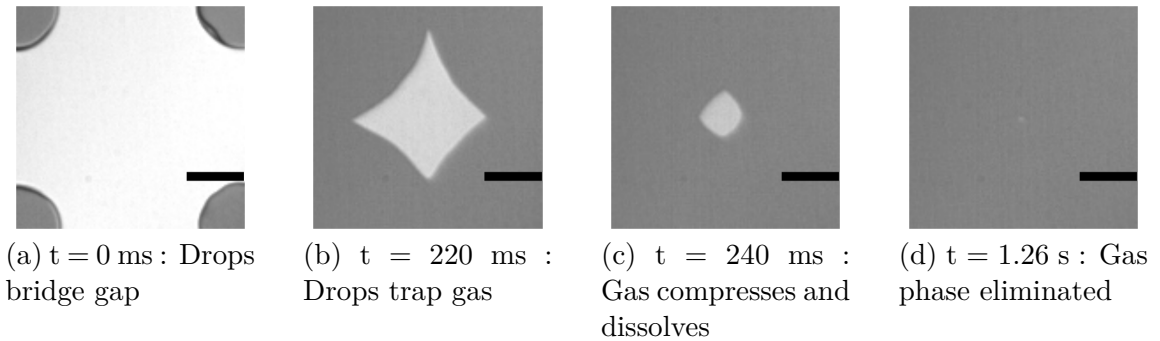
Figure 2.4: Stills captured from high-speed video of drops squeezed between flat plates with 40 µm scale bar. **(a)** The drops bridge the gap between substrate and template. **(b)** The drop edges contact one another, trapping a gas pocket. **(c)** The gas pocket compresses under pressure forces imparted by both applied squeezing and surface tension driven suction between the substrate and template. **(d)** The gas phase has been completely eliminated via dissolution into the liquid volume.

2.3c, the resulting film may not be the ideal uniform thickness as depicted in Figure 2.3d. The model developed in this chapter focuses on the drop merger process of the pattern fill step.

Snapshots from an experimental flow visualization of the process as captured with a high-speed camera,are shown in Figure 2.4[1] The modest motion of the liquid and subsequent motionless confinement of the gas suggests that model development with respect to gas trapping can be separated into stages: First, unconfined gas, and second, gas confinement. Formation of liquid bridges between upper and lower surfaces marks the beginning of the first stage in which the gap volume decreases as the gas flows out of the gap between the drops. Contact of the drop edges with one another marks the beginning of a stage of gas compression, during which, viscous forces in the thinning gap lead to large pressure gradients in the liquid as it displaces the compressing gas. Pressure builds up in both gas and liquid phases to counteract the squeeze forces, reducing the gap closure rate and initiating the gas dissolution

---

[1]Dr. Shrawan Singhal of the University of Texas at Austin, personal communication

stage. The process is slowed by the necessity for gas to diffuse from the gas-liquid interface into the bulk of the liquid. Management of the liquid drop coalescence in the closing gap is critical to process optimization because trapped gas results in non-fill defects or long dwell times. The very thin gaps increase viscous resistance to flow also lengthening dwell times. Smaller drops enable faster drop merger[90] and since inkjet heads can dispense drops as small as 1 pL[65], 100 nm uniform layers can be achieved with optimal drop densities of 10,000 per 1 cm. Since features cannot begin to fill until liquid arrives at their entrances and once they do, capillary action rapidly draws fluid into them,[28] the challenge of modeling the merger of thousands of drops is the primary focus of this work.

This study builds toward a complete predictive model to guide process designs that minimize gas trapping and reduce variation in the residual layer. Expedient model set up and short run times are also desirable so that design and scale-up of the process can be realized. At a minimum, the model requires first a suitable two-phase flow model, capable of scaling up to large flow areas while capturing the aggregate micron-scale effects without computational complexity. As such, trapping of micro-sized gas bubbles, subsequent gas dissolution and diffusion through the liquid phase are the focus of this chapter. This chapter arrives at a mathematical formulation based on multiphase flow concepts that aggregates the micro-size effects of many-drop merger over large areas of varying liquid density and gap thickness. The effects of capillary forces and structural mechanics are left for the next chapter, while flow into template features are left for future work.

2.1.2   Previous Work

Modeling efforts for NIL began after the demonstration that a nano-featured pattern could be imprinted into a layer formed by spin-coating. Colburn et al.[34] assessed

template control schemes with an analytic approach that accounted for both viscous resistance of the liquid phase and capillary forces as a function of gap thickness, gap closure velocity, liquid material properties and drop pattern. Researchers then studied feature filling in order to predict pattern filling times. Reddy et al. [90] extended Colburn's analytic model with a finite difference approach based on volume-of-fluid interface tracking to predict fill times for non-uniform drop patterns.

Researchers then studied the effects of the gas phase with two-phase models. Liang et al. [75] implemented a gas bubble model with the finite difference method that predicts dissolution rate with Henry's law and Fickian diffusion to investigate how thermodynamic properties of the gas effect dissolution dwell times in micron sized features. Roberts et al. [94] formulated a general model for two-phase lubrication of a curvilinear domain, suitable for non-planar flow domains typical of a J-FIL process with structurally flexible templates. Solving the resulting equations with a finite-element based approach, they simulated two-phase gap closure flow with level-set interface tracking. Moreover, Roberts et al. validated results against analytic models for single drop squeeze flow and by accurately predicting evolution of the interface of a single drop as observed in experiment. Section 2.3.1 details the scale-up trial with Roberts model, attempting to simulate drop merger over large areas.

More recently several authors have addressed fluid management in related drop-dispensing, imprint lithography processes. A full three-dimensional, Navier-Stokes, two-phase mixture flow approach was demonstrated by Peng et al.[87] to simulate micro-size bubble formation in micro-size features using the finite volume method. Taylor [6] developed an approach based on contact mechanics that includes imbibition of liquid into the template and the motion of liquid across the substrate and demonstrated that it scales to large areas for process design. Jain et al. [65] advanced a finite-difference, volume-of-fluid (VOF) approach to address the J-FIL process that allows for large area, $(\mathcal{O}(1000))$ drop simulations, but ignores the gas phase.

Nonetheless, this analytical model predicts an NIL parameter envelope wherein gas physics are negligible[66].

Gas Trapping Affects Optimization

While useful process understanding has been gained from these works, no approach accounts for the effects of gas trapping and pressure-driven gas dissolution with a continuum model over practical processing areas of $\mathcal{O}(10 \text{ cm}^2)$. A new approach evolves from the work of others to capture gas trapping and gas dissolution in a multiphase flow formulation that enables large scale (>1000 drops) simulations suitable for iterative process design studies. The analyses of the Saffman-Taylor instability in oil-water flows through sand[117] or fractured rocks[47] provides a significant knowledge-base from which to draw two-phase modeling insights[77].

2.2 Modeling Approaches

This section introduces Reynolds lubrication approximation. An assembly of approaches for modeling the two-phase flow catalogs the the variety of ways that have been used to capture flow of two phases. An account of the process for numerical solution wraps up the process by which models are evaluated for their viability in process design. In essence, this section presents the foundational components that make up two-phase flow simulations of the the NIL process.

2.2.1 Reynolds Lubrication

The small height of standing drops, $\mathcal{O}(1 \text{ μm})$, and large areas necessary for manufacturing processes $\mathcal{O}(10 \text{ cm}^2)$ result in a flow domain of extreme aspect ratio, making a

full three-dimensional multiphase flow model impractical. The extreme aspect ratio of these drops means that the flow will occur in a thin gap, where $h/L \ll 1$. Modeling the flow in a thin gap is made less complex by Reynolds' lubrication theory, that requires also a dynamic constraint that limits the ratio of viscous to inertial forces[92].

$$\text{Re} = \frac{\rho l v}{\mu}, \tag{2.1}$$

where Re is the Reynolds number, l is the characteristic length of the system, v is the characteristic speed of the fluid and ρ and μ are respectively the density and viscosity of the fluid. In this the characteristic length of the system is the gap thickness, $l = h$. The simplifications presented here are derived for cases in which $h\text{Re}/L \ll 1$. More details of this derivation can be found in Appendix A. The full three-dimensional Navier Stokes equations reduce to the following,

$$\frac{\partial P}{\partial x} = \mu \frac{\partial^2 u_x}{\partial z^2} \tag{2.2a}$$

$$\frac{\partial P}{\partial y} = \mu \frac{\partial^2 u_y}{\partial z^2} \tag{2.2b}$$

$$\frac{\partial P}{\partial z} = 0. \tag{2.2c}$$

Here P is the fluid pressure, $\boldsymbol{u}$ is the 3D velocity field and μ is the dynamic viscosity. Take the coordinate system to be that shown in Figure 2.5.

The gap-parallel vectors (represented by the II subscript) are separated from the gap-orthogonal components,

$$\begin{aligned}
\boldsymbol{u} = \boldsymbol{u}_{\text{II}} + u_z \hat{\boldsymbol{z}} = u_x \hat{\boldsymbol{x}} + u_y \hat{\boldsymbol{y}} + u_z \hat{\boldsymbol{z}} \\
\boldsymbol{\nabla}_{\text{II}} = \frac{\partial}{\partial x} \hat{\boldsymbol{x}} + \frac{\partial}{\partial y} \hat{\boldsymbol{y}} \\
\boldsymbol{U}_a = U_{xa} \hat{\boldsymbol{x}} + U_{ya} \hat{\boldsymbol{y}} \\
\text{et cetera}
\end{aligned} \tag{2.3}$$

(a) Thin-gap perspective view showing streamlines around an obstacle.

(b) Thin-gap profile view showing length and boundary velocities. Note: $h \ll L$
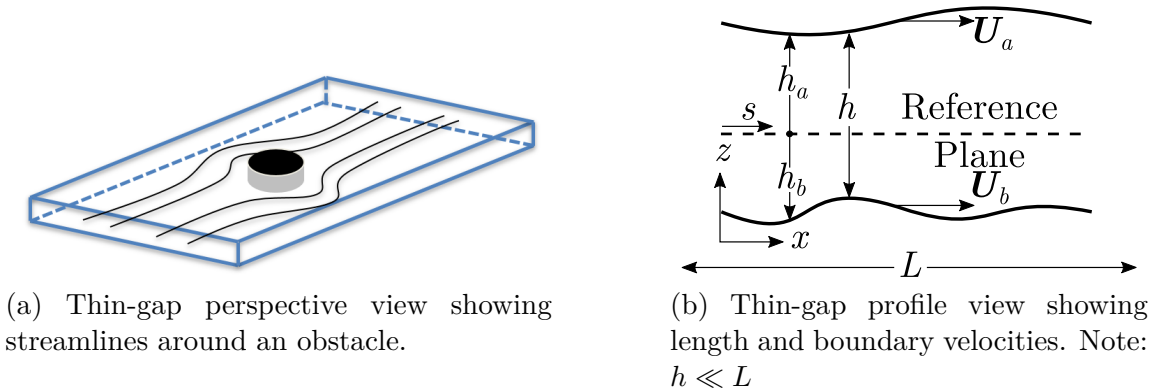
Figure 2.5: Two perspectives of a thin gap

The liquid flux through the gap is is obtained by integrating the continuity equation through the gap thickness after solving Equations 2.2 with the appropriate boundary conditions,

$$\boldsymbol{q} = -\frac{h^3}{12\mu}\boldsymbol{\nabla}_{\mathrm{II}}P \quad + \quad h\frac{\boldsymbol{U}_a + \boldsymbol{U}_b}{2} \ . \tag{2.4}$$

$$\text{Poiseuille flow} \qquad \text{Plug flow}$$
$$\text{contribution} \qquad \text{contribution}$$

The gap average velocity field $\boldsymbol{v}$ is simply,

$$\boldsymbol{v} = \frac{\boldsymbol{q}}{h}. \tag{2.5}$$

This procedure also provides a simple expression relating the boundary motion and the flow in the gap to the pressure field,

$$\frac{\partial h}{\partial t} + \boldsymbol{\nabla}_{\mathrm{II}} \cdot \boldsymbol{q} = 0. \tag{2.6}$$

Reynolds lubrication approximation provides model order reduction by limiting the 3D Navier-Stokes equations to flow in thin gaps. A model of drop merger will require treatment of the two separate fluids that flow in the gap simultaneously and the next section explores some of the many approaches have been developed to model *two-phase flow*.

2.2.2 Two-Phase Flow

A two-phase model with a clear description of the interface is necessary to capture the interfacial forces and individual phase flow in the J-FIL process. Free and moving boundaries are ubiquitous in technologically important problems and many numerical methods for capturing such boundaries have been developed[22]. Numerical methods for free boundary problems are typically divided into two groups, Eulerian and Arbitrary Lagrangian Eulerian (ALE), based on how the interface is tracked relative to the discretization of the domain. Eulerian methods track the interface independently of the discretization, allowing the interface to move across discretization points. ALE methods track the interface by constraining all points of discretization along the interface to move with it. In the droplet merge regime the shape of the interface changes dramatically, therefore approaches that use ALE interface tracking methods would suffer from excessive mesh deformation and lead to poor distribution of discretization points without frequent re-meshing. Consequently, the scope of work is reduced by considering only Eulerian interface tracking methods.

Modern Eulerian methods for simulating two-phase flow in thin-gaps have evolved from a large body of work including: studies of flow in pipes[77], investigations of the Saffman-Taylor instabilities[100], mercury porosimetry[80][51], studies of porous media[119][24], investigations of flow in fractures[47][46] and the of improvement of accuracy in simulations that capture the effects of large interfacial forces[17][49].

Mass Balance for Each Phase

One class of thin-gap two-phase flow models is structured around a classic approach to two-phase Darcy flow[12]. A mass balance equation is formulated for each phase:

$$\frac{\partial(h\rho_l S)}{\partial t} + \boldsymbol{\nabla}_{\mathrm{II}} \cdot (h\rho_l \boldsymbol{v}_l) = 0 \qquad \text{(Conservation of Liquid Mass)} \qquad (2.7)$$

$$\frac{\partial(h\rho_g(1-S))}{\partial t} + \boldsymbol{\nabla}_{\mathrm{II}} \cdot (h\rho_g \boldsymbol{v}_g) = 0. \qquad \text{(Conservation of Gas Mass)} \qquad (2.8)$$

Here, h is the gap thickness, ρ_α is the bulk density of phase α, $\boldsymbol{v}_\alpha$ is the two-dimensional gap-average velocity vector for phase α and S is the saturation, a local measure of the ratio of liquid volume to gap volume. The distinction between phases is made by changing the subscript α; g refers to the gas and l to the liquid. The velocities are described by, with addition of the Darcy permeabilities, k_α,

$$\boldsymbol{v}_l = -\frac{h^2}{12\mu_l} k_l \boldsymbol{\nabla}_{\mathrm{II}} P \qquad \text{(Darcy Potential Flow of Liquid)} \qquad (2.9)$$

$$\boldsymbol{v}_g = -\frac{h^2}{12\mu_g} k_g \boldsymbol{\nabla}_{\mathrm{II}} P. \qquad \text{(Darcy Potential Flow of Gas)} \qquad (2.10)$$

In this approach, P is the local pressure, and μ_α is the bulk viscosity of phase α. The Darcy permeabilities are structured such that each equation is active only in regions that contain the corresponding phase. Furthermore, there are various ways to augment this formulation in order to capture different physical effects. Dual pressure fields, P_l and P_g, and a constitutive equation relate the pressure difference to the capillary pressure jump as well as the deformation of the porous media (c.f. Cairncross et al.[24]). Another approach retains the single pressure field, but specifies the Darcy permeabilities based on macroscopic measurements of the pressure required to drive various mixtures of gas and liquid through thin gaps (c.f. Fourar et al.[46]). This class of two-phase flow model is just one candidate for process design modeling.

Total Mass Balance

An alternate class of flow models employs a single equation for total mass conservation and is prototyped in the following set of equations,

$$\frac{\partial \rho}{\partial t} = -\boldsymbol{\nabla}_{\text{II}} \cdot \rho \boldsymbol{v}_{\text{II}} \qquad \text{(Conservation of Mass)} \qquad (2.11)$$

$$\boldsymbol{v}_{\text{II}} = -\frac{h^2}{12\mu} \boldsymbol{\nabla}_{\text{II}} P \qquad \text{(Conservation of Momentum)} \qquad (2.12)$$

$$\rho = f(S) \qquad \text{(Fluid Density)} \qquad (2.13)$$

$$\mu = g(S) \qquad \text{(Fluid Viscosity)} \qquad (2.14)$$

$$F(S, \boldsymbol{v}_{\text{II}}) = 0. \qquad \text{(Interfacial Motion)} \qquad (2.15)$$

Here, μ and ρ are the viscosity and density of the fluid mixture, as determined by functions f and g of the liquid volume fraction, S. The mixture property functions are constructed so that the material properties transition smoothly from that of bulk liquid to that of the bulk gas as saturation falls from 1 to 0. The function F describes the motion of the interface, and can be constructed from geometric arguments or derived from conservation laws. Further details are covered in Sections 2.3.1 and 2.3.3.

2.2.3 Numerical Solution Method

Systems of non-linear differential equations as described above are implemented in Goma[2][102] a software platform for solving multi-physics problems with the finite-element method. Goma discretizes these equation and solves them with Newton-Raphson method before evolving the system in time via backward Euler or Crank-Nicholson method. The linear systems of equations are solved with Trilinos[3], a

---

[2]http://goma.github.io

[3]https://trilinos.org

software package that provides a uniform application programming interface to several linear algebra packages for solution via direct or iterative methods. Problems can be parallelized by domain decomposition and simultaneous solution is performed with inter-process communications using OpenMPI[4]. Once implemented, predictive models for J-FIL can be solved using many-core workstation computers or high-performance computing (HPC) resources like CARC[5] and XSEDE[6].

Numerical stability, a primary concern, refers to the characteristic that dictates whether a simulation proceeds to completion without accumulating numeric errors that manifest as either non-physical solutions or inability of the solution method to converge. For simulations to be useful in design, they must be numerically stable and thus robust to changes in input parameters. Galerkin finite element methods are well known for exhibiting spurious oscillations around sharp interfaces in convection-dominated problems[73][18]. An extensive body of research has followed the initial investigation by Brooks et al.[21] addressing stability with the streamline upwind Petrov-Galerkin (SUPG) methods for stabilizing such oscillations. Their approach derives a modified test function that corrects the negative artificial diffusion inherent in central-difference and finite-element methods. Implementing stabilization techniques like SUPG can reduce the necessary mesh density thus allowing simulations to be performed faster with fewer unknowns. Reformulating the time derivative matrices that result from the FEM discretization with the mass-lumping[120] procedure mitigates unbounded growth of the pressure field near regions of sharp saturation transition. Besides SUPG and mass lumping, a non-physical diffusion term can also be added to the mass conservation or interface tracking equations, sacrificing accuracy to gain stability and extending the time scales of simulations.

The lubrication approximation simplifies the model enabling rapid simulations to

---

[4]http://www.open-mpi.org

[5]https://carc.unm.edu

[6]https://www.xsede.org

be used for NIL process design. The numerical solution framework facilitates testing of various two-phase flow models. The next section describes three variations on the classes of two-phase flow presented in this section.

2.3 Two-Phase Model Evaluation

The two-phase model evaluations in this section were performed to see if they would be useful in simulating thousands of drops. Each of these models was plagued by some constraint or deficiency that prevented it from effectively modeling so many drops. None-the-less, the virtues of each model are discussed in the following section.

2.3.1 Reynolds Lubrication and Level-Sets

The level-set method tracks an interface much the same way as a *total mass balance* approach does. The level-set field evolves with the velocity, and the level-set zero contour tracks the interface. Osher et al.[83] construct the level set field with a signed distance function, so that the value of the constructed field is the shortest distance to the interface.

Roberts et al. implemented level-sets for interface tracking in thin-film fluid flow[94]. In this approach, Equations 2.11 to 2.15 are used with the interfacial motion equation,

$$\frac{\partial F}{\partial t} + \boldsymbol{v}_{\mathrm{II}} \cdot \boldsymbol{\nabla} F = 0. \tag{2.16}$$

Here, F is the level-set field that is initialized by the signed-distance function. The method was shown to provide accurate predictions of squeeze flow pressures by comparison with analytical solutions. The level-set method also provides accurate prediction of interfacial motion, validated by direct comparison with single drop squeeze

experiments. Exploratory simulations using the level-set method revealed that as the initial gap thickness was increased, a corresponding increase in mesh density was necessary to accurately conserve liquid volume. It was assumed that a drop sitting on the substrate would take the shape of a half-sphere before fully bridging the gap. This assumption requires large initial gap thickness for which the level-set method is unsuitable to thousand drop simulations. The necessity of a very dense mesh was attributed to the sharpness of the interface, shown in Figure 2.6a.
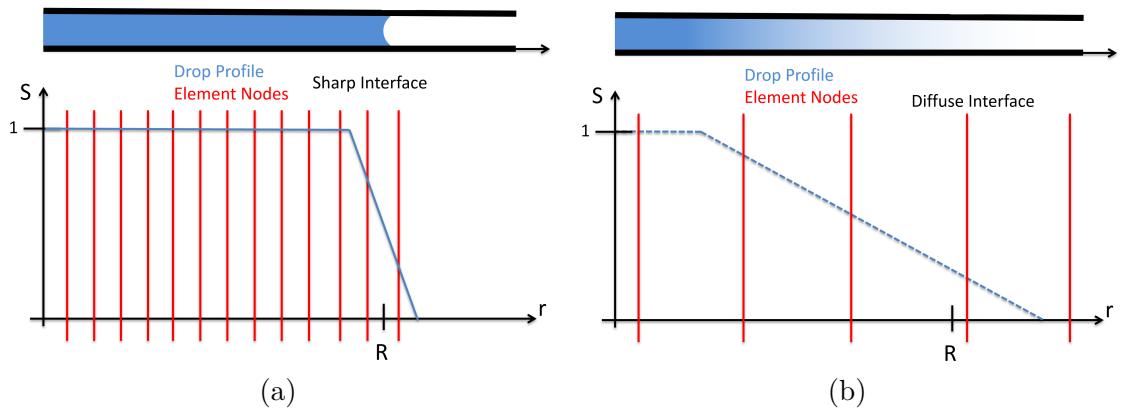
Figure 2.6: Drop profiles demonstrating sharp and smooth interfaces. (a) Sharp interface in the level-set method. (b) Diffuse interface implemented in the saturation-advection method.

It was then posited that a method with a more gradual transition between phases would allow simulations with larger elements, thus leading to reasonable solve times with meshes of lower density. Figure 2.6b shows the more gradual phase transition that might allow larger elements while also allowing the location of the interface to be adequately approximated.

More accurate information concerning the degree to which the liquid wets the substrate has come to light, allowing simulations with much smaller initial gaps and thus less dense mesh. This warrants re-investigation of the suitability of the level-set method in thousand drop simulations. Although the level-set method may yet be

found suitable for manufacturing-scale simulations, the concept of smoother phase transition has led to implementation of other interface tracking methods.

2.3.2 Two-Phase Darcy Flow

An approach analogous to two-phase Darcy flow in porous media has been implemented following the work of Cairncross et al.[24]. It begins with a mass balance for each phase, recall Equations 2.7 & 2.8. It continues with an approach that incorporates the capillary pressure jump across the interface. In this formulation each phase is tracked with a separate pressure,

$$\boldsymbol{v}_l = -\frac{h^2}{12\mu_l}k_l\boldsymbol{\nabla}P_l \tag{2.17}$$

$$\boldsymbol{v}_g = -\frac{h^2}{12\mu_g}k_g\boldsymbol{\nabla}P_g, \tag{2.18}$$

P_l for the liquid and P_g for the gas. Relative permeabilities for gas (k_g) and liquid (k_l) were also implemented. Here, the thin gap is thought of as a porous media with a single pore size. The radius of curvature of the interface can be separated into two components: one in the plane of the gap, r_{II} and one in the direction normal to the gap, r_z.

$$P_\Delta = \sigma\kappa \tag{2.19}$$

$$\kappa = \frac{1}{r_z} + \frac{1}{r_{\mathrm{II}}}. \tag{2.20}$$

Here σ is the surface tension and κ is the curvature of the surface. Simplification is achieved by several assumptions. First, the liquid is perfectly wetting, meaning the contact angle between the liquid-substrate and liquid-template contact lines are 0. Second, by assuming $r_z << r_{\mathrm{II}}$ and the surface forms a perfect half circle between the gap surfaces. These assumptions result in the following expression for curvature,

$$\kappa = \frac{2\sigma}{h}. \tag{2.21}$$

In porous media, smaller pores fill first due to menisci with smaller radii pulling fluid with greater force. This results in a tendency for capillary pressure to be high when saturation is low and vice-versa is represented by a constitutive relationship[24][13] of the form,

$$S = C_1 + C_2\text{tanh}(C_3 + \frac{C_4}{P_c}) \tag{2.22}$$

$$P_c = P_l - P_g. \tag{2.23}$$

The capillary pressure jump, P_c depends on the level of saturation and the difference in pressures of the liquid and gas phases. This set of equations describes a smooth transition of the pressure difference between phases. The values of the constants $C_{1,2,3,4}$ are determined by conditions on the values of P_c at saturations near zero and one, as well as the location and rate of transition. The phase transition center, $S = \frac{1}{2}$, occurs at the pressure jump, P_Δ predicted by the Young-Laplace equation, across an interface between two immiscible fluids.

After implementing this formulation in Goma, simulations produced results (Figure 2.7b) that qualitatively agree with the observations of the gas trapping experiment, shown in Figure 2.7a. The implementation is also robust with respect to decreasing mesh density, allowing rapid simulation of hundreds of drops. Unfortunately, the solutions suffer from egregious inaccuracy with respect to liquid volume conservation. When testing this formulation, a sign change in the total derivative dS/dt was necessary to achieve convergence of Newton's method, this might also have been the cause of the poor mass conservation. Although this formulation has poor mass conservation, it possesses extraordinary stability with respect to decreasing mesh density so it stands as an approach worth revisiting. Meanwhile, an alternative approach was taken, built on total conservation of mass (Equation 2.11).

(a) Experiment   (b) Simulation
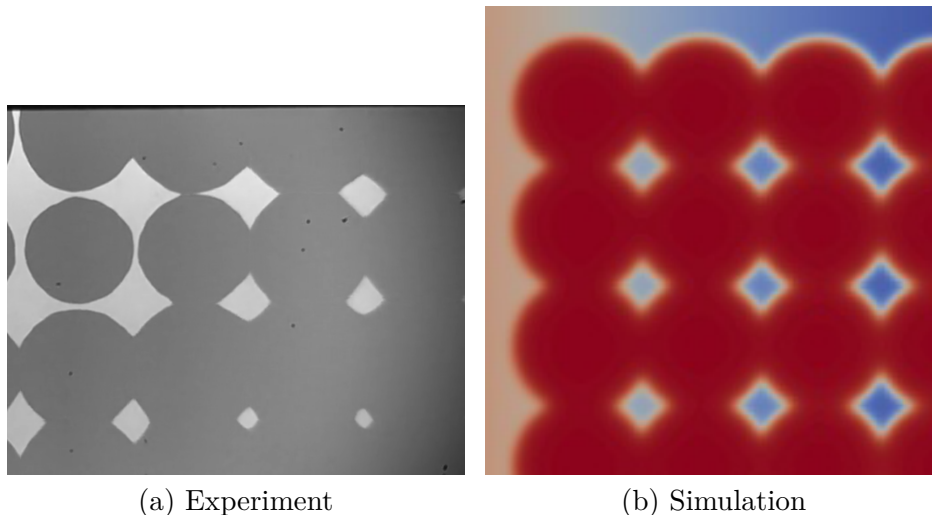
Figure 2.7: Simulated gas pockets match experiments.

2.3.3 Saturation-Advection

A method similar to pseudo-concentration methods[22] results when combining total mass balance of Equation 2.11 with an equation that conserves just the mass of the liquid. This approach utilizes material property functions and the lubrication velocity, i.e. Equation 2.12. Saturation, S is used to represent the liquid volume fraction. The material property equations are expanded as functions of saturation in this form:

$$\mu = a_\mu + b_\mu \tanh(c_\mu + d_\mu S), \tag{2.24}$$

such that it changes from the gas property to the liquid property in a continuous and smooth fashion. It is used for both viscosity and density in the saturation-advection implementation. Here, a_μ, b_μ, c_μ and d_μ are constants defined in part by imposing that the hyperbolic tangent asymptotes to the pure liquid phase μ_l when $S > 1$ and the pure gas phase μ_g when $S < 0$. A tuning parameter, β, is used to control the percent error in the values $\mu(S = 0)$ and $\mu(S = 1)$. The effect of changing the tuning parameter is shown against a simple lever rule for density in Figure 2.8.
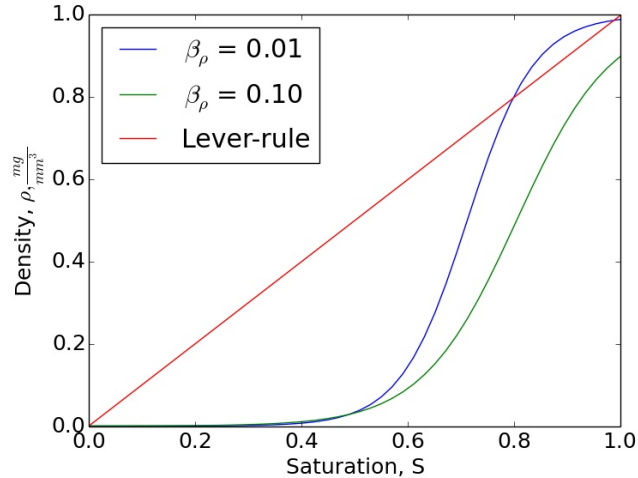
Figure 2.8: Density of a mixture of water and air as a function of saturation

An equation for liquid volume advection is derived from the control volume analysis based on liquid mass conservation within the gap,

$$\frac{\partial S\rho_l h}{\partial t} + \nabla \cdot S\rho_l h\vec{v} = 0. \tag{2.25}$$

Exploiting the fact that the bulk liquid density, ρ_l, is constant everywhere allows some simplification. Further, assuming h varies slowly and the fluid velocity orthogonal to the flow plane varies linearly between the confining boundaries results in an equation of the form,

$$\frac{\partial S}{\partial t} + \vec{v_{\mathrm{II}}} \cdot \nabla_{\mathrm{II}} S = 0. \tag{2.26}$$

This results in a system very much like the volume-of-fluid (VOF) method, in that the saturation is very similar to the VOF color function. Conservation of volume is the primary objective of VOF methods that discretize a domain into cells and use a color function to describe how much fluid is in a cell. The color of a cell is updated by how much fluid has flowed into the cell very much like Equation 2.26. A variety of algorithms exist for locating the interface based on the domain coloring, but with this advection of saturation, the saturation is tracked as a field variable not confined
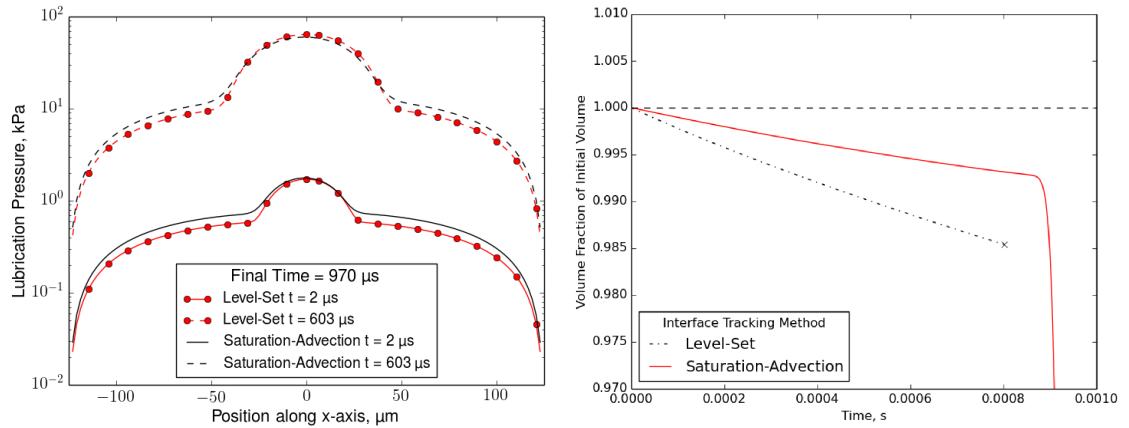
(a) Comparison of pressure profiles at two time steps.

(b) Comparison of liquid volume at the highest level of discretization

Figure 2.9: Direct comparison of level-set and saturation-advection simulations of squeeze-flow of a single drop

to cells. Since both methods track interface motion with the same sort of advection equation, the saturation-advection method can be described as an analogy to VOF methods.

Pressure profiles resulting from this formulation are compared to those of level-set simulations in Figure 2.9a, showing good agreement. The mass conservation characteristics of this method is compared to the level-set method in Figure 2.9b, showing reasonable accuracy with less than 2% error through the entire simulation. It is perhaps noteworthy that the volume fraction drops sharply at roughly 0.9 ms, which can be simply explained by loss of liquid volume as the edge of the drop begins to intersect the edge of the domain. Note also that the level-set method simulation fails due to non-convergence of Newton's method before the liquid reaches the domain edge. The mesh dependency of these methods is compared in Figure 2.10. For both approaches, mass conservation accuracy degrades with decreasing mesh density, however, the level-set method requires much smaller time steps than the saturation-advection method.
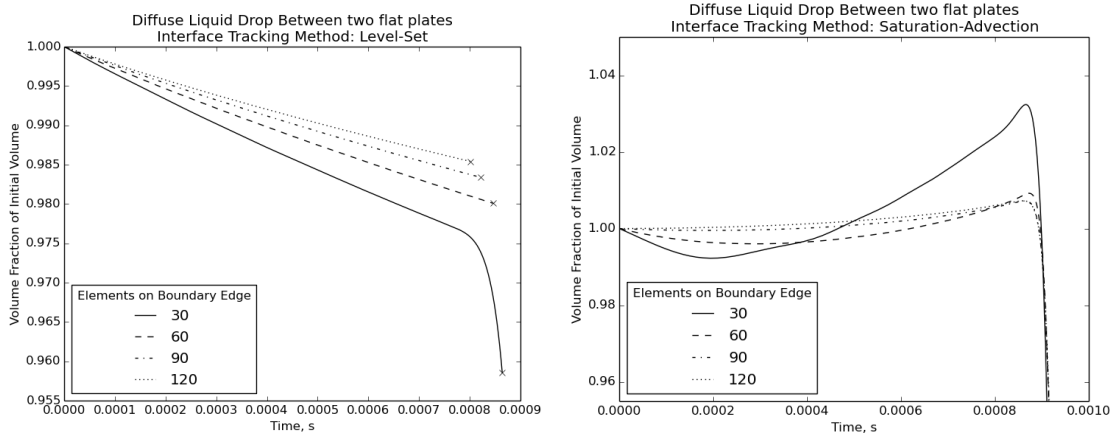
Figure 2.10: Volume Conservation vs. Mesh Density.

Larger time steps and longer resolved times make the saturation-advection method appear to be a better candidate for scale-up than the level-set method. However, verification simulations of four drops in squeeze flow show that when decreasing mesh density, the saturation-advection method sometimes produces non-physical solutions and simulations fail because Newton iterations fail to converge. In simulations of one hundred drops, SUPG test functions are found necessary to stabilize simulations so they can run to completion. However, with the use of SUPG applied consistently to only Equation 2.26, the mesh density must be increased to maintain stability.

The saturation-advection model has been used to successfully to simulate one hundred water drops merging over a 5 mm square domain. The drop volumes were set at 25 pL while actual experiments typically involve drops as small as 6 pL. Smaller drop volumes result in a decrease in stability: as the solution evolves, non-physical effects manifest and grow as Newton's method begins to converge more slowly. The non-physical effects are removed with the addition of SUPG, but this also requires a more dense mesh.

The one hundred drop stable system was increased in size, while maintaining drop pitch, drop volume, initial gap thickness and squeeze rate the same to achieve one thousand drop simulations. However, resulting simulation times were too long to be practical. This demonstrates that further work is necessary to stabilize the saturation-advection formulation in decreased mesh density simulations if it is to be used in manufacturing-scale simulations.

None of these two-phase implementations were found to be suitable for a one-thousand drop simulation in the NIL manufacturing system design process. No satisfactory balance of speed, stability and accuracy was demonstrated for interface-tracking two-phase flow methods. The next section discusses the development of a model for large area simulations of NIL that pursues a disperse two-phase flow implementation. Reynolds' lubrication theory is extended to capture gas-liquid dynamics based on relative permeability concepts used for multiphase flow in porous media. A reduced-order model of gas dissolution is constructed by combining two-phase lubrication theory with Henry's law and analytic approximations of surface area and diffusion length. The governing equations are solved on a thin-shell, finite-element model that can be used to investigate process sensitivities to a variety of technologically important parameters. Results are compared to those from related computationally intensive alternative formulations and to experimental flow visualizations to demonstrate its efficacy in modeling large area, many-drop processes and capturing the gas dissolution behavior observed in practice.

2.4 Model Success

An approach described by Brennen[20] as *disperse*, two-fluid flow is taken in this development because it inherently allows multiple fluids to occupy the same space and avoids the need to track explicit interfaces. Instead of tracking motion of two

fluids *separately*, the volume fractions are tracked by the "saturation" in the gap, where a diffuse representation of the liquid volume is used as depicted in figure 2.11. Previous findings that both smaller Henry's Law constants[75] and smaller drops[87] lead to shorter processing times motivates the inclusion of gas effects in this coarse-grain model. Work demonstrating that dwell times can be practically eliminated with condensible gases[58] juxtaposed against findings of increased shrinkage with condensible gases[1] illustrates that gas phase management plays a critical role in the process and drives model development towards the study of gas dissolution.

The formulation developed in this Section utilizes multiphase concepts of saturation and relative permeability augmented by a reduced-order gas dissolution model. Section 2.4.2 presents model results, demonstrating simple verification and one envisioned application. Comparison between simulation and experimental flow visualization demonstrate the model captures two-phase phenomena pertinent to prediction of gas dissolution dwell times. Section 2.5 discusses the results and future work.
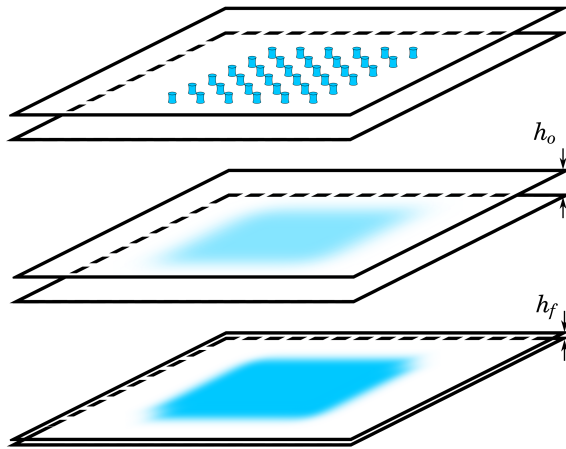
Figure 2.11: Ink-jetted drops represented as a diffusely saturated patch.

2.4.1 Disperse Flow

Continuity of two immiscible, yet reciprocally dispersed fluids is satisfied by employing two mass balance equations, one for each phase, adapted from phase field models of Hele-Shaw flow[37]. Each mass balance is integrated through the gap thickness and makes use of gap average velocities, yielding planar mass conservation equations.

$$\frac{\partial(h\rho_l S)}{\partial t} + \boldsymbol{\nabla}_{\mathrm{II}} \cdot (h\rho_l \boldsymbol{v}_l) = 0 \tag{2.27}$$

$$\frac{\partial(h\rho_g S_g)}{\partial t} + \boldsymbol{\nabla}_{\mathrm{II}} \cdot (h\rho_g \boldsymbol{v}_g) = 0. \tag{2.28}$$

Here, t is time, ρ_l is the bulk density of the liquid phase, ρ_g is the bulk density of the gas phase and $\boldsymbol{v}_l$ and $\boldsymbol{v}_g$ are the in-plane, gap-average velocities for the liquid and gas, respectively. The liquid volume fraction, S, or saturation, together with the gas volume fraction, S_g, make up the whole imprint volume, viz. $S + S_g = 1$. To capture two-phase behavior, the concept of relative permeability is used to calculate the individual phase velocities.

Relative permeability

The concept of permeability is extended from models of flow in porous media, in which volume flux density, $\boldsymbol{q}_d$ (dimensions: length/time), is proportional to the pressure gradient:

$$\boldsymbol{q}_d = -\frac{k}{\mu}\boldsymbol{\nabla}P \tag{2.29}$$

The permeability, k, lumps the effects of pore size, tortuosity, void fraction and level of saturation into a single, but variable parameter. Two-phase flow in an open channel between two flat plates is analogous to flow with a single but variable pore size i.e. the gap thickness. The similarity between volume flux density, $\boldsymbol{q}_d$ here and volume flux, $\boldsymbol{q}$ in Equation 2.4 suggests that the permeability of a thin gap is $h^2/12$.

Another concept borrowed from modeling approaches to flow in porous media is an additional factor of "relative permeability", used to describe the flow of one phase as it is impeded by the other phase(s)[12]. In other words, the flow of one phase, as driven by the pressure gradient, is restricted by the presence of the other phase. Therefore the relative permeability depends directly on the saturation and the nature of interaction between phases. Mathematically, the relative permeability k_α of phase α relates superficial velocity,[7] $\boldsymbol{v}_{s\alpha}$, of phase α to effective volume flow velocities, $\boldsymbol{v}_\alpha$[77]. In two-phase lubrication flow, the relative permeability augments the superficial velocity,

$$\boldsymbol{v}_\alpha = k_\alpha \boldsymbol{v}_{s\alpha} = \frac{h^2}{12\mu_\alpha} k_\alpha \boldsymbol{\nabla}_{\mathrm{II}} P. \tag{2.30}$$

Existing relative permeability models in the literature for Hele-Shaw flows address pressure-driven flow through fixed, wetted gaps[10], or flows in which mixtures have randomly distributed interfaces[48]. In contrast, the J-FIL process is characterized by phase mixtures with structured distribution and evolution of interfaces within a closing gap between dry surfaces(i.e. squeeze flow).
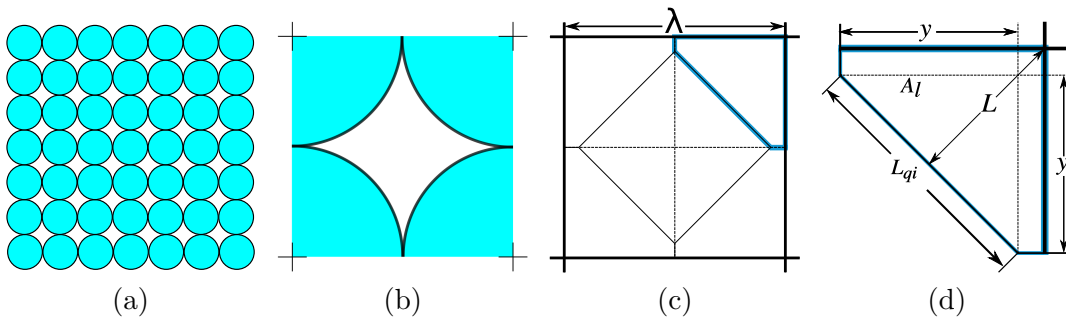
Figure 2.12: Gas-dissolution stage model geometry **(a)** Square lattice of circular drops at point of drop-drop contact. **(b)** Square lattice element **(c)** Simplified 'diamond' geometry **(d)** Micro-structure geometry

---

[7]The superficial velocity of a phase is the velocity computed as though that phase were the only phase present as it would be driven by the pressure gradient.

Development of relative permeabilities that capture the J-FIL flow configuration is motivated in part by discussion of the gas displacement and gas compression/dissolution stages (demarcated by the frames displayed in Figures 2.4a, 2.4b and 2.4d but also captured and simplified in schematic detail in Figure 2.12). From the point the liquid has bridged the gap, the liquid phase is completely discontinuous throughout the domain, so liquid flow is limited to expansion of the drops. In fact, the experimental observations in Figure 2.4 clearly suggest that net liquid flow across the lattice boundary is negligible up to the point at which the gas phase is completely eliminated.

The gas phase appears to flow freely, past the liquid bridges, until it is trapped. At that point, the gas becomes the discontinuous phase in which no net macroscopic flow can take place. While Romm's experiments[95] find linear relationships between saturation and relative permeability for unstructured flow, drop-merger observations show that net flow of gas stops before the gap is fully saturated. Reconciliation of these observations is achieved in the model by using a tunable relative permeability model (constructed from piece-wise linear segments in saturation, S).

$$k_{rg} = \begin{cases} 1 & : 0 \leq S \leq S_{cg} - \beta_g \\ m_g S + c_g & : S_{cg} - \beta_g < S < S_{cg} + \beta_g \\ 0 & : S_{cg} + \beta_g \leq S \leq 1 \end{cases} \quad (2.31)$$

$$m_g = -1\frac{1}{2\beta_g} \quad (2.32)$$

$$c_g = m_g(S_{cg} + \beta_g) \quad (2.33)$$
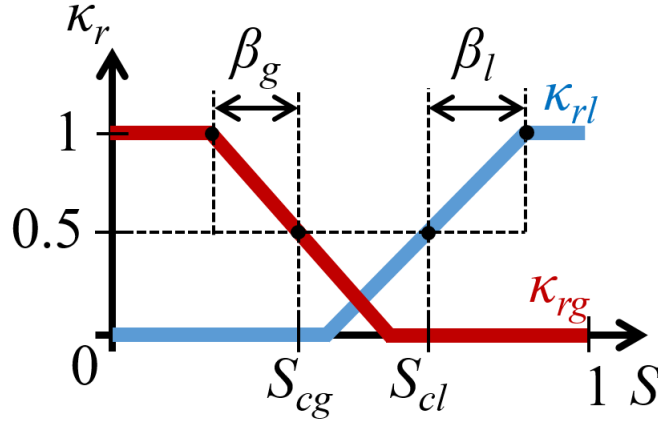
Figure 2.13: Parameterization of two-phase permeabilities using transition centers, $S_{c\alpha}$, and half-transition spans, β_α, for liquid and gas phases.

$$
k_{rl} = \begin{cases} 0 & : 0 \leq S \leq S_{cl} - \beta_l \\ m_l S + c_l & : S_{cl} - \beta_l < S < S_{cl} + \beta_l \\ 1 & : S_{cl} + \beta_l \leq S \leq 1 \end{cases} \tag{2.34}
$$

$$
m_l = 1\frac{1}{2\beta_l} \tag{2.35}
$$

$$
c_l = -m_l(S_{cl} + \beta_l) \tag{2.36}
$$

Here, the relative permeability for each phase, $k_{r\alpha}$, is tuned by selection of a transition center saturation, $S_{c\alpha}$, at which transition from free flow to no flow occurs and a half-transition length, β_α. These curves are depicted graphically in Figure 2.13. The choice of these tuning parameters is influenced by the type of simulation being performed (diffuse patch of drops or discrete drops) and is discussed in Section 2.4.2.

Gas dissolution

The derivation of Equation 2.6 assumes the fluid is incompressible, yet gas phase compression and resulting pressure rise is a driving force for its dissolution. The approach used in studies of compressible lubrication flow[54][9] typically just rein-

troduces the density into the mass conservation equation. With the assumption of constant temperature, the ideal gas law allows direct computation of the density from the pressure,

$$\rho_g = \frac{PM}{RT}.$$

(2.37)

Here, M is the molecular weight of the gas, R is the ideal gas law constant and T is the temperature, which for the purposes of this study is set to $25 \deg \mathrm{C}$ (subsequent numerical demonstrations use $T = 298\mathrm{K}$). Tracking pressure of the compressible gas phase allows the prediction of volume reduction by compression and dissolution into the liquid. The liquid is still taken to be incompressible, allowing for the liquid density to be divided out of Equation 2.27.

The final stage of the process, seen beginning in Figure 2.4c, is dominated by gas dissolution, a key rate limiting step. The liquid phase is taken here as an infinite sink that is initially saturated with gas at standard ambient pressure. Henry's Law states that the concentration of a chemical species, dissolved in liquid, is directly proportional to the partial pressure of the gaseous phase of that species, i.e.

$$PH = b_g$$

(2.38)

Henry's law constant, H, relates the partial pressure of the gas species to the interfacial concentration of dissolved gas, b_g. The model assumes a single gas species, so the partial pressure is taken as the lubrication pressure, P. The magnitude of the diffusive flux density, j, of gas species into the liquid drop is modeled with a lumped mass transfer expression,

$$j \cong \frac{D_{gl}}{L}(b_g - b_\infty) = k_D(b_g - b_\infty),$$

(2.39)

where D_{gl} is the molecular diffusivity of the gas species in the liquid solvent, L is the diffusion length, b_∞ is the concentration of the dissolved gas species in the delivered photo-resist and k_D is the lumped mass transfer parameter. The diffusion length is approximated with an analytic expression based on the square grid drop pattern.

An idealized dissolution model is developed assuming drops of identical volume, V_d, are arrayed in a uniform grid across the substrate in a square lattice with a pitch of λ, as shown in Figure 2.12. The volume-average diffusive flux of gas into the liquid phase, J is derived using the volume-average interface density, A_i/V_t, and the assumption that the magnitude of the flux density, j, is uniform across the gas-liquid interface,

$$J = j\frac{A_i}{V_t}h = h\frac{A_i}{V_t}\frac{D_{gl}}{L}H(P - P_{\text{atm}}). \tag{2.40}$$

Expressions for diffusion length and volume-average interface density are derived from the ordered evolution of the drop topology during gap closure. Before the drops contact each other, the diffusion length is taken as the radius of the drop, r, as defined by the drop volume, V_d, and the gap thickness, h,

$$L = r = \sqrt{\frac{V_d}{\pi h}}. \tag{2.41}$$

The volume-average interface density can be derived from the interface evolution of the square drop lattice. For every lattice element (Figure 2.2b) with lattice length, λ, the interfacial area, A_i, is that of a single, cylindrical drop and the total volume is of the lattice element,

$$\frac{A_i}{V_t} = \frac{2\pi rh}{\lambda^2 h} = \frac{2\pi r}{\lambda^2}. \tag{2.42}$$

Because the saturation is related to gap thickness through the pitch and drop volume, viz.,

$$S = \frac{V_d}{V_t} = \frac{V_d}{\lambda^2 h}, \tag{2.43}$$

the volume-average interface density can be derived as a function of saturation by combining Equations 2.41, 2.42 and 2.43,

$$\frac{A_i}{V_t} = \frac{2\sqrt{\pi}}{\lambda}\sqrt{S}. \tag{2.44}$$

These expressions hold in areas of constant lattice density throughout the gas-flow stage, however once the drops begin to merge, their shapes no longer match a growing circle and the evolution of the two phase geometry becomes more complex.

A simplified geometry of the drop structure is used to calculate diffusion length and volume-average interfacial area after the gas is trapped. The gas pocket between the drops, pictured in Figure 2.12b, resembles a shrinking square depicted in Figure 2.12c throughout the gas-dissolution stage. The diffusion length is approximated to be the shortest distance, L, from the gas pocket to the drop center. Several relationships necessary to compute the volume-average interface density and diffusion length are derived from this simplified geometry. A structure parameter, y, the liquid area, A_l, and the quarter interface length, L_{qi}, of the quarter-lattice-element, depicted in Figure 2.12d, relate the liquid drop volume and the lattice length to the inter interfacial area, diffusion length, saturation and gap thickness.

$$\frac{V_d}{4h} = A_l = \left(\frac{\lambda}{2}\right)^2 - \frac{y^2}{2} \tag{2.45}$$

$$L = \frac{1}{\sqrt{2}}(\lambda - 2y) \tag{2.46}$$

$$\frac{A_i}{4h} = L_{qi} = \sqrt{2}y \tag{2.47}$$

Re-organizing Equations 2.43, 2.45 and 2.46 yields the expression for gas-diffusion stage diffusion length in terms of gap thickness,

$$L = \frac{\lambda}{\sqrt{2}}\left(1 - \sqrt{2}\sqrt{1 - \frac{V_d}{\lambda^2 h}}\right). \tag{2.48}$$

An expression for the volume-average interfacial area in terms of saturation is found by combining Equations 2.43, 2.45 and 2.47.

$$\frac{A_i}{V_t} = \frac{4}{\lambda}(\sqrt{1 - S}) \tag{2.49}$$

The transition point between flow and dissolution stages occurs at the moment that drop edges make contact and trap gas pockets. This occurs at the moment

when the drop radius is equal to half of the drop pitch. Therefore, the transition saturation, S_t, for the square drop lattice is equal to $\pi/4$.

With the assumption that the liquid is an incompressible fluid and combining the dissolution rate, J, into Equation 2.28 as a sink term, the model equations become,

$$\frac{\partial Sh}{\partial t} + \boldsymbol{\nabla}_{\mathrm{II}} \cdot (\boldsymbol{v}_l h) = 0 \tag{2.50}$$

$$\frac{\partial \rho_g (1-S) h}{\partial t} + \boldsymbol{\nabla}_{\mathrm{II}} \cdot (\boldsymbol{v}_g \rho_g h) + J = 0. \tag{2.51}$$

Numerical Considerations

A Dirichlet boundary condition on pressure is sufficient when liquid does not cross the external boundary, however integration by parts of the advection terms in the weighted residual results in the default condition on saturation $\hat{n} \cdot (\boldsymbol{v}_l h) = 0$ at the boundary, where $\hat{n}$ is the vector normal to the boundary and in the plane of flow. The outflow boundary condition described by Papanastasiou et al.[85] is used if liquid should exit the domain through the boundary. As the model was developed, mass lumping, a small amount of artificial diffusion and a conservative clipping method were found necessary to achieve stability of the transient simulations.

A modulated artificial diffusion term, $D_a k_d \nabla^2 S$, is added to equation 2.50 to mitigate these spurious oscillations. This diffusion is tuned via the parameters β_d and S_{cd} as in Figure 2.14. No mathematical constraints exist in the model to prevent the saturation from rising above unity and because the advection of each phase is tightly coupled to the level of saturation, these spurious fields result in increasing non-physical behavior as solutions evolve in time. Specifically, when the saturation is greater than unity, the gas phase mass balance, Equation 2.51, drives the saturation higher. This non-physical behavior is remedied with a computational switch that substitutes the gas equation with an equation that acts to drive saturation back towards unity.
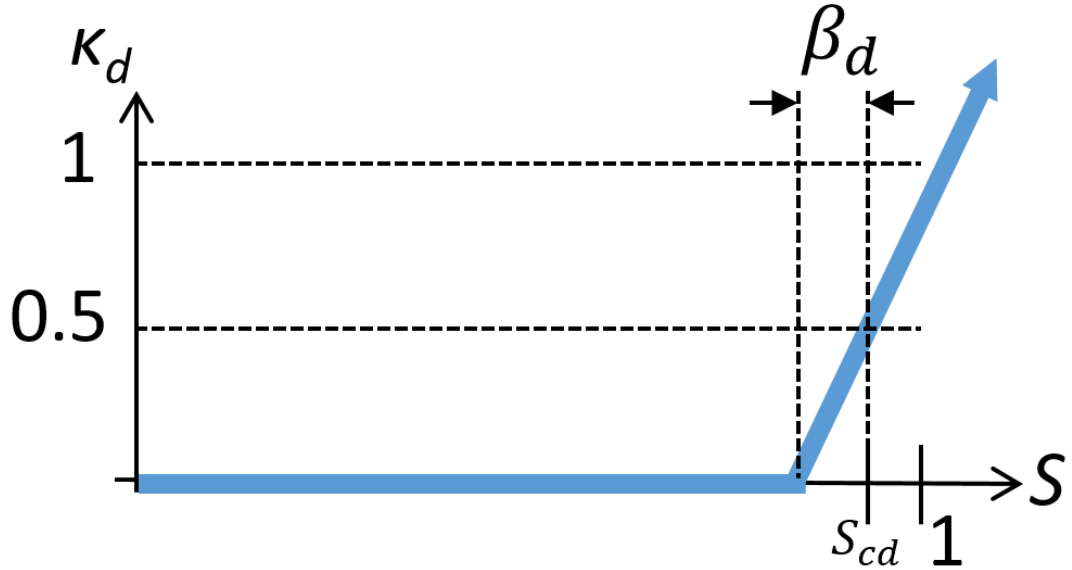
Figure 2.14: Artificial diffusion modulation scheme.

In regions devoid of gas, Equation 2.51 as written serves no purpose, and so is replaced with one that promotes monotonicity of the simulation. When $S \geq 1$, the advection and dissolution terms go to zero, the time derivative is expanded by the product rule and $(1 - S)$ is replaced with $k_c(1 - S)^2$ to obtain,

$$0 = h\frac{\partial S}{\partial t} - k_c(1 - S)^2\frac{\partial h}{\partial t} \tag{2.52}$$

Here, k_c is a parameter (chosen to be positive) that controls the strength of this spurious oscillation correction. Note that Equation 2.52 applies correction by requiring $\frac{\partial S}{\partial t} < 0$, because $(1 - S)^2$ is always positive and the closing gap implies $\frac{\partial h}{\partial t} < 0$. Since the liquid conservation equation (2.50) remains in effect, the conservation of the liquid volume is always maintained. Together, the modulated artificial diffusion and Equation 2.52 constitute a form of "clipping" of the non-monotonic behavior[73] of the saturation front. This clipping method has improved fluid tracking in thin-gap flow simulations, yet it is not sensitive to the change in gap thickness or variation in gap closure rate, making it difficult to tune for simulations with wide variations in

gap thickness and closure rate.

2.4.2 Results

In this section the model is demonstrated at two levels, first on diffuse drop patches and then on discrete drop patterns. An energy-based approach to determining the specific relative permeability parameters of Equations 2.31-2.36 is discussed in Section 2.4.2 followed by discussion of sensitivity to key thermo-physical parameters. A fine-grain, single-drop simulation exploring the limits of accuracy of interface evolution and pressure field predictions demonstrates that gas-liquid interfaces can still be captured effectively in Section 2.4.2. A simulation that captures the drop merger process is compared with experimental flow visualizations in Section 2.4.2. Finally, in Section 2.4.2, a coarse-grain simulation of varying density drop arrays is used to illustrate the class of problems this model was designed to support, and that the model is suitable for further advancement in subsequent work.

Diffuse Drops

The manufacturing-scale fluid mechanics resulting from the merger of thousands of drops can be examined with coarse grain simulations by starting with a uniform saturation, representative of the NIL process. A patch of ink-jetted drops is represented by a saturation field with a value of the total volume of drops divided by the total gap volume, illustrated in Figure 2.11.

For a diffuse representation of the regular square lattice depicted in Figure 2.2b, liquid relative permeability can be constructed to maintain the expected viscous dissipation. To maintain the expected dissipation within a lattice element, the rate of work done on the fluid needs to equal the rate of dissipation due to irreversible

conversion from kinetic to internal energy, as in

$$\int_A P \mathrm{d}A \frac{\partial h}{\partial t} = \int_{V_d} \boldsymbol{\tau} : \boldsymbol{\nabla u} \mathrm{d}V_d. \tag{2.53}$$

Here, A is lattice element area, V_d is the volume of the liquid within the lattice element, $\boldsymbol{\tau}$ is the viscous stress tensor and $\boldsymbol{\nabla u}$ is the velocity gradient.

In this approach, the notion of effective liquid pressure, P_l, is developed to relate forces developed due to drop liquid motion to coarse-grain lubrication pressure, P, and relative permeability. The motion of liquid is driven by the effective liquid pressure gradient which is equal to the gradient of the lubrication pressure modulated by the relative permeability,

$$\boldsymbol{v}_l = -\frac{h^2}{12\mu_l} k_{rl} \boldsymbol{\nabla}_{\mathrm{II}} P = -\frac{h^2}{12\mu_l} \boldsymbol{\nabla}_{\mathrm{II}} P_l. \tag{2.54}$$

From Equation 2.54, the assumption that the relative permeability is constant across a lattice element results in the relationship between lubrication pressure and effective liquid pressure,

$$k_{rl} P = P_l. \tag{2.55}$$

The effective liquid pressure is computed by dividing the total force per drop, F, by the lattice area.

$$P_l = \frac{F}{\lambda^2} \tag{2.56}$$

The force per drop is calculated by integrating the analytic expression for pressure field over the drop area, obtained by Reddy et al.[90].

$$F = -\frac{3}{2}\pi\mu_l \frac{r^4}{h^3} \frac{\partial h}{\partial t} \tag{2.57}$$

Now, the lubrication pressure changes negligibly across the lattice area so the rate of work done on the liquid can be computed as

$$\int_A P \mathrm{d}A \frac{\partial h}{\partial t} \approx P\lambda^2 \frac{\partial h}{\partial t}. \tag{2.58}$$

Breaking this expression into the sum of components due to dissipation in liquid and in gas gives

$$P\lambda^2\frac{\partial h}{\partial t} = [P\pi r^2 + P(\lambda^2 - \pi r^2)]\frac{\partial h}{\partial t}. \tag{2.59}$$

Because the dissipation of energy comes predominately from the liquid phase, the second term on the right is neglected, giving

$$\int\limits_A P\mathrm{d}A\frac{\partial h}{\partial t} \approx P\pi r^2\frac{\partial h}{\partial t}. \tag{2.60}$$

Combining Equations 2.55, 2.56, 2.57 and 2.60 gives

$$\int\limits_A P\mathrm{d}A\frac{\partial h}{\partial t} \approx -\frac{3}{2}\pi\mu_l\frac{r^4}{h^3}\left(\frac{\partial h}{\partial t}\right)^2\frac{\pi r^2}{k_{rl}\lambda^2}. \tag{2.61}$$

Irreversible conversion from kinetic to internal energy is obtained using analytic expressions for velocity fields as presented by Chauhan et al.[28] resulting in

$$\int\limits_{V_d}\boldsymbol{\tau}:\boldsymbol{\nabla u}\mathrm{d}V_d = -2\pi\mu_l\left(\frac{3}{h^3}\frac{\partial h}{\partial t}\right)^2\left(\frac{r^2h^5}{5} + \frac{r^4h^3}{12}\right). \tag{2.62}$$

Equating the two expressions for viscous dissipation, Equations 2.61 and 2.62 and simplifying, results in

$$\frac{1}{k_{rl}} = 12\frac{\lambda^2}{\pi r^2}\left(\frac{h^2}{5r^2} + \frac{1}{12}\right). \tag{2.63}$$

In typical NIL processes, $h^2/r^2 \ll 1$, this allows removal of the first term on the right-hand side of Equation 2.63. Furthermore, the saturation is the ratio of the liquid drop volume to the lattice element volume,

$$k_{rl} \approx \frac{\pi r^2 h}{\lambda^2 h} = S. \tag{2.64}$$

This relative permeability is achieved by selecting $S_{cl} = \beta_l = 1/2$.

As for relative permeability of gas, experimental observations show that gas no longer flows when the drops contact one another, i.e. when $S = \pi/4$. Because the gas is much less viscous than the liquid, its viscous dissipation can be neglected. Without regard to any viscous coupling of the phases or the resultant multiphase dissipation effects, a relative permeability that satisfies the flow/no-flow conditions for the gas phase results when $S_{cg} = \beta_g = \pi/8$. The sum of these relative permeabilities is less than unity except where $S = 0$ and $S = 1$, a result that is consistent with the experimental measurements of two-phase relative permeabilities for a fracture taken by Fourar et al.[46].

Sensitivity analysis of a diffuse carbon dioxide-water system in a gap closing at a constant rate shows that increasing the number of drops to deliver the same liquid volume requires smaller applied force. In this model, smaller forces are allowed by faster gas dissolution resulting from decreased diffusion lengths and increased inter-facial surface area (c.f. Equation 2.40). The trend of this prediction is in agreement with lubrication studies of Colburn[34] and Reddy[90].

A set of simulations is performed to demonstrate that the choice of gas species can have an effect comparable to an accessible change in the liquid viscosity. In each simulation, a patch of drops, saturated with the respective gas at atmospheric pressure, merge as the gap closes from 1 µm to 100 nm in 1 ms. The base case simulation is that of the merger of water drops with a viscosity of 1e-3 Pa·s in an atmosphere of nitrogen gas. Because the simulations are gap-thickness controlled and the dwell times are not an output of the model, a pseudo-work objective function is constructed to asses the energy requirement, E, corresponding to each test case. Specifically the pseudo-work is computed as,

$$E = \int\limits_{0}^{t_f} \int\limits_{A} P \mathrm{d}A \frac{\mathrm{d}h}{\mathrm{d}t} \mathrm{d}t. \tag{2.65}$$

Here t_f is the final time and A is the area of the simulation domain. The energy

requirement is reduced by 9% when the liquid viscosity is reduced by 20% from the base simulation. In comparison, the energy requirement falls 8% when the gas species is switched from nitrogen in the base case to carbon dioxide. These comparable reductions in energy for independent changes in liquid viscosity and ambient gas species indicate that choice of gas species impacts processing rate just as much as liquid viscosity.

Single Discrete Drop

The disperse, two-fluid model was formulated to capture the effects of disperse, immiscible fluid flows without capturing the interfaces, however it can also be used to model flow of fluids that are separated by regions of stark saturation contrast, much like distinct drops. Numerical investigations of evolution of a single drop, flowing outward in a closing gap, as depicted in Figure 2.2b, are reproduced with a level-set based, separated, two-fluid method[94] and compared (Figure 2.15) with simulations performed with this disperse, two-fluid model. A direct comparison of the two-phase lubrication models is achieved by excluding surface tension forces, taking gas density to be constant and foregoing the gas dissolution term, since the models do not possess complementary facilities for simulating them. The other relevant parameters are specified identically, as listed in Table 2.1.

To model discrete drops as islands of fully saturated volume, relative permeability parameters are selected that facilitate neighboring flows with starkly different material properties. Transition centers and transition lengths of $S_{cl} = S_{cg} = \beta_l = \beta_g = 1/2$, represent a boundary symmetry in that each material interacts with the interface in the same manner. Figure2.15c shows that increasing the interface resolution, either with denser mesh ($\epsilon = 240$) or smaller transition lengths ($\beta_l = \beta_g = 1/10$) leads to more accurate pressure predictions at later simulation times.

Simulation Parameter	Value	Units
Initial Gap Thickness	1.32	µm
Initial Drop Volume	2.59	pL
Gap Closure Rate	1.36	$\frac{\text{mm}}{\text{s}}$
Simulation Time	800.	µs
Gas Viscosity	18.6e-3 (18.6e-6)	cP (Pa·s)
Liquid Viscosity	10.0 (10e-3)	cP (Pa·s)
Boundary Pressure	101	kPa
Domain Edge Length	250.	µm
Elements per Domain Edge	120	

Table 2.1: List of physical parameters defining the simulations of a single drop in a closing gap.

(a) Liquid volume vs. time   (b) Pressure after 400 µs   (c) Pressure after 800 µs. Here ϵ is elements per domain edge (as in Table 2.1)
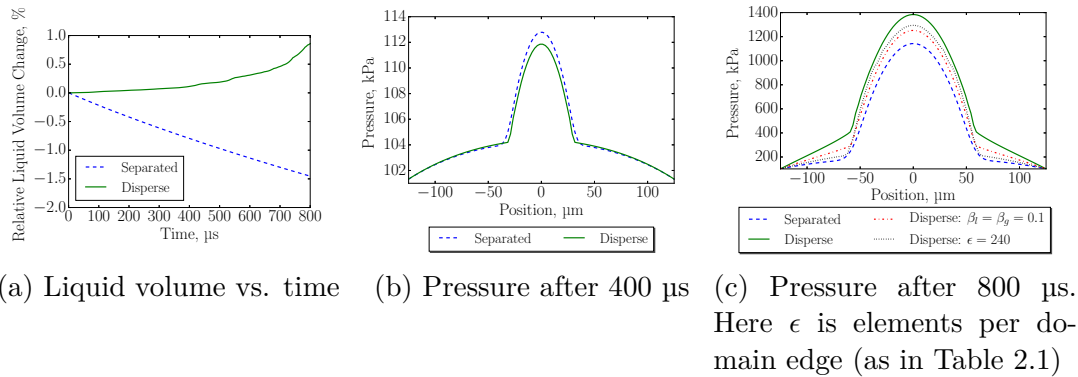
Figure 2.15: Direct comparison of volume conservation characteristics and predicted pressure in separated flow (level-set) and two-mass balance flow models in the single drop case. Subfigure (c) demonstrates the sensitivity of the pressure field to decreasing transition lengths and increasing domain resolution.

Figure 2.15a shows the liquid volume as normalized by the initial liquid volume, computed via integration over the domain at each time step. The liquid volume error accumulation over time in the separated and disperse methods are 1.4% and 0.8% respectively. The pressure fields are compared at two different time steps in Figures 2.15b and 2.15c. The predicted pressure fields at 400 µs are nearly identical, however, at the end of the simulation, the maximum pressure differs by nearly 20%.

Several factors have been found to influence the disparity between the pressure field maxima, including choice of stabilization parameters, mesh density and liquid permeability parameters. Although increasing domain resolution and decreasing β_l and β_g all lead to better agreement between pressure predictions, exact agreement between models is not expected in any case.

Flow Visualization

A flow visualization of drop merger was captured with high speed video as pictured in Figures 2.4 and 2.16. A square lattice pattern of 6 pL drops was ink-jetted onto a flat glass plate substrate. A second glass plate was then lowered onto the drops with a displacement-controlled ram. As the gap closes, the pressure becomes very high and plate motion control is switched to constant force while the gas pockets dissolve. The apparatus is surrounded by atmospheric gas at ambient pressure and when fluid reaches the edge of the plate (top boundary in Figure 2.16) its motion is arrested by contact line pinning.

Two assumptions about the experiment are made to estimate parameters that are needed for the simulation. The first is that each drop is a spherical cap which sets a relationship between drop volume, contact angle and standing drop radius. The second is that the contact angle is 7.5° which sets the standing drop radius of 39 µm. The ratio of lattice spacing to the standing drop radius, measured by pixel ratio, determines the lattice spacing to be 203 µm.

The frames of the video are analyzed with computer vision software OpenCV[19][8]. A combination of Gaussian blurring and Otsu's binarization[9] is used for each frame to produce an image showing liquid in black and gas in white. Saturation is calculated as the ratio of black pixels to the total number of pixels in a given lattice

---

[8]http://opencv.org/
[9] https://docs.opencv.org/3.3.1/d7/d4d/tutorial_py_thresholding.html

element. Because the interface is smeared as a result of the video processing, there is uncertainty in the number of black pixels, on the order of the number of pixels along the interface length. This saturation dependent uncertainty is maximized when $S = \pi/4$ at roughly 2.5% of the number of pixels in the lattice element. The gap thickness is subsequently computed from this measured saturation by Equation 2.43 because the liquid is incompressible. The saturation predictions and calculated gap thicknesses are only valid after the gap thickness is 1350 because the drops do not fully bridge the gap until this point.

A simulation of 16 water drops surrounded by CO_2 using a modified height function is compared to the flow visualization experiment. The simulated gap thickness function is stretched in time in order to achieve simulation stability.

Figure 2.16 shows the gap thickness as determined from the experiment, a least-squares fit of a hyperbolic tangent function to the calculated gap thickness as well as the smoothed, simulated height function. The oscillation in the experimental data curve right before gap thickness reaches 1350 nm stems from transformation of the drops from spherical sections rising from the substrate to cylinders that bridge the gap. Since the time scales differ between simulation and experiment, the visual comparisons are made at specific gap thicknesses. Inset into Figure 2.16 are direct visual comparisons between simulation and experiment at four different gap thicknesses, demonstrating qualitative prediction of the two-phase flow.

This section shows that key process features observed in experimental images are captured with a multi-drop simulation. As the gap closes from 1350 nm, the drops expand from the their centers until they merge at 186 nm gap thickness. The pockets of trapped gas compress and dissolve until the gap is occupied by liquid only at a gap of 146 nm. This experimental comparison, while not true validation of the model, demonstrate that the disperse, two-fluid approach is able to capture the gross features of the flow.
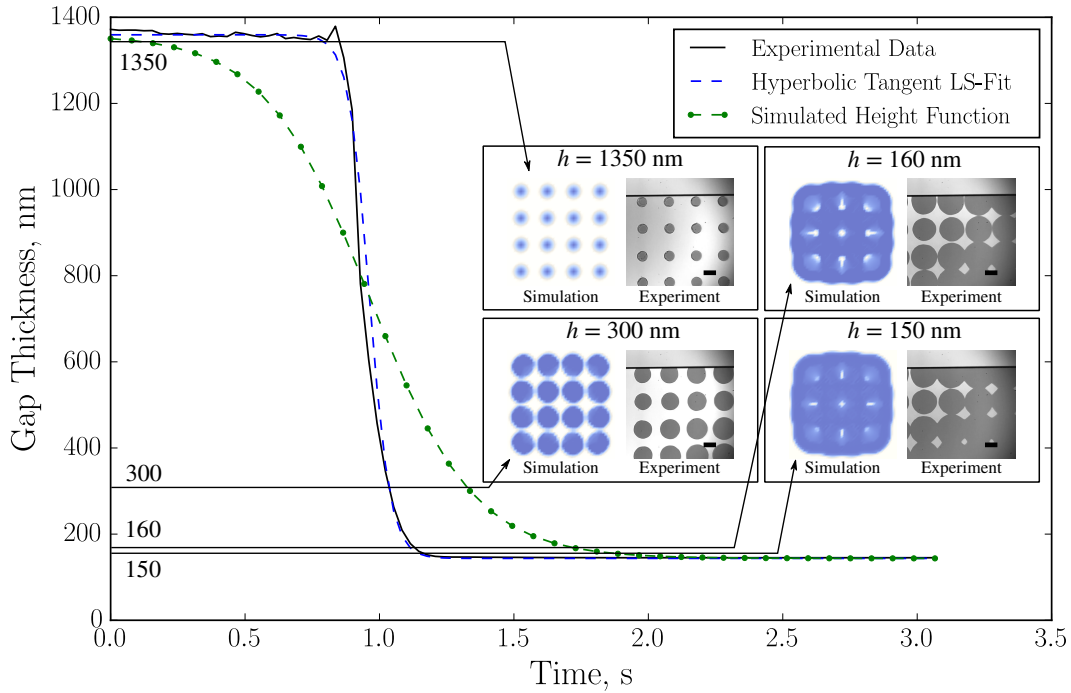
Figure 2.16: Plot of gap thickness vs. time for experiment, curve-fit and simulation. Inset are direct visual comparisons at heights marked by parallel lines from the gap thickness axis. Scale bars represent 100 µm.

Exemplar device

In NIL processes, templates may contain a variety of features positioned to create complex patterns possessing several tiers of feature density (e.g. transistors are organized to form logic gates that are in turn grouped to create processors). The approach developed here can be adapted to model varied patterns of drops for such purpose. For example, Figure 2.17a illustrates a mask for use as a conductive layer etch barrier to be employed in the fabrication of a transistor array. In the center of the pattern is the array of the conductive paths for planar transistors[29] that might be used to drive an array of LEDs in a display. The contact pads at the edge and the block of transistor elements in the center have a much greater feature

density and therefore require more liquid, i.e. a more dense drop pattern than the wire paths connecting the two regions, depicted in Figure 2.17b. To demonstrate how J-FIL processes with varying drop densities can be simulated, the saturation field is initialized with corresponding saturation levels, as shown in Figure 2.17c. Atmospheric pressure and free outflow conditions are applied at the boundary.

(a) Conductive layer for planar transistor array

(b) Varying drop patterns required by varying imprint patterns

(c) Saturation field initialization
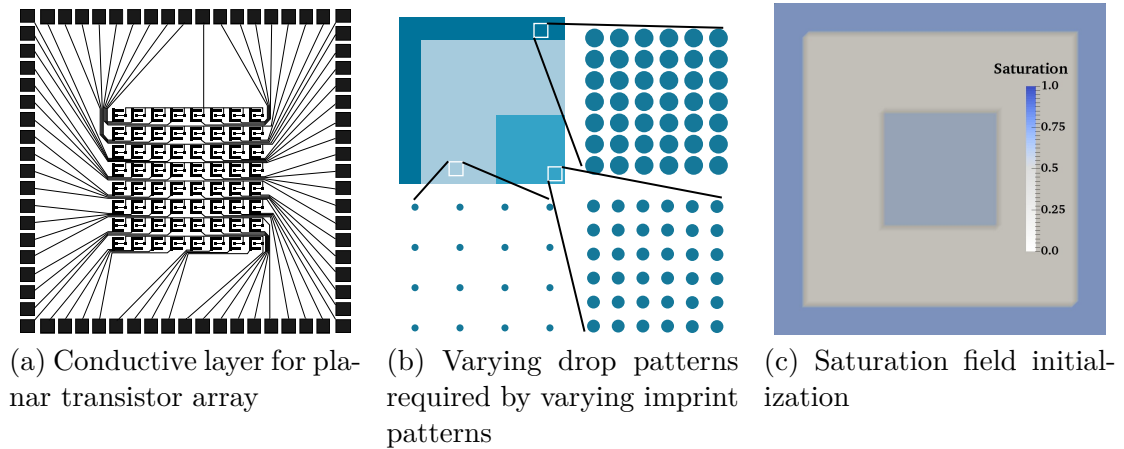
Figure 2.17: Single-layer pattern, commensurate drop patterns and simulation initialization for transistor array.

The regions of higher saturation fill first, and as the model does not yet account for patterned templates, once the gap is filled, the liquid must flow into adjacent unsaturated regions. Figure 2.18a shows that all the gas in the central and edge regions has escaped or dissolved while the low-liquid-density wiring region has not yet completely filled. Figure 2.18b show that as the simulation proceeds, the fully saturated central and edge regions begin to flood the wiring region.

This example demonstrates the capture of two-phase lubrication flow for the class of applications for which the model is intended. In future work, predictive capabilities will be expanded by the addition of physics of substrate/template deformation, capillary action, and fluid flow into the template. Structural mechanics can be in-
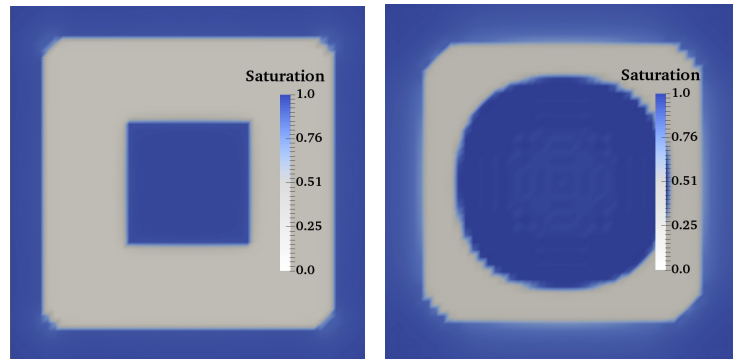
(a) Filled transistor region (b) Liquid flowing from saturated to unsaturated regions

Figure 2.18: Saturation rises to fill the closing gap before flowing outward from a full gap.

corporated by coupling to membrane mechanics[25] or plate mechanics To predict flow anisotropy observed in experiments like those of Zhang et al.[5] this gap flow model may be coupled with a template flow model based on porous media flow theory as described by Roberts et al.[93]. Pattern flow effects of increased dissolution and capillary action could be captured by extension of the porous flow model by the approach to dissolution described by Chauhan et al.[28].

2.5   Conclusion

A model for two-phase flow in a closing gap that is suitable for simulating drop merger of drop-dispensed nanoimprint lithography processes has been presented. The model is implemented in a continuum finite-element code. This implementation enables the application of lubrication theory to problems in which incompressible liquids interact with compressible, dissolvable gases. The model demonstrates qualitative prediction of closing gap drop merger by capturing evolution of interfaces in addition to gas trapping/dissolution behaviors that are congruent with video captured of the process.

Conservation of mass and momentum are applied to each phase individually and interaction between phases occurs through the saturation-based relative permeabilities. This disperse, two-fluid flow model enables the simulation of large area, multiphase lubrication processes by reducing the computational complexity, and hence, computation time, with reduced-order models that allow reduction of required spatial resolution. Variation of the dispensed drop pattern, (i.e. spatial variation of drop size, lattice spacing and lattice type) can be addressed in the dissolution model, however these variations are not reflected in the relative permeability model, representing one of the many research pursuits for future work.

Avenues for future work include exploration of alternative gas compression models that may be more appropriate for the length scales and pressures involved in these NIL flows. As the dissolution model is formulated specifically for disperse, two-fluid flows, re-tailoring of the dissolution model may improve the accuracy of discrete drop simulations, although the current model adequately portrays gas trapping and subsequent gas dissolution when diffuse interfaces are included. Improvement of the clipping method will reduce total computation time for both disperse and separated flow simulations. A more detailed study of energy landscape with respect to liquid viscosity, gas properties, RLT and gap closure rate will advance the understanding of the role of gas in drop merger during NIL. Incorporation with thin-shell structural mechanics will extend simulation capabilities to enable prediction of residual layer thickness variations driven by capillary action and coupled deformation of substrate and template. To conclude, this work serves as a building block to be used in the development of more advanced models that will enable predictive simulations to guide the design of drop-dispensing nanoimprint processes.

The next chapter discusses the approaches to bringing a model for structural mechanics into simulations for predicting residual layer thickness. A coupled model of the two-phase flow between a rigid roller and a flexible web is validated by matching

predictions to experimental data found in the literature.

Chapter 3

Elastohydrodynamics of Tensioned Web UV-imprint Lithography

3.1 Introduction
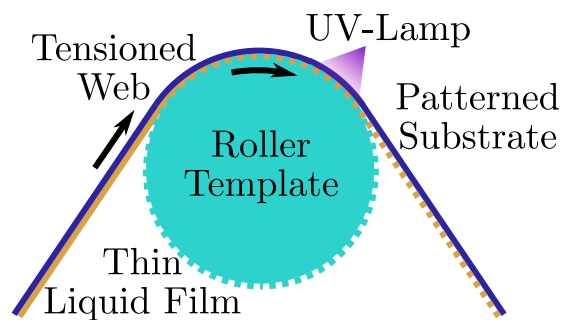
Figure 3.1: Roll-to-roll imprint lithography.

In nanoimprint lithography (NIL) a template is pressed into a thin liquid layer to produce a nano-patterned substrate ready for subsequent processing steps[30][53]. The patterning step is essential to unlocking the benefit of nano-scale phenomena that enhance devices like solar panels [79], batteries[60], optical films[106] and certainly

many others. Augmenting roll-to-roll (R2R) lines with nano-patterning as in Figure 3.1 will enable high volume production of the nano-enabled materials used in next generation devices. This way of patterning relies on the interaction of hydrodynamic forces exerted by the liquid layer and the elastic forces exerted by the deformable solid boundary of the substrate, an elastohydrodynamic interaction.

UV-cure NIL, uses a photo-curing solution that can quickly fill the nanofeatures in the template during the imprint. Once the liquid assumes the shape of the template, an ultraviolet light is used to illuminate the photoresist, causing it to cure, that is, to change phase from liquid to solid. The template is then separated from the solid photoresist resulting in the transfer of the pattern to its inverse on the substrate.
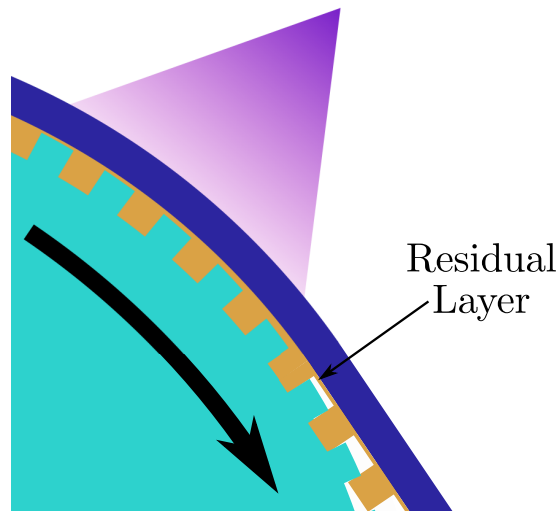
Figure 3.2: Residual layer in imprint lithography.

Any part of the cured photoresist that isn't part of the pattern is the residual layer, pointed out in Figure 3.2. If the residual layer thickness (RLT) is thin enough, the pattern can be used as an etch mask for transferring the pattern into the substrate[3]. If a thin layer of active material had been placed on the substrate before patterning, the result would be a patterned layer of that material[91]. In other cases the pattern structure is to be used as a scaffold in the device, as with the wire-grid

polarizer described in the introduction. Using the pattern as a mask for etching or surface treatment requires the residual layer to be broken through. For processes that use the pattern as an etch mask, the residual layer may be thin enough to be broken through by the etch meant for the underlying material, but non-uniformity will result in magnified variation in the substrate etch depth. For processes that use the pattern as a surface treatment mask, an isotropic breakthrough etch may degrade the pattern anywhere the RLT is on the order of the feature size. In these ways, non-uniform RLT degrades the yield of a process. In the case of the wire-grid polarizer, RLT non-uniformity could result in undesirable interference structures, affecting the performance of the product. In any case, the manufacturing-scale process development toolbox must provide the designer some insight into RLT non-uniformity. A mathematical model of the feature-fill regime should inform its user based on two-phase fluid mechanics and structural deformation that precede the UV-cure. When this R2R nanopatterning process is refined it will enable economic high-volume manufacture of nanofeatured materials that can be used to construct improving consumer access to nanotechnology[112][62].

The process has been demonstrated to achieve features as small as 4 nm[7], but as a relatively new processing technology, low yield associated with RLT uniformity is a formidable barrier to its implementation. For the consumer electronics market, high volume manufacturing processes must reliably produce materials with very high uniformity to keep costs down and remain profitable[71]. The challenge of pre-metering the liquid photoresist such that the residual layer is under 100 nm rules out traditional deposition techniques like slot-die, gravure and kiss coating (c.f. Figure 3.3) that bottom out around 1 micron coat thicknesses. One approach to overcoming this barrier is to use an inkjet head to gain more fine control of liquid volume deposition to create the process depicted in Figure 3.4, a R2R modality of an NIL method called jet-and-flash imprint lithography (J-FIL)[7][109]. The fine control of fluid volume allows the amount of liquid dispensed to vary across the substrate based

(a) Slot-Die Coating

(b) Gravure Coating

(c) Kiss Coating
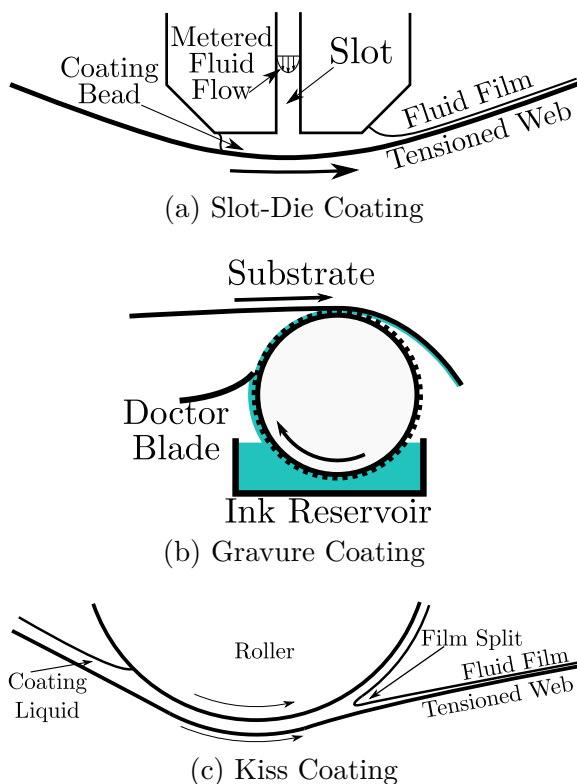
Figure 3.3: Several types of R2R thin film deposition processes.
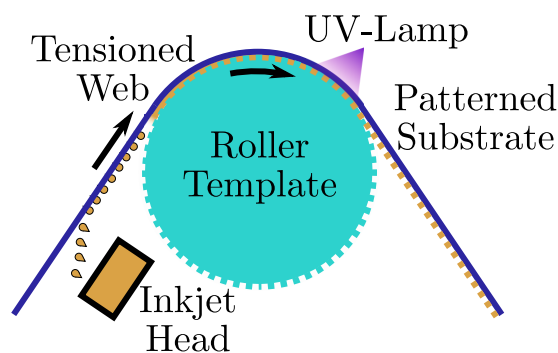
Figure 3.4: Roll-to-roll jet-and-flash imprint lithography.

on the volume of the features to be filled. Although inkjet printing provides greater control of fluid placement, the drops are of finite volume and they trap pockets of gas as they merge in the closing gap. For merger of 10,000 drops per square centimeter,

the size of the gas pockets is on the order of 100 m. Reddy[90] and Chauhan[28] showed that smaller inkjet drops are better because large viscous forces in the thin gaps act over shorter distances. Smaller drops trap smaller gas pockets that dissolve faster due to decreased dissolution lengths and decreased gas quantities that need to be dissolved. Figure 3.5 shows how the capillary forces influence the pressure in the gap as well as how the pressure is likely to influence structural deformation as well as the formation of the residual layer. Figure 3.5b show the surface tension forces that act on the web cause local deformation that adversely affects the uniformity of the residual layer. the elastohydrodynamics of two-phase flow and tensioned web

(a) Pressure profile across a pocket of trapped gas

(b) Pressure induced deformation

(c) Non-uniform residual layer

(d) Uniform residual layer
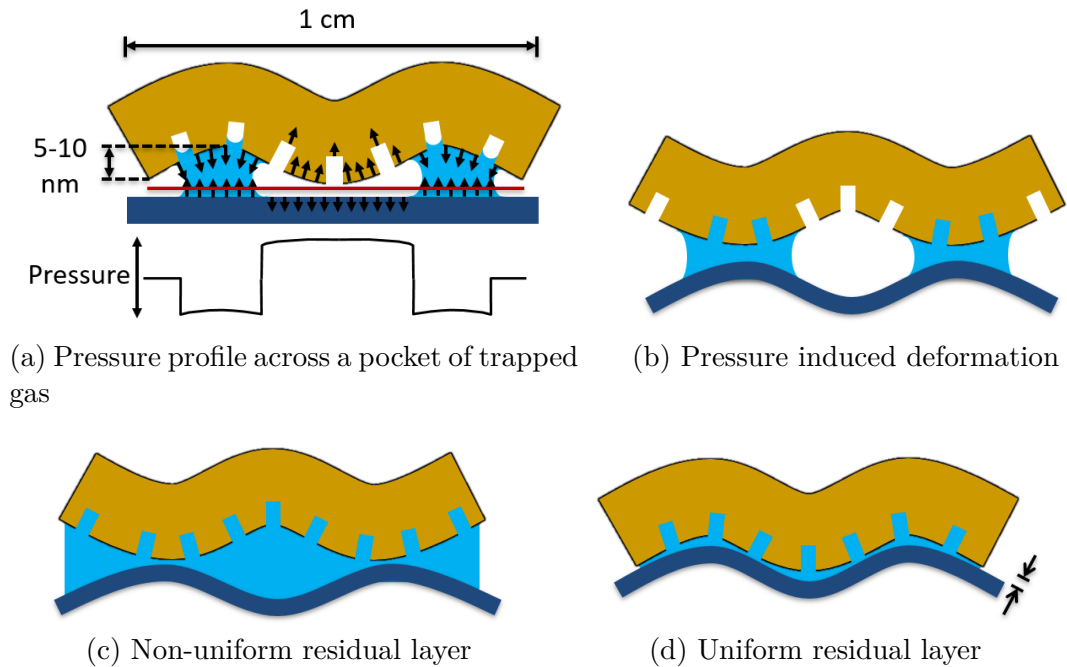
Figure 3.5:   Capillary forces and the residual layer thickness.

mechanics together form models for predicting the RLT because a high degree of precision is necessary to obtain high NIL process yield.

In the development of manufacturing processes, a tight feedback between model predictions and experiments accelerates the convergence to optimum manufacturing

process parameters. Despite the increased computational power available to present day analysts, compute time still scales with the cube of the number of unknowns in the problem. This work investigates reduced-order-models for shorter computation times so they may be used in iterative design of experiment processes.

As discussed above, RLT is a key outcome that influences the quality of pattern transfer by chemical etching. The fluid layer thickness where the photoresist is cured should be predicted to infer the RLT. The model is constructed to assess the fluid layer thickness as a function of processing speed, wrap angle and web tension. The model can also be adjusted to account for material properties of viscosity and web bending stiffness in addition to machine parameters of roller radius and idler position.

Figure 3.4 shows that in the R2R modality of J-FIL, pattern filling and UV-curing will occur as the wrapped web travels around the rotating imprint roller. This work focuses on modeling a lubricated segment of web for identifying key parameters for the curing process and support the production of homogeneous product. The model should help process designers predict the thickness of fluid film layer in addition to the window available for UV-cure under minimal shear forces. In Prankch's thesis[89], he enumerated several elastohydrodynamic systems that involve the interaction between a fluid and a tensioned web, of these, foil-bearings present an interesting case because they possess a region of uniformity that might be ideal for UV-cure.

The most prominent application for regions of uniformity in systems with lubrication layers is the magnetic tape reader. These systems have evolved to posses read heads with precisely formed depressions that control fluid layer thickness where the tensioned tape is translated past the stationary read head[55]. The study of these systems began with analysis of what are called foil bearings in which the bearing material would offer no structural resistance to axial deformation. Blok and van-Rossum[15] observed that pressure and thickness of the fluid layer where constant through the length of the bearing, except for the leading and trailing regions. They

also derived a scaling law relating the nominal fluid layer thickness, h^*, to the journal radius, r, fluid viscosity, μ, foil tension per unit width, T, and rotation rate. The scaling prediction was refined by Eshel et al.[41] and experimentally validated by Ma[78] and later by Licht[76] to be

$$h^* = Kr \left(\frac{6\mu U}{T} \right)^{\frac{2}{3}} \tag{3.1}$$

where U is the speed of the foil moving past the journal and K is generally accepted to be 0.643 for highly flexible materials. William Gross[52] codified much of the work done to understand effects of wrap angle, bending stiffness, inertia and foil width. The work of the magnetic tape reader community emphasizes the dimensionless foil-bearing number, $\epsilon = 6\mu U/T$ the ratio of viscous forces to tension forces. The study of tape reader systems were focused on cases in which either the read head or the web are stationary with respect to the motion of the other. Subsequent studies of web handling[70][39] have validated the similarity of using the average of roller surface velocity (u_a) and web velocity (u_b) in the foil-bearing number, $\epsilon = 12\mu(u_a+u_b)/2/T$. These expressions are equivalent because, U, the speed of one surface moving passed the opposite, stationary surface is double the average velocity that is $12U/2 = 6U$.

Studies of elastohydrodynamics of this nature were also conducted by the coating & conversion community. For kiss coating (Figure 3.3c, film thickness is strongly influenced by conditions at the nip outflow because of the film split in the exit region[36][50]. In general, positive outcomes of tensioned web roll coating processes are constrained by whatever measures are necessary to avoid instabilities in film formation[25]. In slot-die coating of flexible webs[43] (Figure 3.3a) film thickness is governed by the flow rate and web speed[26]. The body of literature regarding coating processes is primarily concerned with the fluid film formation at the coater exit region.

Only recently has the idea of attaining thinner films by curing merged drops between substrate and superstrate been investigated and designated Jet and Coat

of Thin-films (JCT) by Singhal et al.[2]. This idea was explored in the context of coating wafers in a step and repeat mode, but did not address R2R processes directly. Their findings concerning the relationship between spreading time and layer uniformity should be considered in R2R process design. Jain et al. studied the process that transfers patterns from a roller template onto a flat, rigid substrate[64]. Their analytical work finds an expression for the time available for UV-cure after transfer, given the drops merge completely during the approach of the rigid template to rigid substrate. To study the fluid layer thickness for the imprint of a flexible substrate, equations of flow and thin structure are solved computationally.

3.2   Model Development

A three-dimensional shell is employed to capture deformation and lubrication flow for the case of a lubrication gap between a free-span, tensioned web and a flat, featureless template. An approach analogous to the Reynolds lubrication for fluid mechanics reduces model order of the structural mechanics. The results of this 3D model highlight the influence of capillary forces on the elastohydrodynamics of free-span web systems. The difficulty of identifying problems in the 3D formulation leads efforts to develop a two-dimensional shell model to predict the gap thickness between a stiff web translating with the surface of a rotating roller.

The mechanics of the fluid and solid are modeled a set of coupled equations that captures the elastohydrodynamics of the system. Since the fluid layer is thin, Reynolds' lubrication approximation is invoked to reduce the model order for the fluid mechanics. Since the web is thin, a model based on Mindlin plate theory[89] is invoked to reduce the model order of the structural mechanics. For a particular geometry, the finite element method produces a set of discrete, nonlinear algebraic equations from a set of partial differential equations. The Newton-Raphson method

solves the non-linear equations by an iterative process of linearization and solution by linear algebra.

3.2.1   Elastohydrodynamics on Three-dimensional Shells

The development that follows was built on the work of Pranckh[89] but Dr. Tjip-towidjojo was inspired to extend the models to capture bending stiffness by the geometric approach presented by Soedel[111]. A quasi-static steady-state model for the web structure develops under the application of total force balance. The tangential force balance equations comprise extension stress, shear of the web and bending moment stress

$$\boldsymbol{\nabla}_{\mathrm{II}} \cdot \boldsymbol{N}_1 \qquad\qquad + \kappa_1 \boldsymbol{\nabla}_{\mathrm{II}} \cdot \boldsymbol{M}_1 \qquad\qquad = 0 \qquad (3.2\mathrm{a})$$

$$\boldsymbol{\nabla}_{\mathrm{II}} \cdot \boldsymbol{N}_2 \qquad\qquad + \kappa_2 \boldsymbol{\nabla}_{\mathrm{II}} \cdot \boldsymbol{M}_2 \qquad\qquad = 0 \qquad (3.2\mathrm{b})$$

Extension and   Bending moments about

web-plane shear   axes in the web-plane

The normal force balance equation contains components that arise from extension around a curve, bending moments and applied pressure.

$$\kappa_1 N_{11} + \kappa_2 N_{22} \qquad - \boldsymbol{\nabla}_{\mathrm{II}} \cdot \boldsymbol{M}_1 - \boldsymbol{\nabla}_{\mathrm{II}} \cdot \boldsymbol{M}_2 \quad + F \qquad\qquad = 0 \quad (3.3)$$

Curved extension   Bending moments   Applied pressure

Here $\boldsymbol{N}_{1,2}$ and $\boldsymbol{M}_{1,2}$ are components of the tangential and bending stress tensors, $\boldsymbol{N}$ and $\boldsymbol{M}$, respectively, and are constructed from their scalar components below.

$$\boldsymbol{N} = \begin{bmatrix} \boldsymbol{N}_1 & \boldsymbol{N}_2 \end{bmatrix} = \begin{bmatrix} N_{11} & N_{12} \\ N_{21} & N_{22} \end{bmatrix}$$

$$\boldsymbol{M} = \begin{bmatrix} \boldsymbol{M}_1 & \boldsymbol{M}_2 \end{bmatrix} = \begin{bmatrix} M_{11} & M_{12} \\ M_{21} & M_{22} \end{bmatrix}$$

The scalar components of the tangential stress tensor are composed of extensional and shear stresses in the plane of the web

$$N_{11} = K \left(\frac{\partial \delta_s}{\partial s} + \nu \frac{\partial \delta_t}{\partial t} \right) \tag{3.4}$$

$$N_{22} = K \left(\nu \frac{\partial \delta_s}{\partial s} + \frac{\partial \delta_t}{\partial t} \right) \tag{3.5}$$

$$N_{12} = N_{21} = \frac{K}{2} (1 - \nu) \left(\frac{\partial \delta_s}{\partial t} + \nu \frac{\partial \delta_t}{\partial s} \right) \qquad \text{where} \tag{3.6}$$

$$K = \frac{Eh}{1 - \nu^2}. \qquad \text{(Extensional Stiffness)} \tag{3.7}$$

Here δ_α is the displacement along the α-direction (for $\alpha = s, t$), while ν and E are the Poisson's ratio and modulus of elasticity of the material. The scalar components of the bending stress tensors are constructed from the rate of change of the surface's deflection angle along the surface

$$M_{11} = D \left(\frac{\partial \theta_s}{\partial s} + \nu \frac{\partial \theta_t}{\partial t} \right) \tag{3.8}$$

$$M_{22} = D \left(\nu \frac{\partial \theta_s}{\partial s} + \frac{\partial \theta_t}{\partial t} \right) \tag{3.9}$$

$$M_{12} = M_{21} = \frac{D}{2} (1 - \nu) \left(\frac{\partial \theta_s}{\partial t} + \frac{\partial \theta_s}{\partial t} \right) \qquad \text{where} \tag{3.10}$$

$$D = \frac{Eh^3}{12(1 - \nu^2)}. \qquad \text{(Bending Stiffness)} \tag{3.11}$$

Here, θ_α is the angle of deflection of the surface along the α-direction.

The angle of deflection is computed for small curvatures by the expression,

$$\theta_\alpha = \kappa_\alpha \delta_\alpha. \tag{3.12}$$

Here, $\kappa_\alpha{}^1$ is the curvature of the web in the plane defined by the two vectors $\hat{\boldsymbol{n}}$ and $\hat{\boldsymbol{t}}_\alpha$ shown in Figure 3.6, and computed by,

$$\kappa_\alpha = \hat{\boldsymbol{t}}_\alpha \hat{\boldsymbol{t}}_\alpha : \boldsymbol{\nabla}_{\mathrm{II}} \hat{\boldsymbol{n}}. \tag{3.13}$$

---

[1]The repeated indices in Equation 3.12 do not indicate a sum.

The surface gradient, $\boldsymbol{\nabla}_{\mathrm{II}}$, operates on the 2D surface in 3D space by subtracting the components that are orthogonal to the surface, for an arbitrary 3D field scalar, γ,

$$\boldsymbol{\nabla}_{\mathrm{II}}\gamma = \boldsymbol{\nabla} \cdot (\mathbf{I} - \hat{\boldsymbol{n}}\hat{\boldsymbol{n}})\gamma, \tag{3.14}$$

where $\mathbf{I}$ is the idemfactor, that is, the identity tensor. Similarly, the surface divergence $\boldsymbol{\nabla}_{\mathrm{II}}\cdot$ operates on the 2D surface in 3D space by likewise subtracting divergence components that are orthogonal to the surface, for an arbitrary 3D field vector, $\boldsymbol{\gamma}$,

$$\boldsymbol{\nabla}_{\mathrm{II}} \cdot \boldsymbol{\gamma} = \boldsymbol{\nabla} \cdot (\mathbf{I} - \hat{\boldsymbol{n}}\hat{\boldsymbol{n}}) \cdot \boldsymbol{\gamma}. \tag{3.15}$$

When the surface normal is the same as a basis vector of the 3D space, these operators simplify to the 2D versions given in the previous chapter (c.f. Equation 2.3).
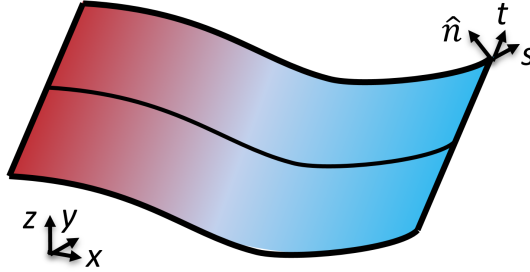
Figure 3.6: 3D shell domain for 2D differential equations in 3D space

This model for structural deformation is coupled to the two-phase flow model presented in Chapter 2. An approximate relationship couples gap thickness and deformation,

$$h = h_0 - \boldsymbol{\delta} \cdot \hat{\boldsymbol{n}}. \tag{3.16}$$

Here h_0 is the initial gap thickness and δ is the vector of displacement of the web from its initial position. The fluid pressure is used in the normal balance expression, accounting for atmospheric pressure on the back-side of the web,

$$F = P - P_{\mathrm{atm}} - S\sigma\kappa_m. \tag{3.17}$$

Here, $S\sigma\kappa_m$ is an average capillary pressure jump term, S limits the capillary effects to the gap fraction occupied by the liquid, σ is the surface tension between the gas and the liquid, and κ_m is the approximate curvature of the meniscus. In this work, the meniscus curvature is assumed to be controlled by the gap thickness, rather than the drop radii,

$$\kappa_m = \frac{1}{r_z} + \frac{1}{r_{\mathrm{II}}} \approx \frac{2}{h}, \tag{3.18}$$

where r_z and r_{II} are defined in Figure 3.7. The additional assumption that the fluid is perfectly wetting makes the final simplification for κ_m.

(a) Drop meniscus characterized by two radii

(b) Meniscus Exploded View
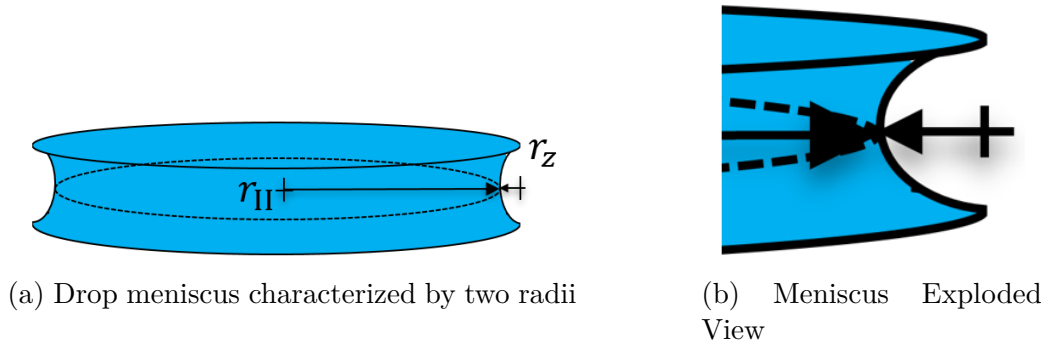
Figure 3.7: Drop meniscus radii

This coupled elastohydrodynamics model is applied to the study of the web deformation during gap filling against a rigid and featureless template. The problem description is depicted in Figure 3.8 in which a flat plate is pressed into a patch of drops, located on the central region of the free span. Figure 3.8 shows the dispense, imprint, flash and separation steps of the J-FIL process. The inkjet head dispenses the resist onto the web. Then, the web is translated under the imprint template. The tension of the web causes the template to be pressed against the web's central region, resulting in web deformation and merger of the drops. After the UV-cure, the stamp is separated from the solid resist and the web is translated forward. Several
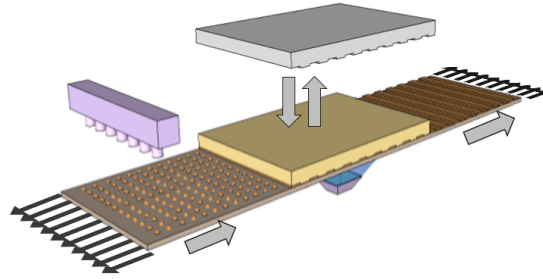
Figure 3.8: Diagram of imprint action on free-span, tensioned web.

perspective views of the final results of the simulations are presented in Figure 3.9 In this simulation the web has zero bending stiffness because attempts to use non-zero stiffness values resulted in unstable time evolution and perhaps non-physical results. Non-zero bending stiffnesses, resulted in asymmetric web deformation, likely due to errors in the implementation.

Two related features are the capillary-induced pinch of the gap near the web edge, and the pillow of liquid that has formed across the web. With zero bending stiffness, Equation 3.3 pressure is balanced by curved extension in each direction. Extensional stress in the direction that tension is applied, is larger than the other direction and the curvatures have the converse relationship. With smaller curvature in direction of tension, a relatively large curvature in the cross-web direction manifests as the wrinkling seen in Figures 3.9b and 3.9c.

The pinching induced by capillary forces results in a very narrow gap where viscous forces are increased, effectively trapping the liquid photoresist and preventing flow further outward to the edge of the web and impeding formation of a uniform layer. The sharp angle of the membrane at this pinch-point is not observed in experiments suggesting that bending stiffness could play a key role in achieving a more uniform fluid layer. It is unfortunate that simulations with non-zero bending stiffness did not prove to be stable, because they could shed light on this matter.

(a) Top-down perspective   (b) Diagram perspective   (c) In-line perspective
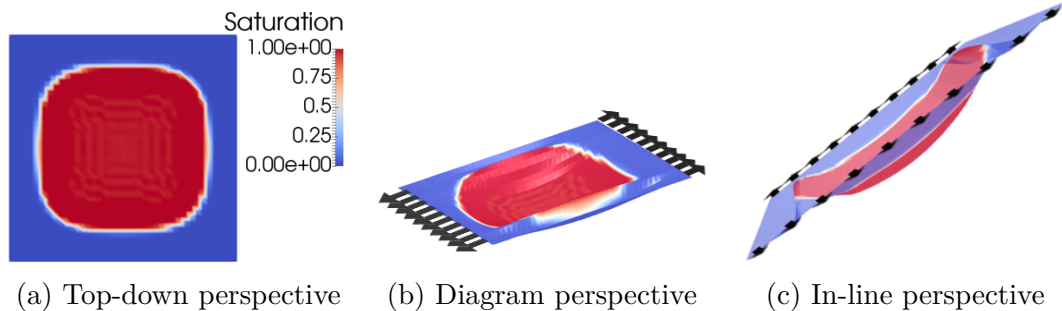
Figure 3.9: Several perspectives of the final time step of a simulation using the coupled two-phase flow and membrane mechanics model. Deformation is increased 1500 times in the axis that the stamp travels through.

This result re-enforces the approaches of process design that completely avoid unbacked imprint steps. It appears that some additional force is necessary to aid in spreading the fluid out to produce a uniform layer. To study the effects of bending stiffness on this pinching phenomena, a simplified structural model is pursued so that sources of instability may be more readily discovered and understood, thereby leading to workarounds. The next phase of model development is in a way a regression of capability, but it produces a simpler system overall in which sources of instability are easier to identify and so advances the basic understanding of the model.

3.2.2 Elastohydrodynamics on Two-dimensional Shells

In the system where the substrate is wrapped around the the NIL pattern roller, fluid layer thickness is governed by the interaction between pressure built up in the fluid by viscous resistance and forces acting through the tensioned web. At this point in the work, plug flow terms were included in the volume flux expression (c.f. Equations 2.4 and 3.20, marking the beginning the study of lubrication flow into a converging gap by tangential motion of the gap boundaries. The deformation of the web is modeled with of inextensible cylindrical shell theory[89][25]. The coupling of these

models enables study of layer thickness in rolling imprint modalities. The search for similar results revealed an unexpected link between this work and foil-bearing literature.

In the past, the study of foil-bearing theory provided better understanding of systems like magnetic tape readers and high speed thrust bearings. Foil-bearing theory predicts a region of uniformity where a lubrication layer separates a tensioned web from a circular roller. Rolling imprint processes can benefit from this uniform region during UV-cure because the fluid is under no/negligible shear stress, moreover, in the lab frame of reference a uniformly thick layer allows for longer residence time while curing. Besides revealing the region of uniformity, the models in the literature enable process designers to predict the effects of bending stiffness on the layer thickness. The model development in this section ties two-phase lubrication theory to a deformable web, the structure of which is controlled by stresses built-up in the substrate curvature. The resulting coupled, reduced-order model produces results with regions of uniformity comparable to those of foil-bearing theory. The role of bending stiffness in the formation of these uniform thickness regions is investigated. Some theoretical limits are established for curing the fluid in the region of uniformity.

The lubrication equations are reformulated with respect to a curvilinear coordinate, s, and according to a generic diagram of the flow domain is given in Figure 3.10. In NIL flow systems, the gap thickness is much less than the flow length, $h << L$, and the Reynolds number is also relatively small, $h\text{Re} << L$. Lubrication theory starts with the equation for mass conservation of a fluid in a thin, infinitely wide gap

$$\frac{\partial \rho h}{\partial t} + \frac{\partial}{\partial s}(\rho q) = 0, \tag{3.19}$$

where h is the gap thickness, q is the volumetric flux parallel to the reference plane with coordinate s, ρ is the fluid density and t is time. This work assumes that the vector direction of the coordinate s can vary, rotating along its path through the xy-plane, without any affect on lubrication equations. The volumetric flux has a
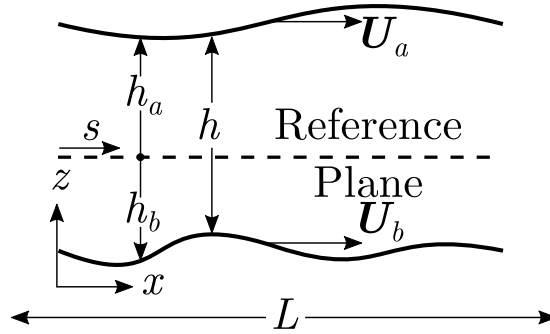
Figure 3.10: Lubrication domain with the moving mesh representing the web position.

plug flow contribution computed by the average of the two boundary velocities, and a Poiseuille flow contribution driven by the pressure gradient,

$$q = \frac{h(u_a + u_b)}{2} - \frac{h^3}{12\mu}\frac{\partial P}{\partial s}.$$ (3.20)

Here, u_a and u_b are the top and bottom boundary velocities tangent to the reference plane, μ is the dynamic viscosity of the fluid and p is the fluid pressure.[2]

The s-coordinate of Equation 3.19 measures the distance along a one-dimensional curvilinear domain, shown in Figure 3.11. The s-domain is discretized into shell elements for which the nodal positions are computed in terms of global Cartesian coordinates, x and y.

Motion of the web through the xy-plane is described by the sum of the base position of the web, $\boldsymbol{x}_0$ and the x-displacement field, $\boldsymbol{\delta}_x$, $\boldsymbol{x} = \boldsymbol{x}_0 + \boldsymbol{\delta}_x$, depicted in figure 3.12.

Because the substrate is thin, the cylindrical shell equations reduce model order of the structural mechanics. Cylindrical shell theory provides quasi-static, plane-stress equations describing the curvature of the web under tension, pressure and traction

---

[2]The full dimension versions of Equations 3.19 and 3.20 are derived in Chapter 2 as well as in Skip Scriven's course notes for ChEn 8101 at University of Minnesota, circa 1981-1989.
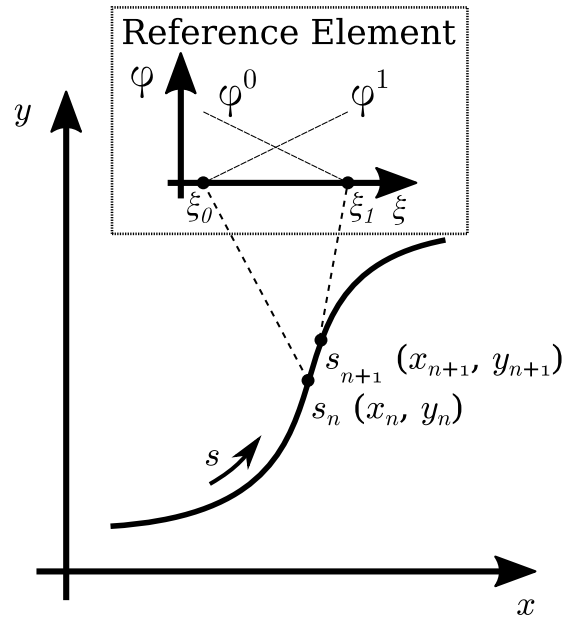
Figure 3.11: The curvilinear domain of s maintains a simple computational domain regardless of path through a Cartesian plane. Elements in s are mapped to the first order Lagrangian basis element, with basis functions ϕ.
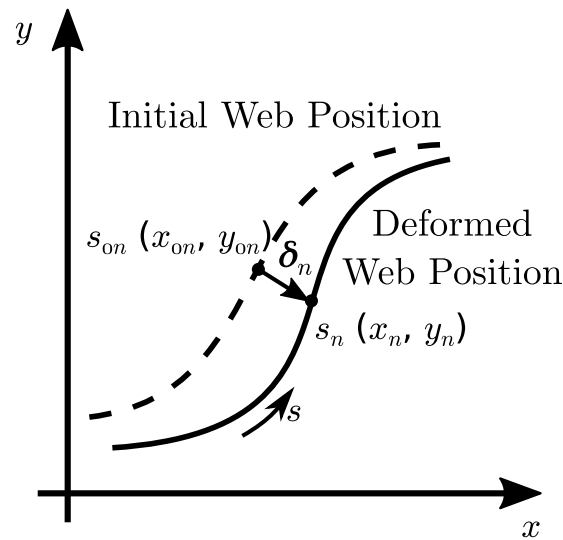
Figure 3.12: The curvilinear domain s moves from initial position s_0 through the non-moving xy-plane, tracked by the displacement vector δ.

forces. The tangential and normal stress balances are

$$\frac{\partial T}{\partial s} + \kappa \frac{\partial}{\partial s}(\kappa D) + P_t = 0 \tag{3.21}$$

$$-\frac{\partial^2}{\partial s^2}(\kappa D) + \kappa T + P_n = 0, \tag{3.22}$$

where κ is the curvature of the shell, P_t is traction, P_n is the normal stress and D is the bending stiffness[25]. The bending stiffness, $D \equiv Et^3/(12(1-\nu^2))$ is a function of the elastic modulus E, the shell thickness, t, and the Poisson ratio, ν. This model neglects the effects of liquid traction on the web, i.e. $P_t = 0$.

To account for mesh motion, the arbitrary Lagrangian Eulerian (ALE) method is implemented by also including geometric constraints on the position of the mesh. That is, the physical constraints of Equations 3.21 and 3.22 are supplemented by the differential form of the equation of a circle,

$$\frac{\partial^2 y}{\partial s^2} - \kappa \frac{\partial x}{\partial s} = 0. \tag{3.23}$$

Arbitrary mesh motion is made possible by an elliptic mesh control constraint with a linear coordinate potential as in the Laplace systems described by Thompson[113],

$$\frac{\partial^2 s}{\partial \xi^2} = 0. \tag{3.24}$$

Here, ξ is the distance along the reference element, as shown in Figure 3.11. This amounts to imposing the condition that each element has an equal arc-length.

The Equations of fluid (3.19) and structural mechanics (3.21 and 3.22) are coupled through the gap thickness and the fluid pressure. In theory, the gap thickness, h is the sum of h_a and h_b and is used in Equation 3.19, but to relate it to the moving mesh, the gap thickness is computed as the distance along the roller radius between the roller surface and the web,

$$h = r_w - r_r. \tag{3.25}$$

Here r_r is the roller radius and r_w is the distance between the web and the roller center. The tangential pressure acting on the web is assumed to be negligible. The difference between lubrication pressure and atmospheric pressure provides the effective normal pressures for Equation 3.22,

$$P_n = P - P_{\text{atm}}. \tag{3.26}$$

As presented in Chapters 1 and 2, NIL can be configured to use ink-jet dispensing of the liquid upstream of the imprint step. To extend the model here to accommodate this aspect, the approach of two-phase flow for NIL[32] is extended to domains with tangential boundary velocities. The relative permeabilities apply only to the Poiseuille terms while the lever-rule scalings are applied to the capacitive and Couette/plug-flow terms,

$$\frac{\partial Sh}{\partial t} + \frac{\partial}{\partial s}\left(h\bar{v}_l + Sh\frac{v_t + v_b}{2}\right) = 0 \tag{3.27}$$

$$\frac{\partial \rho_g (1-S)h}{\partial t} + \frac{\partial}{\partial s}\left(\rho_g h\bar{v}_g + \rho_g(1-S)h\frac{v_t + v_b}{2}\right) = 0. \tag{3.28}$$

Here, the saturation, S, is the local ratio of liquid volume to gap volume, ρ_g is the gas density and $\bar{v}_\alpha$ is the gap average velocity of the α-fluid phase. The α-fluid phase velocities are

$$v_\alpha = -\frac{h^2}{12\mu_\alpha}k_{r\alpha}\frac{\partial P}{\partial s}, \tag{3.29}$$

where μ_α is the bulk viscosity of the α-phase and $k_{r\alpha}$ is relative permeability of the α-phase. The relative permeabilities are addressed in more detail in previous work[32].

The mathematical model represented by Equations 3.19 implemented using the Galerkin finite-element method with Goma,[102][3] an open-source, multi-physics software for solving differential equations using finite-element method. A nuance of

---

[3]https://goma.github.io

working with this model arises in the construction of the mathematical weak form, amenable for solution with the finite element method. Usually the integrals are performed numerically with Gaussian quadrature[99]. The quadrature rules provide solutions to polynomial integrals over the reference element so a factor is needed to scale the size of the domain element to the reference element. Elements with the same dimension as that of the global coordinates have a square Jacobian of mapping matrix. Shell element domains have fewer computational dimensions than the continuum domain (c.f. Figure 3.11), and thus a rectangular Jacobian of mapping matrix, which does not have a determinant and thus no straightforward scaling factor. So an alternate method of computing the scaling factor is necessary. The scale factor is constructed from the arc-length formula to maintain lengths in the Euclidean sense. Dividing the arc-length formula by $\Delta\xi$, and then taking the limit as $\Delta\xi \to 0$ gives the scaling factor,

$$\frac{\partial s}{\partial \xi} = \sqrt{\left(\frac{\partial x}{\partial \xi}\right)^2 + \left(\frac{\partial y}{\partial \xi}\right)^2}. \tag{3.30}$$

Using this scaling factor in the weak form of Equation 3.24 results in a nonstandard simplification for numerical solution. The contribution of element e to residual i is

$$R_{ie} = \int_{\Omega_e} \phi^i \frac{\partial^2 s}{\partial \xi^2} \mathrm{d}s = \int_{\Omega_{\text{ref}}} \phi^i \frac{\partial^2 s}{\partial \xi^2} \frac{\partial s}{\partial \xi} \mathrm{d}\xi = \int_{\Omega_{\text{ref}}} \frac{1}{2} \phi^i \frac{\partial}{\partial \xi}\left[\left(\frac{\partial s}{\partial \xi}\right)^2\right] \mathrm{d}\xi, \tag{3.31}$$

for which, by divergence theorem the second derivative is eliminated,

$$R_{ie} = -\frac{1}{2}\left\{\int_{\Omega_{\text{ref}}} \frac{\partial \phi^i}{\partial \xi}\left(\frac{\partial s}{\partial \xi}\right)^2 \mathrm{d}\xi + \left[\phi^i|_{\xi_l}\left(\frac{\partial s}{\partial \xi}\bigg|_{\xi_l}\right)^2 - \phi^i|_{\xi_r}\left(\frac{\partial s}{\partial \xi}\bigg|_{\xi_r}\right)^2\right]\right\}. \tag{3.32}$$

Here, the two right-most terms are boundary terms that cancel out at inter-element boundaries, ξ_l and ξ_r are the left-most and right-most values of ξ on the reference element.

This model is used to simulate web deflection and lubrication fluid pressure in the translation a web partially wrapped around a cylindrical roller. Results are discussed next and compared to previous work by the foil-bearing community and with examples geared toward R2R NIL process design.

3.3 Results

Foil bearing theory provides a solid foundation for analysis of the results because the gap profile of these analyses reflect those observed in foil bearing analysis and experiments. Results from the model compare will with values from literature for perfectly flexible foil bearings as well as foil bearings with non-zero bending stiffness. Positing that the region of uniformity provides optimum conditions for UV-cure, a process window is developed with some theoretical limits on processing rates for perfectly flexible webs. The section wraps up with a demonstration that the coupled two-phase elastohydrodynamics model predicts that regions of uniformity might be made thinner by limiting the fluid entry to the inlet region with an ink-jet process.

The simulation domain consists of three segments, two of which require only the web-structure equations, while fluid and structure equations are solved where a lubrication layer exists between the roller and the web. The boundary conditions follow from the problem description. The idlers are treated as fixed points. The lubricated segment is bounded at the inflow and outflow by the condition of atmospheric pressure. The top and bottom tangential boundary velocities of the lubricated region are set to the same speed.

In foil bearing analysis and the rolling imprint analysis in Figure 3.13a, an entrance region turns into a region of uniformity before developing an exit region, shown in figure 3.13b. Both the entrance and exit region are thought of as transition regions, discussed further below. This behavior is mirrored between the plug flows

(a) Problem description diagram

(b) Three regions of the gap thickness in a foil bearing
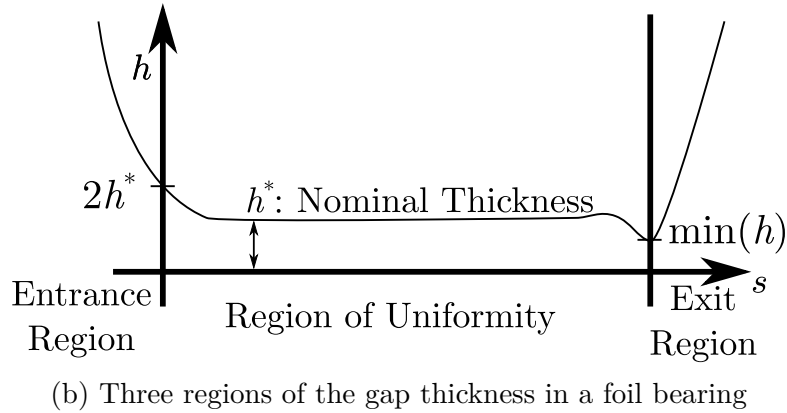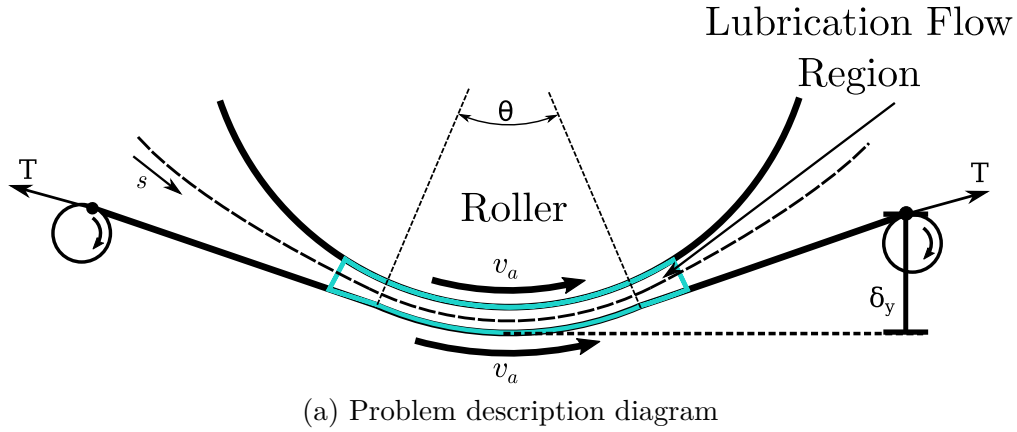
Figure 3.13: Problem description diagram and idealized gap thickness profile

in the NIL foil bearing and the Couette flows in the traditional foil bearing studies. To predict the length of the region of uniformity and its nominal thickness, a steady-state solution is obtained to a system with specified process speed, v_a, web tension per unit length, T, idler displacement, δ_y, bending stiffness, D, and fluid viscosity, μ. The foil-bearing number is computed from the process speed,

$$\epsilon = \frac{12 v_a \mu}{T}. \tag{3.33}$$

The result is analyzed to obtain nominal gap thickness, h^*, and the wrap angle, θ. The foil-bearing constant K appears as a dimensionless gap thickness and is

computed from simulations as

$$K = \frac{h^*}{r\epsilon^{\frac{2}{3}}}, \tag{3.34}$$

where h^* is the gap thickness at the center of the lubricated region, and v_a is the average velocity of the roller surface and web. In this work, the key dimensionless parameters are adopted from the foil-bearing literature. Wrap angle is usually reported as the normalized wrap angle Θ (Gross et al.[52]),

$$\Theta = \frac{\theta}{\epsilon^{\frac{1}{3}}}, \tag{3.35}$$

which represents the ratio of wrap angle, θ to the wrap angle of the transition region, $\epsilon^{(1/3)}$ [52]. θ is computed from the simulation as the roller angle that is spanned by the region of uniformity, bounded at the inlet by the point where the gap is twice the nominal thickness $(2h^*)$ and bound at the exit by the point where the gap thickness reaches its minimum, indicated in Figure 3.13.

The *stiffness parameter S_p*[4] can be thought of as the ratio of characteristic length to transition region length[52],

$$S_p = \frac{D}{Tr^2\epsilon^{\frac{2}{3}}}. \tag{3.36}$$

Here D is the *bending stiffness* and $D = Et^3/(12(1 - \nu^2))$. The bending stiffness is lumped parameter composed of the Young's modulus, E, the material thickness, t, and Poisson's ratio, ν. Comparisons between model and literature predictions of K, Θ and S_p relationships are in given in the next section.

Goma solves the system equations for steady-state solutions for the variables of web displacement, fluid pressure, tension and curvature. The hunting capability of Goma enables automation of the otherwise laborious process of obtaining a steady-state solution from an initial guess of a parametrically nearby steady-state solution.

---

[4]The literature uses just S for the stiffness parameter, but here, S_p is used to avoid confusion with the saturation variable.

Due to the highly non-linear behavior of this system, the first solution is computed for a near-zero wrap angle at a near-zero speed. First, the speed is ramped up from the initial guess value of 1 m/s to a specified level and second the idler position δ_y, is increased in y so as to wrap the web around the roller.

The model is first validated by comparing predicted dependence of K on Θ with those given be Gross et al.[52]. The values of $K(\Theta)$ for constant speeds are obtained by calculating both K and Θ along the hunting path that increases idler displacement. Several speeds are compared to the predicted relationship and presented in Figure 3.14. Values of Θ below eight correspond to glancing incidence wrap angles, and for these cases the inlet and exit regions have not yet fully developed to produce a region of uniformity(c.f. Figure 3.14b. The constant value of K for Θ above eight matches the expected value for perfectly flexible foil bearings. At the right side of of the plot, K drops off steeply indicating the lubrication domain no longer contains the inlet and exit regions (c.f. Figures 3.14 **c** and **d**). This means that the simulated domain is too short to contain the solution but that a longer simulation domain would allow the plot to extend further. Although this result validates the model, the boundary conditions might not be physical for NIL imprint systems that have much less fluid entering the gap. If the fluid is being cured, atmospheric pressure may not be appropriate for the outflow.

Figure 3.15 shows the variation of K with speed for a material with the stiffness equivalent to 3 mil thick mylar, providing some contrast to the insensitivity of K to speed and normalized wrap angle. This plot demonstrates that structural stiffness plays a role in both the formation of the region of uniformity as well as nominal gap thickness, but is still independent of the amount of wrap. The length of transition region scales with speed, so a faster speed should lead to later onset of wrap. Because of this, increasing speed reduces the normalized wrap angle. At lower speeds, lower thicknesses imply that less pressure is needed to balance the force of tension acting

(a) *K* vs. Θ at several speeds. Sub-figures **b** and **c** are taken at the points indicated by black circles on 0.001 cm/s plot.

(b) Gap at Θ ∼ 8 for 0.001 cm/s

(c) Gap at Θ ∼ 340 for 0.001 cm/s

(d) Gap at Θ ∼ 480 for 0.001 cm/s
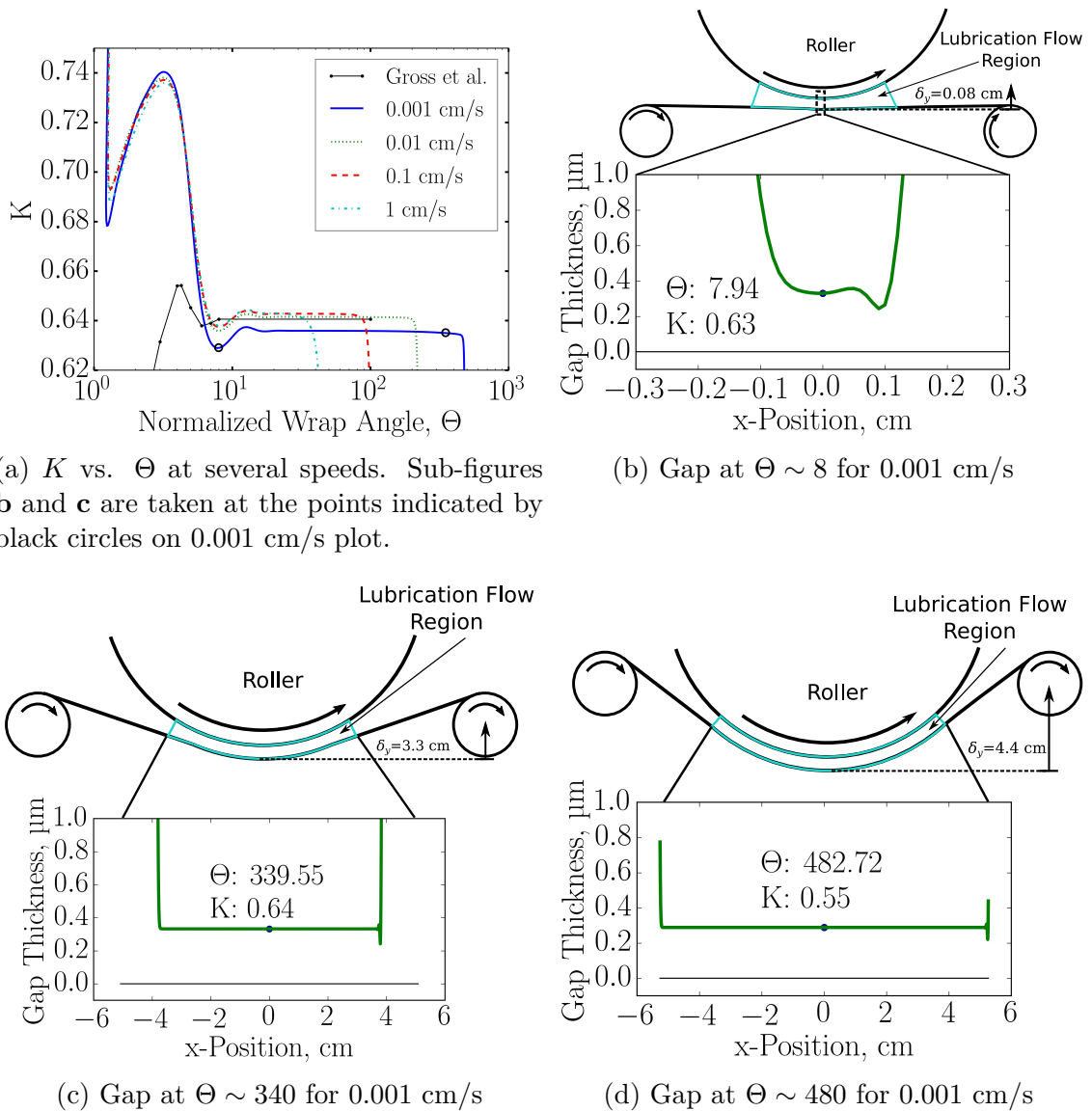
Figure 3.14: The values of K as a function of normalized wrap angle for different speeds.

through the web. So a reduced transition length seems to be what enables the thinner nominal thicknesses.

Including web stiffness also impedes steady-state solutions with regions of uni-
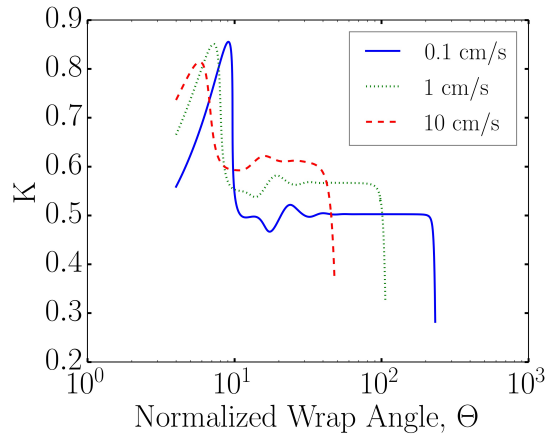
Figure 3.15: Plot of K vs Θ at several speeds for 3 mil thick mylar.

formity at the low speeds that are otherwise attainable without stiffness. This could be because the the web would bottom-out against the roller or the fluid isn't viscous enough to buildup the extra pressure needed to keep the web bent.

Gross et al.[52] provides a prediction for the relationship between K and the stiffness parameter S_p, included in Figure 3.16. Values of K for three thicknesses of mylar are obtained from the model and line-up together when plotted against the stiffness parameter. This line differs from the prediction presented by Gross et al.[52], perhaps because it is produced with the zeroth approximation solution presented by Eshel and Elrod[40]. The congruency of this model's predictions suggests there is a systematic difference between model Gross used to produce the plot and this model.

This shows that the model can be used to predict the length and the thickness of a region of uniformity for tensioned web NIL systems, and that foil-bearing theory can be brought to bear. A UV-cure processing window, presented in Figure 3.17, emerges as a result of this new application of foil-bearing theory. Because of the relationship between ϵ and the ratio of nominal gap thickness to roller radius, the process window suggests that thickness can be always be driven smaller for arbitrary materials by simply reducing the speed. Selecting a 50 nm thick region of uniformity
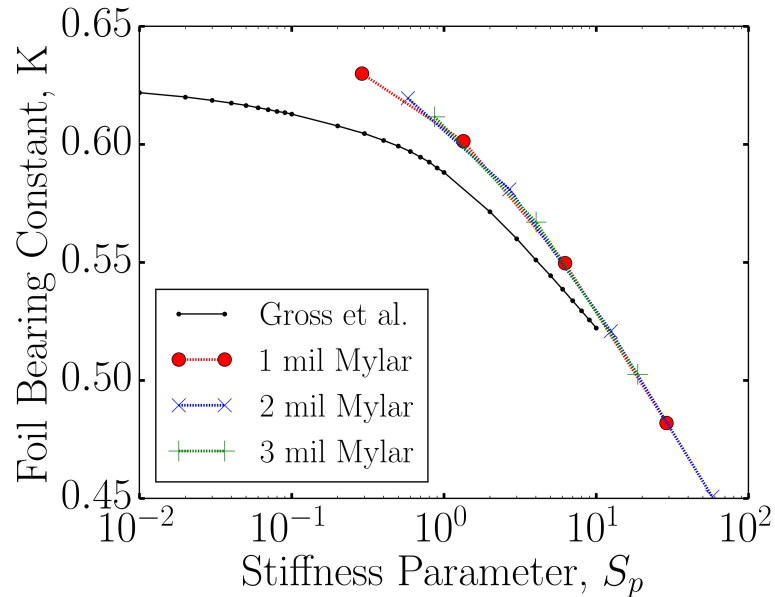
Figure 3.16: Plot of K vs S_p.

with a roller that is 5 cm in diameter sets the value of $\epsilon = 1.94e{-}9$ by Equation 3.34. With ϵ determined, resist viscosity ($\mu = 1$ cP) and web tension set the process speed (e.g. a 3 mil mylar membrane could support a maximum tension just above 10 kN/m). Now ϵ determines the web speed $v_a = 1.6$ mm/s by Equation 3.33. With ϵ defined for the system, the amount of time available for UV-exposure is determined by the roller radius, wrap angle and process speed, i.e. $\tau = \theta r/v_a$. The theoretical maximum exposure time is 196 s if the web is wrapped all the way around the roller. This process may not be feasible because the material may deform too much under this tension resulting in high strain in the web upon curing and tendency of the cured material to compress and collapse when the tension is relieved. Economics may still hamper this process because the rate of material production is too low. A one-cm-wide web traveling at 1.6 mm/s would produce only 60 cm^2 of patterned material per hour, roughly the value that Sreenivasan[112] reported to be the typical throughput for photonic crystals in 2008. Appendix B explores further the process of applying foil-bearing theory to system design. Although this presents
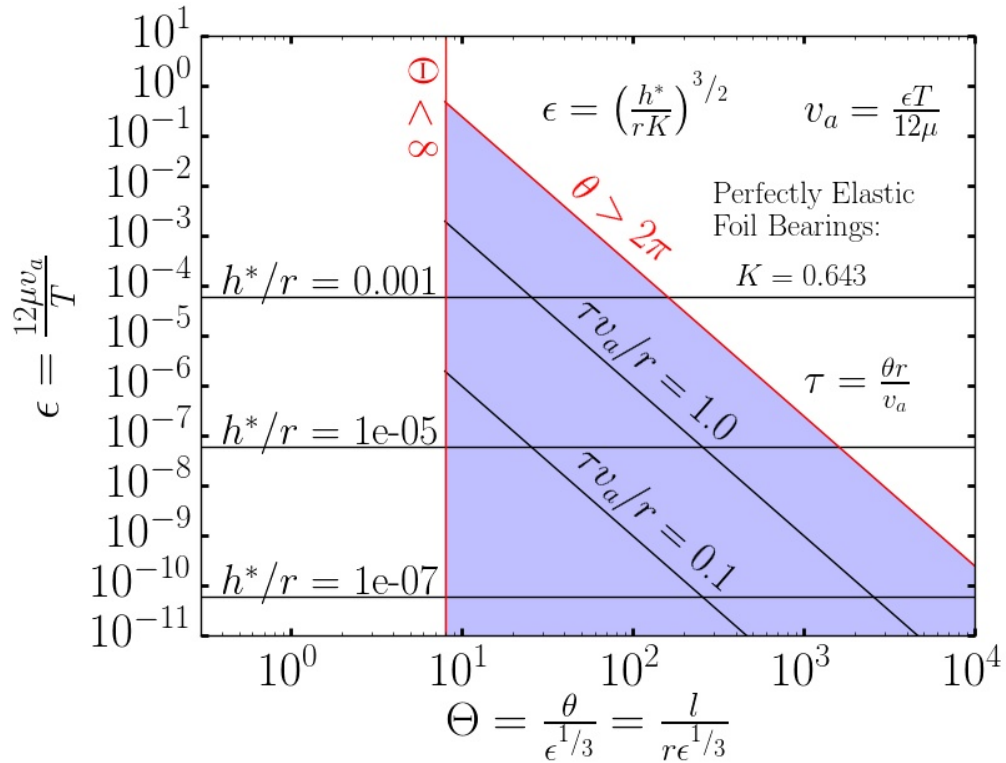
Figure 3.17: The shaded region covers the parameter space in which a region of uniformity exists and its length, l, is less than the circumference of the roller. The dwell time τ is the amount of time that a parcel of fluid spends in the region of uniformity. The lines of tv_a/r can be used to determine how much dwell time is available for UV-curing at constant gap.

an interesting opportunity for process design, the effects of bending stiffness remain to be incorporated into the diagram.

The amount of wrap provides some theoretical limits on the window for UV-cure, however, the challenge of finding a limit on the minimum achievable gap thickness remains. Although it appears the gap can be always be driven lower be reducing the processing rate, finding alternate ways to a thinner gap are more appealing from the product manufacturing point of view. Approaches like increasing pressure with an air-knife[67] or backing roll[7] can reduce gap thickness. Stronger materials support

higher tensions that drive thinner gaps. The model also suggests that reducing the photoresist viscosity can allow thinner regions of uniformity. This work examines how reduction of effective viscosity with two-phase flow of ink-jet systems can reduce gap thickness.

The results of incorporating the two-phase model by Equations 3.27 and 3.28 show a significant reduction in gap thickness. In this test case, the gas phase is simulated as though it were incompressible. Due to the increased non-linearity of the two-phase equations, a careful path must be taken to achieve a solution. The continuation capability of Goma reduces the viscosity from that of water (1 centiPoise) to that of air (0.000186 centiPoise) for the fluid supporting the wrapped solution in Figure 3.18a with particular web speed and idler displacement. The pressure and displacement fields initialize the solution for the transient two phase system and an additional boundary condition of non-zero saturation at the inlet to achieve the solution in Figure 3.18b. This simulation using a drop dispensing system to limit liquid inflow shows that thinner regions of uniformity can be achieved in these two-phase foil-bearing systems.

3.4   Conclusion

A reduced-order model for the elastohydrodynamics of R2R imprinting is developed. The initial results without bending stiffness agree with the expected foil-bearing behavior. Foil-bearing theory provides some insight into the operating window for UV-cure in the region of uniformity. A process design diagram communicates fundamental limitations of the process parameters. An example use case of the process design diagram demonstrates how to select process parameters for a nominal gap thickness of 50 nm, revealing practical processing-speed limitations of the process.

The study of bending stiffness shows that even with different stiffness, a single
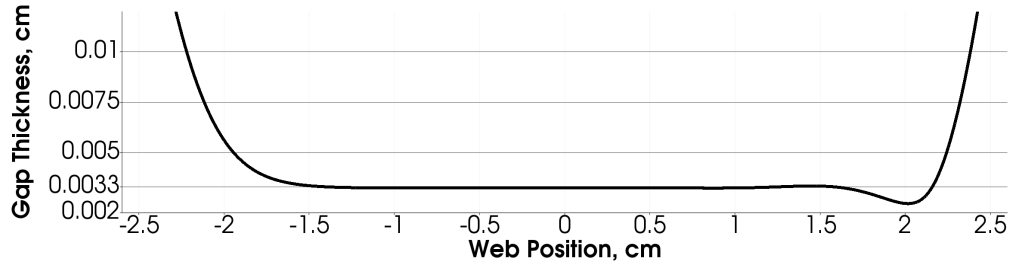
(a) Single-phase solution for water ($\mu = 1$ cP)
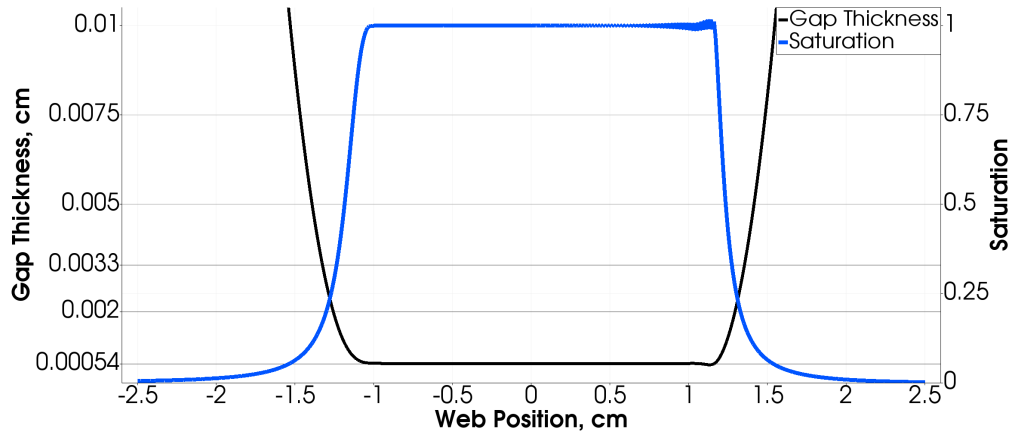
(b) Two-phase solution (Air: $\mu = 1.86\mathrm{e}-2$ cP & Water)

Figure 3.18: Limiting liquid inflow reduces the gap thickness for the same process speed and web tension. **(a)** Liquid viscosity: 1 cP. Nominal gap thickness: 33 µm. **(b)** Liquid viscosity: 1 cP. Gas viscosity: $1.86\mathrm{e}-2$ cP. Nominal gap thickness: 5.4 µm.

relationship between K and S_p determines the nominal gap thickness. The effects of bending stiffness also compare well but not exactly with the expected behavior presented in the literature.

The introduction of a second fluid of lesser viscosity to the entrance region subverts the power the foil-bearing number has over the nominal gap thickness. By feeding both gas and liquid into the entrance region, the viscosity is effectively decreased. This allows decreased nominal gap thickness for a foil bearing number computed from the liquid photoresist viscosity. The model demonstration is made

with an incomplete two-phase model, none of the effects that control gas dissolution rate are incorporated. While the thickness of a liquid layer produced by merger of drops can be determined *a-priori* simply from the liquid volume per area ratio, the drop merge is dependent on a variety of parameters that will influence the time available to cure the resist.

The effects of compressibility, dissolution parameters and drop dispense pattern also warrant further study to better understand how the region of uniformity responds to dissolution and for how a two-phase system will improve process feasibility. Besides the process aspects, the full 3D shell remains to be developed so as to study the capillary-elastohydrodynamics of a finite width web as inkjet drops merge in the gap.

This application of foil-bearing theory demonstrates that R2R imprint is possible within theoretical boundaries on wrap angle and processing rate. The revelation that there is a region of uniformity between a tensioned web and rotating roller begs the design of UV-cure R2R coating/imprint processes that benefit from the highly predictable thicknesses and minimized shear forces to be found there. The availability of validated predictive simulations for process design that include the elastohydrodynamics of two-phase foil bearings will also enable technical leaders to better inform decision makers of the potential business case for such processes.

3.5 Final Remarks

This thesis developed reduced-order models for fluid and structural mechanics relevant to the rolling-mode J-FIL. The model of fluid mechanics enables large area simulations that capture aggregate effects of tens of thousands of drops merging together. The coupled, reduced order model demonstrates the region of uniformity with highly predictable nominal thickness and low shear stresses making it an ideal

window for UV-curing. The end of this thesis by no means marks the end of what insights can be extracted from this vein of research. The knowledge gleaned from these models suggest many future direction for the work.

Better understanding of the limitation on minimum speed and how it relates to bending stiffness will further illuminate the theoretical limits on the process. Validation of the gas dissolution model also poses an area of possible research that will require experimental data so comparisons can be made that help identify model deficiencies so they can by understood and the model improved. A model that aggregates the dissolution of thousands of micron-scale gas pockets into an analytic approximation available at centimeter scale areas is ready to be incorporated into the coupled two-phase elastohydrodynamics model. Having identified some of the problems with coupling 2D structural mechanics with two-phase fluid mechanics, there are fewer barriers to implementing the 3D version of the model. Modeling phase change during UV-cure at the region of uniformity along with modeling the separation at the exit region perhaps represents completion of the modeling of a foil-bearing UV-cure coating process.

The limited perspective on minimum achievable thickness gained through this work suggests that these models may benefit micro-imprint systems[67] that are being used right now to create microfluidics systems which are being used to study micro sized electrical wires, as well as interesting microfluidics circuit elements[61]. The way capillary forces affect web deformation suggest that the influence of feature-filling[75][28] on the formation of the residual layer warrants further study and this may be achieved by coupling a feature-filling model with the model developed in this thesis. Combining a structural flow model with the suggested foil-bearing UV-cure coating process would complete the set of models that describe the physical system discussed in this thesis.

The goal of enabling the dissemination of nanotechnology and predicting the

region of uniformity highlights the paramount value of a project to build the foil-bearing imprint system. The system may then be used with the models developed in this thesis in a complete process design-and-build cycle, enabling the identification of specific problem that will drive the next steps of model development. This cycle of modeling, simulation and experimentation enables the understanding and development of such complex systems and each practice informs and refines the others.

Appendices

Appendix A

Reynolds Lubrication

In this section, scaling analysis develops Reynolds lubrication approximation. Hele-Shaw[56] demonstrated the remarkably simple flow in such thin-gaps with dye tracers in flow through a thin gap, depicted by cartoon in Figure A.1a. Integration of the lubrication approximation through the thin gap between NIL template and substrate reduces the dimensionality of the equations.

A.1   Scaling Analysis

Lubrication theory issues from the scaling analysis of the steady, incompressible Navier-Stokes and continuity equations with a geometric requirement and a dynamic requirement[38]. To specify these requirements several parameters need to first be described. The Reynolds number describes the ratio of inertial forces to viscous forces and is computed,

$$\mathrm{Re} = \frac{\rho l v}{\mu}, \tag{A.1}$$

Appendix A. Reynolds Lubrication

(a) Thin-gap perspective view showing streamlines around an obstacle.

(b) Thin-gap profile view showing length and velocity labels.
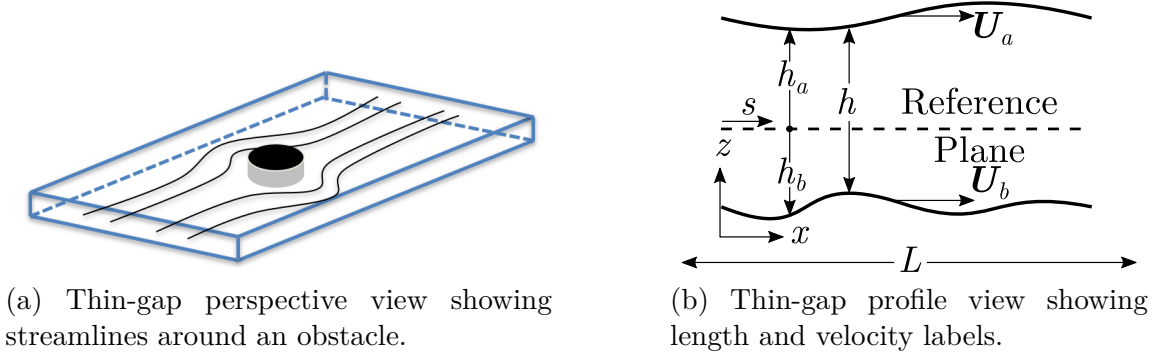
Figure A.1: Two perspectives of a thin-gap

where l is the characteristic length of the system, v is the characteristic speed of the fluid and ρ and μ are respectively the density and viscosity of the fluid.

The geometric requirement of lubrication theory is that the gap thickness, h, is much less than the gap length, L,

$$\frac{h}{L} << 1. \tag{A.2}$$

And the dynamic requirement constraints the Reynolds number with respect to this thickness-length ratio,

$$\mathrm{Re}\frac{h}{L} << 1. \tag{A.3}$$

For incompressible fluids, the continuity equation describes conservation of mass as

$$\frac{\partial u_x}{\partial x} + \frac{\partial u_y}{\partial y} + \frac{\partial u_z}{\partial z} = 0. \tag{A.4}$$

The steady, three-dimensional Navier-Stokes equations describe transport of momentum

$$\rho \left(u_x \frac{\partial u_x}{\partial x} + u_y \frac{\partial u_x}{\partial y} + u_z \frac{\partial u_x}{\partial z} \right) = -\frac{\partial P}{\partial x} + \mu \left(\frac{\partial^2 u_x}{\partial x^2} + \frac{\partial^2 u_x}{\partial y^2} + \frac{\partial^2 u_x}{\partial z^2} \right) \tag{A.5a}$$

$$\rho \left(u_x \frac{\partial u_y}{\partial x} + u_y \frac{\partial u_y}{\partial y} + u_z \frac{\partial u_y}{\partial z} \right) = -\frac{\partial P}{\partial y} + \mu \left(\frac{\partial^2 u_y}{\partial x^2} + \frac{\partial^2 u_y}{\partial y^2} + \frac{\partial^2 u_y}{\partial z^2} \right) \tag{A.5b}$$

$$\rho \left(u_x \frac{\partial u_z}{\partial x} + u_y \frac{\partial u_z}{\partial y} + u_z \frac{\partial u_z}{\partial z} \right) = -\frac{\partial P}{\partial z} + \mu \left(\frac{\partial^2 u_z}{\partial x^2} + \frac{\partial^2 u_z}{\partial y^2} + \frac{\partial^2 u_z}{\partial z^2} \right). \tag{A.5c}$$

Appendix A. Reynolds Lubrication

Here $\mathbf{v} = (u_x, u_y, u_z)$ is the velocity of the fluid and P is the pressure.

Scaling analysis under the conditions in Equations A.2 and A.3 provides a model with substantially reduced complexity. Non-dimensional variables, denoted by the breve ($\breve{\ }$) bring out the fundamental relationships that control the magnitudes of the derivatives. The tilde, $\sim$ is used in these relationships to indicate the terms on either side are of similar orders of magnitude thus removing the strict equality of the =-sign. The non-dimensional velocities are defined in terms of velocity scales, U in the x and y directions and V in the z direction,

$$\breve{u}_x \sim \frac{u_x}{U}, \tag{A.6}$$

$$\breve{u}_y \sim \frac{u_y}{U} \text{ and} \tag{A.7}$$

$$\breve{u}_z \sim \frac{u_z}{V}. \tag{A.8}$$

$$\tag{A.9}$$

The non-dimensional lengths are also defined in terms of length scales, L in the x and y directions and h in the z direction,

$$\breve{x} \sim \frac{x}{L}, \tag{A.10}$$

$$\breve{y} \sim \frac{y}{L} \text{ and} \tag{A.11}$$

$$\breve{z} \sim \frac{z}{h}. \tag{A.12}$$

Non-dimensional derivatives are easily found by employing the chain rule as per the following operation,

$$\frac{\partial \breve{u}_x}{\partial \breve{x}} \sim \frac{\partial \breve{u}_x}{\partial u_x} \frac{\partial u_x}{\partial x} \frac{\partial x}{\partial \breve{x}} \sim \frac{L}{U} \frac{\partial u_x}{\partial x}. \tag{A.13}$$

The geometric constraint then applied to the scaled form of the continuity equation yields the first insight of lubrication theory,

$$\frac{U}{L} \frac{\partial \breve{u}_x}{\partial \breve{x}} + \frac{U}{L} \frac{\partial \breve{u}_y}{\partial \breve{y}} + \frac{V}{h} \frac{\partial \breve{u}_z}{\partial \breve{z}} \sim \frac{2U}{L} + \frac{V}{h} \sim 0 \text{ or} \tag{A.14}$$

$$\frac{V}{2U} \sim \frac{V}{U} \sim \frac{h}{L} << 1. \tag{A.15}$$

Appendix A. Reynolds Lubrication

Here continuity informs us that in cases where the gap is much thinner than it is long, the velocity along the length of the gap must far outweigh the velocity in the direction of gap-width.

Before re-writing the z-component of momentum transport in terms of non-dimensional variables, the pressure must be non-dimensionalized. In the NIL flow system, viscous solutions are meant to fill the gap completely and the inertia of the fluid plays little role in this process. Thus, flow restriction by viscous drag is of primary concern, and to capture this effect, the viscous pressure scaling $\breve{P} = P\mu U/h$, is employed. Here the length scale h and the velocity scale U are used specifically to capture the relationship between pressure and viscous drag in the Poisuelle-like flow. Equation A.5c, is re-written in terms of the non-dimensionalized variables,

$$\rho \left(\frac{UV}{L} \breve{u}_x \frac{\partial \breve{u}_z}{\partial \breve{x}} + \frac{UV}{L} \breve{u}_y \frac{\partial \breve{u}_z}{\partial \breve{y}} + \frac{V^2}{h} \breve{u}_z \frac{\partial \breve{u}_z}{\partial \breve{z}} \right) \sim$$
$$-\frac{\mu U}{h^2} \frac{\partial \breve{P}}{\partial \breve{z}} + \mu \left(\frac{V}{L^2} \frac{\partial^2 \breve{u}_z}{\partial \breve{x}^2} + \frac{V}{L^2} \frac{\partial^2 \breve{u}_z}{\partial \breve{y}^2} + \frac{V}{h^2} \frac{\partial^2 \breve{u}_z}{\partial \breve{z}^2} \right) \tag{A.16}$$

Replacing V with the scaled Uh/L and multiplying both sides by h^2,

$$\rho U^2 h \frac{h^2}{L^2} \left(\breve{u}_x \frac{\partial \breve{u}_z}{\partial \breve{x}} + \breve{u}_y \frac{\partial \breve{u}_z}{\partial \breve{y}} + \breve{u}_z \frac{\partial \breve{u}_z}{\partial \breve{z}} \right) \sim$$
$$-\mu U \frac{\partial \breve{P}}{\partial \breve{z}} + \mu \frac{h}{L} \left(\frac{h^2}{L^2} \frac{\partial^2 \breve{u}_z}{\partial \breve{x}^2} + \frac{h^2}{L^2} \frac{\partial^2 \breve{u}_z}{\partial \breve{y}^2} + \frac{\partial^2 \breve{u}_z}{\partial \breve{z}^2} \right) \tag{A.17}$$

In this form it is easy to see that all terms except $\partial \breve{P}/\partial \breve{z}$ scale out of the equation, since $h/L << 1$. Furthermore with no other terms of appreciable scale, the change of pressure in the y direction is neglible,

$$\frac{\partial \breve{P}}{\partial \breve{z}} \sim 0, \tag{A.18}$$

making pressure a function of x and y only.

Appendix A. Reynolds Lubrication

Re-writing the x-component in terms of non-dimensionalized variables and re-arranging to find which terms dominate the expression for $\partial \breve{P}/\partial \breve{x}$,

$$-\frac{\partial \breve{P}}{\partial \breve{x}} \sim \rho \frac{Uh}{\mu} \left(\breve{u}_x \frac{\partial \breve{u}_x}{\partial \breve{x}} + \breve{u}_y \frac{\partial \breve{u}_x}{\partial \breve{y}} + \breve{u}_z \frac{\partial \breve{u}_x}{\partial \breve{z}} \right) - \left(\frac{h}{L} \frac{\partial^2 \breve{u}_x}{\partial \breve{x}^2} + \frac{h}{L} \frac{\partial^2 \breve{u}_x}{\partial \breve{y}^2} + \frac{L}{h} \frac{\partial^2 \breve{u}_x}{\partial \breve{z}^2} \right).$$
(A.19)

Immediately the terms with a factor of h/L can be dropped, and two terms remain on the right-hand side of Equation A.19

$$-\frac{\partial \breve{P}}{\partial \breve{x}} \sim \mathrm{Re} \left(\breve{u}_x \frac{\partial \breve{u}_x}{\partial \breve{x}} + \breve{u}_y \frac{\partial \breve{u}_x}{\partial \breve{y}} + \breve{u}_z \frac{\partial \breve{u}_x}{\partial \breve{z}} \right) - \frac{L}{h} \frac{\partial^2 \breve{u}_x}{\partial \breve{y}^2}.$$
(A.20)

For the viscous forces in this system, h is the characteristic length and U is the characterstic speed, so $\rho U h/\mu = \mathrm{Re}$ and the dynamic constraint describes which of the remaining terms dominates. From Equation A.3, $\mathrm{Re} << L/h$,

$$\frac{\partial \breve{P}}{\partial \breve{x}} \sim \frac{L}{h} \frac{\partial^2 \breve{u}_x}{\partial \breve{y}^2}.$$
(A.21)

This process applied to the y-direction reveals the similar dominant effect of $\partial^2 \breve{u}_y/\partial \breve{z}^2$ on $\partial \breve{P}/\partial \breve{y}$. Having determined these dominant terms, Equations A.5a,b and c are simplified for thin-gaps of Figure A.2 with small enough Reynolds number as,

$$\frac{\partial P}{\partial x} = \mu \frac{\partial^2 u_x}{\partial z^2}$$
(A.22)

$$\frac{\partial P}{\partial y} = \mu \frac{\partial^2 u_y}{\partial z^2}$$
(A.23)

$$\frac{\partial P}{\partial z} = 0.$$
(A.24)

Reynolds lubrication theory simplifies the general 3D Navier-Stokes equations for thin-gap flow[92] providing the first step in model-order reduction for modeling drop merger in NIL. This result illustrates that the pressure field is directly dependent on the velocity tangent to the gap-plane and suggests that a 2D expression may be found to further reduce the order of the model.
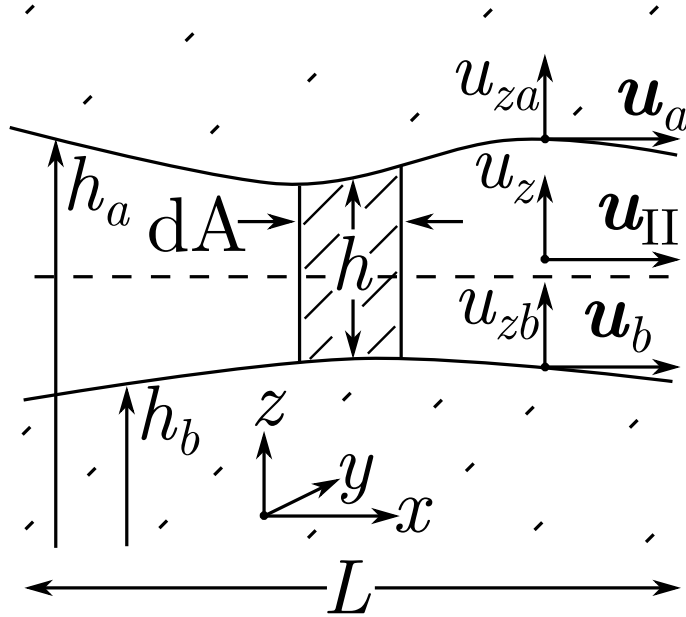
Figure A.2: Diagram of the important variables in thin-gap flow analysis

A.2   Obtaining 2D Equations

Three-dimensional velocity fields within the gap are obtained by integrating Equations A.22 and A.23 through the gap thickness for the boundary conditions

$$
\begin{aligned}
z = h_a \quad u_x = U_{xa} \quad u_y = U_{ya} \quad u_z = \frac{dh_a}{dt} \ \text{and} \\
z = h_b \quad u_x = U_{xb} \quad u_y = U_{yb} \quad u_z = \frac{dh_b}{dt}.
\end{aligned} \tag{A.25}
$$

The z-motion of the gap boundaries is computed for a frame that is not moving with respect to the base coordinate system. Under the conditions in A.25 the terms of the continuity equation (A.4) are integrated through the gap, but judicious attention to Leibniz's rule is necessary to properly switch the integrals and derivatives,

$$
\int_{z=h_b}^{h_a} \frac{\partial u_x}{\partial x} \mathrm{d}z = \frac{\partial}{\partial x} \int_{z=h_b}^{h_a} u_x \mathrm{d}z - u_x|_{h_a} \frac{\partial h_a}{\partial x} + u_x|_{h_b} \frac{\partial h_b}{\partial x}. \tag{A.26}
$$

Appendix A. Reynolds Lubrication

The total derivatives of the z-components of the boundary velocities are expanded about the boundary points in terms of their partial derivatives so the integral may capture the complete effects of boundary motion,

$$\frac{dh_a}{dt} = \frac{\partial h_a}{\partial t} + \frac{\partial h_a}{\partial x}\frac{\partial x}{\partial t} + \frac{\partial h_a}{\partial y_a}\frac{\partial y_a}{\partial t} = \frac{\partial h_a}{\partial t} + U_{xa}\frac{\partial h_a}{\partial x} + U_{ya}\frac{\partial h_a}{\partial y} \quad \text{and} \quad (A.27)$$

$$\frac{dh_b}{dt} = \ldots \qquad\qquad = \frac{\partial h_b}{\partial t} + U_{xb}\frac{\partial h_b}{\partial x} + U_{yb}\frac{\partial h_b}{\partial y} \quad . \qquad (A.28)$$

The gap boundary heights are not a function of z, so Leibniz's rule is not applied to the $\partial u_z/\partial z$ component,

$$\int_{z=h_b}^{h_a} \frac{\partial u_z}{\partial z}\mathrm{d}z = u_z|_{h_a} - u_z|_{h_b} \qquad (A.29)$$

$$= \frac{\partial h_a}{\partial t} + U_{xa}\frac{\partial h_a}{\partial x} + U_{ya}\frac{\partial h_a}{\partial y} - \frac{\partial h_b}{\partial t} - U_{xb}\frac{\partial h_b}{\partial x} - U_{yb}\frac{\partial h_b}{\partial y} \qquad (A.30)$$

The gap-parallel vectors (represented by the II subscript) are separated from the gap-orthogonal components,

$$\boldsymbol{u}_{\mathrm{II}} = u_x\hat{\boldsymbol{x}} + u_y\hat{\boldsymbol{y}}$$
$$\boldsymbol{\nabla}_{\mathrm{II}} = \frac{\partial}{\partial x}\hat{\boldsymbol{x}} + \frac{\partial}{\partial y}\hat{\boldsymbol{y}} \qquad (A.31)$$
$$\boldsymbol{U}_a = U_{xa}\hat{\boldsymbol{x}} + U_{ya}\hat{\boldsymbol{y}}$$
$$\quad \text{et cetera}$$

The continuity equation is re-assembled in terms of the vector expressions in A.31

$$\int_{z=h_b}^{h_a} \boldsymbol{\nabla}_{\mathrm{II}} \cdot \boldsymbol{u}_{\mathrm{II}}\mathrm{d}z = \boldsymbol{\nabla}_{\mathrm{II}} \cdot \int_{z=h_b}^{h_a} \boldsymbol{u}_{\mathrm{II}}\mathrm{d}z - \boldsymbol{U}_a \cdot \boldsymbol{\nabla}_{\mathrm{II}}h_a + \boldsymbol{U}_b \cdot \boldsymbol{\nabla}_{\mathrm{II}}h_b \quad \text{and} \quad (A.32)$$

$$\int_{z=h_b}^{h_a} \frac{\partial u_z}{\partial z}\mathrm{d}z = \frac{\partial h}{\partial t} + \boldsymbol{U}_a \cdot \boldsymbol{\nabla}_{\mathrm{II}}h_a - \boldsymbol{U}_b \cdot \boldsymbol{\nabla}_{\mathrm{II}}h_b \quad \text{so} \quad (A.33)$$

$$0 = \int_{z=h_b}^{h_a} \frac{\partial u_x}{\partial x} + \frac{\partial u_y}{\partial y} + \frac{\partial u_z}{\partial z}\mathrm{d}z = \frac{\partial h}{\partial t} + \boldsymbol{\nabla}_{\mathrm{II}} \cdot \int_{z=h_b}^{h_a} \boldsymbol{u}_{\mathrm{II}}\mathrm{d}z \qquad (A.34)$$

where the gap thickness is the difference between the gap boundary heights, $h = h_a - h_b$ Defining he volumetric flux parallel to the gap-plane $\boldsymbol{q}$,

$$\boldsymbol{q} = \int\limits_{z=h_b}^{h_a} \boldsymbol{u}_{\mathrm{II}}\mathrm{d}z \tag{A.35}$$

allows for the integrated continuity equation to be expressed as the equation for the change of volume in the gap between the bounding surfaces:

$$\frac{\partial h}{\partial t} + \boldsymbol{\nabla}_{\mathrm{II}} \cdot \boldsymbol{q} = 0. \tag{A.36}$$

Now the volumetric flowrate can be expressed in terms of the boundary velocities and gap thickness if the integral in Equation A.35 is carried out.

$$\boldsymbol{q} = -\underbrace{\frac{h^3}{12\mu}\boldsymbol{\nabla}_{\mathrm{II}}P}_{\substack{\text{Poiseuille flow} \\ \text{contribution}}} + \underbrace{h\frac{\boldsymbol{U}_a + \boldsymbol{U}_b}{2}}_{\substack{\text{Plug flow} \\ \text{contribution}}} . \tag{A.37}$$

Thus the steady, incompressible and three-dimensional Navier-Stokes equations are simplified to a set of two-dimensional equations expressing volume conservation as a relationship between changing gap height and the pressure field. The gap-average velocity is computed simply by dividing the volumetric flowrate by the gap height,

$$\boldsymbol{v} = \frac{\boldsymbol{q}}{h}. \tag{A.38}$$

Appendix B

UV-Cure Window Formulae

Foil-bearing theory provides guidance in the design of NIL process by enabling determination of, h^*, the nominal gap thickness and τ, the time available for cure. For perfectly elastic foil bearing systems, important material properties include E, the Young's modulus of the web, t, the thickness of the web and μ, the viscosity of the fluid. Parameters of the process; rate, v_a, roller radius, r, web tension (per unit length), T, and wrap angle, θ determine the process outcomes.

The following procedure reveals how the constraints of maximum extensional strain of the web, ϵ_{smax}, and fluid viscosity define the relationship between roller radius and processing speed for a specified web material. Recall the equation for the foil bearing constant, ϵ, is

$$\epsilon = \frac{12\mu v_a}{T}. \tag{B.1}$$

Recall the equation for the nominal gap thickness is

$$h^* = Kr\epsilon^{2/3}. \tag{B.2}$$

Here, perfect flexibility of the web is assumed, setting the value of $K = 0.643$[52]. Under plane-stress assumptions, the stress on the web in the direction of tension, σ,

Appendix B. UV-Cure Window Formulae

is related to web thickness and web tension as,

$$\sigma t = T. \tag{B.3}$$

From mechanics of materials,

$$\sigma = \epsilon_s E, \tag{B.4}$$

here, ϵ_s is extensional strain, or change in web length, Δl, per web length, l. Simplifying Equations B.1, B.2, B.3 and B.4 gives,

$$h^* = 0.643r \left(\frac{12\mu v_a}{\epsilon_{smax} Et} \right)^{2/3}. \tag{B.5}$$

This expression provides the expected nominal thickness based on material properties, processing parameters and extensional strain. The strain of the web during UV-Cure needs to be considered if the tension in the web is to be released. Release of the tension will cause the web to shrink, putting a compressive stress on the pattern where it is adhered to the web. This should be planned for because it may result in change of shape of the pattern, or at worst, the stress differential at the web-resist interface may lead to de-adhesion of the pattern.

The time available for cure is determined from the processing rate, roller radius and wrap angle achieved by the equipment,

$$\tau = \frac{\theta r}{v_a}, \tag{B.6}$$

here, θ, is in radians and is related to the wrap length l by $r\theta = l$. Since the process utilizes a circular roller, a hard maximum for θ is 2π. Although, some of the arc of the roller will be used in the transition regions so wrap angle of 2π cannot be achieved in practice. In order to have time for cure, there needs to be non-zero length to the region of uniformity. Comparisons of foil-bearing theory with simulations show that the region of uniformity exists above a normalized wrap angle of 8, putting the

Appendix B. UV-Cure Window Formulae

constraint on the foil-bearing number,

$$\epsilon < \frac{l}{8r}^3 .$$

(B.7)

These constraints are depicted in the design space of foil-bearing number and normalized wrap angle by red lines in Figure B.1.
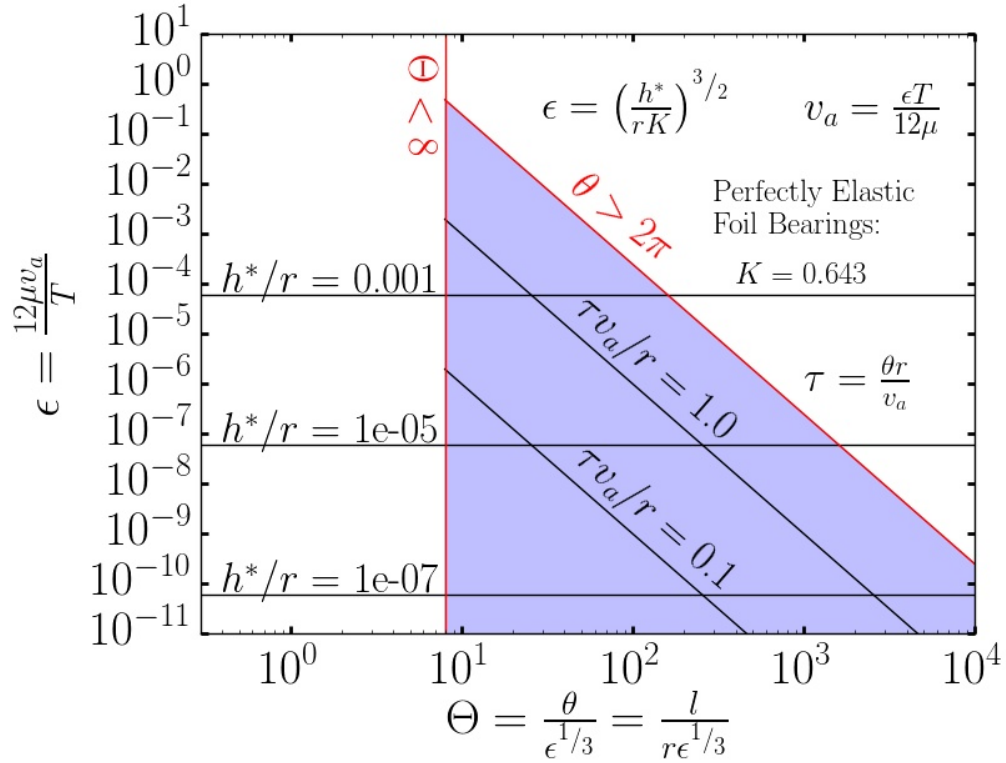
Figure B.1: UV-Cure processing window.

The vertical axis in Figure B.1 has two scales, ϵ and h^*/r related by Equation B.2. Designing a process around the desired gap thickness will require balancing a higher velocity against a reduction of the roller radius. A smaller radius and high velocity will result in a shorter process window for UV-cure. Higher tension can increase the roller radius for the same desired gap thickness, as well as increase the amount of time available for UV-cure. However increased tension will also increased strain

between the web and pattern. Evaluating how this limits the process is a question of whether the tension will be relieved from the web, or on how well the pattern and substrate interface holds up under the strain involved. If strain isn't a limiting factor, then certainly, the strength of the web will limit the amount of tension that can be applied, as materials will fail or yield plastically under high tension.

Suppose the fluid viscosity is 1 centipoise, the design tension is 10 N/m and the roller radius is 5 cm,

$$h^* = 0.643(5 \ [\text{cm}]) \left(\frac{12(1 \ [\text{centipoise}])v_a}{10 \ [\text{N/m}]} \right)^{2/3} \tag{B.8}$$

$$= 3.215 \ [\text{cm}] \left(\frac{0.12 \ [\text{g/cm/s}]v_a}{10000 \ [\text{g/s/s}]} \right)^{2/3} \tag{B.9}$$

$$= 0.001685 v_a^{2/3}, \tag{B.10}$$

where v_a is given in cm/s and h^* is in cm. In this scenario, a gap thickness of 10 nm requires a speed of $1.45(10)^{-5}$ cm/s. If, however, the tension is 1000 N/m, the 10 nm gap requires a processing speed of $1.45(10)^{-3}$ cm/s. A tension of 100000 N/m would give a 10 nm gap for a processing speed of 1.45 mm/s. A strong enough material would support this tension, or the roller radius could be reduced for the 10 nm gap.

A roller radius of 1 cm, tension of 10000 N/m with the same viscosity would produce a 10 nm gap with a processing speed of 1.6 mm/s, and $\epsilon = 1.94(10)^{-9}$ This foil-bearing number has a wide range in Figure B.1. The theoretical max wrap angle of 2π gives maximum cure window of 39 s.

Bibliography

[1] Qing Wang and Hiroshi Hiroshima. "Effects of environmental gas in UV nano-imprint on the characteristice of UV-curable resin". In: *Japanese Journal of Applied Physics* 49 (2010).

[2] Shrawan Singhal et al. "Inkjet-based deposition of polymer thin films enabled by a lubrication model incorporating nano-scale parasitics". In: *Physics of Fluids* 25 (2013).

[3] M. Colburn et al. "Step and flash imprint lithography: a new approach to high-resolution patterning". In: *Proceedings of SPIE*. Emerging Lithographic Technologies III. 1999.

[4] Gerard M. Schmid et al. "Jet and flash imprint lithography for the fabrication of patterned media drives". In: *Proceedings of SPIE*. Photomask Technology. 2009.

[5] Wei Zhang et al. "High throughput jet and flash imprint lithopgraphy for semiconductor memory applications". In: *Proceedings of SPIE*. Alternative Lithographic Technologies VIII. 2016.

[6] Hayden Taylor. "Defectivity prediction for droplet-dispensed UV nanoimprint lithography, enabled by fast simulation of resin flow at feature, droplet, and template scales". In: *Proceedings of SPIE*. Vol. 9777. Alternative Lithographic Technologies VIII. 2016.

[7]   Sean Ahn et al. "Roll-to-roll nanopatterning using jet and flash imprint lithography". In: *Proceedings of SPIE*. Vol. 8323. 2012.

[8]   Paras Ajay et al. "Multifield sub-5 nm overlay in imprint lithography". In: *Journal of Vacuum Science and Technology B* 34 (6 2016).

[9]   A. Almqvist and J. Dasht. "The homogenization process of the Reynolds equation describing compressible liquid flow". In: *Tribology International* 39 (2005), pp. 994–1002.

[10]   J.-C. Bacri et al. "Miscible viscous fingering experiments versus continuum approach". In: *Physics of Fluids A: Fluid Dynamics* 4 (8 1992), pp. 1611–1619.

[11]   Derek William Basset. "Fluid management in immersion and imprint lithography". University of Texas at Austin, 2010.

[12]   Jacob Bear. *Dynamics of fluids in porous media*. Dover, 1972.

[13]   Jacob Bear and Y. Bachmat. *Introduction to modeling transport phenomena in porous media*. Springer Netherlands, 1990.

[14]   Dean Francis Benjamin. "Roll coating flows in multiple roll systems". University of Minnesota, 1994.

[15]   H. Blok and J. J. vanRossum. "The foil bearing - A new departure in hydrodynamic lubrication". In: *Lubrication Engineering* 9 (1953), pp. 310–320.

[16]   Joseph J. M. Braat, Albert Smid, and M. M. B. Wijnakker. "Design and production technology of replicated aspheric objective lenses for optical disk systems". In: *Applied Optics* 24 (12 1985), pp. 1853–1855.

[17]   J. U. Brackbill, D. B. Kothe, and C. Zemach. "A continuum method for modeling surface tension". In: *Journal of Computational Physics* 100 (1992), pp. 335–354.

[18]   Scott F. Bradford and Nikolaos D. Katapodes. "The anti-dissipative, non-monotone behavior of Petrov-Galerkin upwinding". In: *International Journal for Numerical Methods in Fluids* 33 (2000), pp. 583–608.

[19]   G. Bradski. "The OpenCV Library". In: *Dr. Dobb's Journal of Software Tools* (2000). accessed 2017-07-27. URL: `http://www.drdobbs.com/open-source/the-opencv-library/184404319` (visited on 07/27/2017).

[20]   Christopher E. Brennen. *Fundamentals of Multiphase Flows*. accessed 2017-07-27. Cambridge University Press, 2005, pp. 20–21. URL: `http://authors.library.caltech.edu/25021/2/cabook.pdf` (visited on 07/27/2017).

[21]   Alexander N. Brooks and Thomas J.R. Hughes. "Streamline upwind/Petrov-Galerkin formulations for convection dominated flows with particular emphasis on the incompressible Navier-Stokes equations". In: *Computer Methods in Applied Mechanics and Engineering* 32 (1982), pp. 199–259.

[22]   Alexandre Caboussat. "Numerical simulation of two phase free surface flows". In: *Archives of Computational Methods in Engineering* 12 (2 2005), pp. 165–224.

[23]   Richard Allan Cairncross. "Solidification phenomena during drying of sol-to-gel coatings". University of Minnesota, 1994.

[24]   Richard A. Cairncross et al. *Drying in Deformable Partially-Saturated Porous Media: Sol-Gel Coatings*. Tech. rep. SAND96-2146. Sandia National Laboratories, 1996.

[25]   M. S. Carvalho. "Elastohydrodynamics of tensioned web roll coating process". In: *International Journal Multiphase Flow* 41 (2003), pp. 561–576.

[26]   Marcio S. Carvalho and Haroon S. Keshgi. "Low-flow limit in slot coating: Theory and experiments". In: *AIChE Journal* 46 (10 2000), pp. 1907–1917.

[27]   Jeff Chappell. "EUVL: The Clear NGL Frontrunner". In: *Electronic News* (Feb. 2002).

[28]   Siddharth Chauhan et al. "Feature filling modeling for step and flash inprint lithography". In: *Journal of Vacuum Science & Technology B* 27 (4 2009), pp. 1926–1932.

[29]   Yongsuk Choi et al. "Monolithic Metal Oxide Transistors". In: *ACS NANO* 9 (4 2015), pp. 4288–4295.

[30]   Stephen Y. Chou, Peter R. Krauss, and Preston J. Renstrom. "Imprint of sub-25 nm vias and trenches in polymers". In: *Applied Physics Letters* 67 (12 1995), pp. 3114–3116.

[31]   Stephen Y Chou, Peter R Krauss, and Preston J Renstrom. "Nanoimprint Lithography". In: *Journal of Vacuum Science and Technology B* 14 (1996), pp. 4129–4133.

[32]   Andrew Cochrane et al. "Multiphase model for nanoimprint lithography". In: *International Journal of Multiphase Flow* 104 (2018), pp. 9–19.

[33]   Matthew Colburn. "Step and flash imrpint lithography a low pressure, room temperature nanoimprint lithography". University of Texas at Austin, 2001.

[34]   Matthew Colburn et al. "Ramifications of lubrication theory on imprint lithography". In: *Microelectronic Engineering* 75 (2004), pp. 321–329.

[35]   France A. Córdova. *Remarks by Dr. France A. Córdova, Director, National Science Foundation, AAAS Forum on Science and Technology Policy, US Initiatives Advancing the Frontiers of Science & Policy Innovation, June 22, 2018.* 2018. URL: https://www.nsf.gov/news/speeches/cordova/18/fc180622_aaaspolicyforum.jsp (visited on 01/14/2019).

[36]   Dennis J. Coyle. "Knife and roll coating". In: *Liquid Film Coating.* Ed. by S. F. Kistler and P. M. Scweizer. Chapman & Hall, 1997.

[37] Luis Cueto-Felgueroso and Ruben James. "A phase-field model of two-phase Hele-Shaw flow". In: *Journal of Fluid Mechanics* 758 (2014), pp. 522–552.

[38] William M. Deen. *Analysis of Transport Phenomena.* Oxford University Press, 1998.

[39] K. S. Ducotey and J. K. Good. "The importance of traction in web handling". In: *Journal of Tribology* 117 (1995), pp. 679–684.

[40] A. Eshel and Jr. H. G. Elrod. "Stiffness effects on the infinitely wide foil bearing". In: *Journal of Lubrications Technology* 89 (1967), pp. 92–97.

[41] A. Eshel and Jr. H. G. Elrod. "The theory of the infinitely wide, perfectly flexible, self-acting foil bearing". In: *Journal of Basic Engineering* 87 (4 1965), pp. 831–836.

[42] Stephen D. Fantone. "Replicating optical surfaces using UV curing cements: a method". In: *Applied Optics* 22 (6 1983), p. 764.

[43] James Q. Feng. "Computational analysis of slot coating on a tensioned web". In: *AIChE Journal* 44 (10 1998), pp. 2137–2143.

[44] Richard P. Feynman. "There's plenty of room at the bottom". In: *Engineering and Science* 23 (5 1960), pp. 22–36.

[45] Fir0002Flagstaffotos. *Female Golden Stag Beetle.* [Online: accessed February 27th, 2019]. URL: https://commons.wikimedia.org/wiki/File:Female_Golden_Stag_Beetle.jpg.

[46] M. Fourar and S. Bories. "Experimental study of air-water two-phase flow through a fracture (narrow channel)". In: *International Journal of Multiphase Flow* 21 (4 1995), pp. 621–637.

[47] M. Fourar, S. Bories, and R. Lenormand. "Experimental study of two-phase flow in rough fractures". In: *Seventeenth Workshop on Geothermal Reservoir Engineering.* 1992, pp. 215–218.

[48]   M. Fourar, C. Moyne, and R. Lenormand. "A theoretical model for relative permeabilities in two-phase flow in a fracture". In: *Computational Methods in Water Resources XII. Computational Methods in Surface and Ground Water Transport.* Ed. by V. N. Burganos et al. 1998, pp. 159–166.

[49]   Marianne M. Francois et al. "A balanced-force algorithm for continuous and sharp interfacial surface tension models within a volume tracking interface". In: *Journal of Computational Physics* 213 (2006), pp. 141–173.

[50]   P. H. Gaskell et al. "A mathematical model of roll-to-web kiss coating". In: *Chemical Engineering Research & Design* 76 (A1 1998), pp. 29–37.

[51]   Pierre-Gilles de Gennes. "Theory of slow biphasic flows in porous media". In: *PhysicoChemical Hydrodynamics* 4 (2 1983), pp. 175–185.

[52]   William A. Gross et al. *Fluid Film Lubrication.* United States of America: John Wiley & Sons, Inc., 1980.

[53]   Jan Haisma et al. "Mold-Assisted Nanolithography: A process for Reliable Pattern Replication". In: *Journal of Vacuum Science and Technology B* 14 (1996), pp. 4124–4128.

[54]   W. J. Harrison. "The Hydrodynamical theory of lubrication with special reference to air as a lubricant". In: *Transactions of the Cambridge Philosophical Society* 22 (1913), pp. 39–54.

[55]   Juan C. Heinrich and Derry Connolly. "Three-dimensional finite element analysis of self-acting foil bearings". In: *Computer Methods in Applied Mechanics and Engineering* 100 (1992), pp. 31–43.

[56]   Henry Selby Hele-Shaw. "The Flow of Water". In: *Nature* 58 (1898), pp. 34–36.

[57] Irene Heo. *Why does AMOLED need polarizers?* 2014. URL: `https://techn ology.ihs.com/509943/why-all-amoled-is-applying-polarizer-supp liers-of-amoled-polarizer-and-compensation-film-for-polarizer- technology-trend-of-amoled-use-polarizer`.

[58] Hiroshi Hiroshima, Masaru Nakagawa Yoshihiko Hirai, and Shinji Matsui. "Innovative nanoimprint lithography using PFP condensible gas". In: *Journal of Photopolymer Science and Technology* 26 (1 2013), pp. 87–96.

[59] H. Howden and J. A. Clarke. "Refracting Replica Aspheric Optics". In: *Optical Engineering* 15 (6 1976), pp. 197–201.

[60] Alfred Hubler. *Arrays of synthetic atoms: Nanocapacitor batteries with large energydensity and smalle leak currents.* Tech. rep. AD1043094. Air Force Research Laboratory, 2017.

[61] Woo Jin Hyun et al. "Open-channel microfluidic diodes based on two-tier juntions". In: *applied Physics Letters* 113 (2018), p. 193701.

[62] ITRS. *ITRS Overview.* Tech. rep. International Technology Roadmap for Semiconductors, 2015. URL: `https : / / www . dropbox . com / s / 6eskh6bwdcuzpsa/1507_11_Paolo%20verview_Out.pdf?dl=0`.

[63] ITRS. *Lithography technology working group white paper.* Tech. rep. International Technology Roadmap for Semiconductors, 2014. URL: `https://www. dropbox.com/sh/8jaob1jtmkugw7d/AADdL9m8hirVFqa489-rydiaa/2014% 20ITRS%202.0%20ITWG%20White%20Papers?dl=0&preview=1_2014+ITRS+ 2.0_Lithography_R1.pdf&subfolder_nav_tracking=1`.

[64] Akhilesh Jain and Roger T. Bonnecaze. "Fluid management in roll-to-roll nanoimprint lithography". In: *Journal of Applied Physics* 113 (2013).

[65] Akhilesh Jain, Andrew Spann, and Roger T. Bonnecaze. "Effect of droplet size, droplet placement, and gas dissolution on throughput and defect rate in UV nanoimprint lithography". In: *Journal of Vacuum Science and Technology B* 35 (1 2016).

[66] Akhilesh Jain et al. "Fluid flow in UV nanoimprint lithography with patterned templates". In: *Microelectronic Engineering* 173 (5 2017), pp. 62–70.

[67] Krystopher S. Jochem et al. "High-resolution, high-aspect-ratio printed and plated metal conductors utilizing roll-to-roll microscale UV-imprinting with prototype imprinting stamps". In: *Industrial & Engineering Chemistry Research* 57 (48 2018), pp. 16335–16346.

[68] Matthew Kincaid. "Investigation of roll-to-roll nanoimprinting process utilizing inkjet based resist deposition". MA thesis. University of Texas at Austin, 2011.

[69] Stephan F. Kistler. "The fluid mechanics of curtain coating and related vsicous free surface flows with contact lines". University of Minnesota, 1983.

[70] Kenneth L. Knox and Thomas L. Sweeney. "Fluid effects associated with web handling". In: *Industrial & Engineering Chemistry Process Design and Development* 10 (2 1971), pp. 201–205.

[71] Nazrin Kooy et al. "A review of roll-to-roll nanoimprint lithography". In: *Nanoscale Research Letters* 9 (2014), p. 320.

[72] Vera Kratochvil. *Blue Morpho Butterfly*. URL: `https://www.publicdomainpictures.net/en/view-image.php?image=7275&picture=blue-morpho-butterfly` (visited on 03/01/2019).

[73] B. P. Leonard and H. S. Niknafs. "Sharp monotonic resolution of discontinuities without clipping of narrow extrema". In: *Computers & Fluids* 19 (1991), pp. 141–154.

[74]   Wen-Di Li, Wei Wu, and Richard Stanley Williams. "Combined helium ion beam and nanoimprint lithography attains 4nm half-pitch dense patterns". In: *Journal of Vacuum Science and Technology B* 30 (6 2012), 06F304-1 – 06F304-4.

[75]   Xiaogan Liang et al. "Air bubble formation and dissolution in dispensing nanoimprint lithography". In: *Nanotechnology* 18 (4 2007), pp. 1926–1932.

[76]   L. Licht. "An experimental study of elastohydrodynamic lubrication of foil bearings: Part 1 - Displacement in the central zone". In: *Journal of Lubrication Technology* 90 (1 1968), pp. 199–220.

[77]   R. W. Lockhart and R. C. Martinelli. "Proposed correlation of data for isothermal two-phase two-component flow in pipes". In: *Chemical Engineering Progress* 45.1 (1949), pp. 39–48.

[78]   J. T. S. Ma. "An investigation of self-acting foil bearings". In: *Journal of Basic Engineering* 87 (4 1965), pp. 837–846.

[79]   Anastassios Mavrokefalos et al. "Efficient light trapping in inverted nanopyramid thin crystalline solicon membranes for solar cell applications". In: *Nanoletters* 12 (2011), pp. 2792–2796.

[80]   Raymond P. Mayer and Robert A. Stowe. "Mercury porosimetry - breakthrough pressure for penetration between packed spheres". In: *Journal of Colloid Science* 20 (1965), pp. 893–911.

[81]   Jeffrey Morse et al. *Nanofabrication technologies for roll-to-roll processing.* Tech. rep. NIST-National Nanomanufacturing Network, 2011.

[82]   R Nave. *Oil film interference.* [Online: accessed October 18th, 2018]. 2018. URL: http://hyperphysics.phy-astr.gsu.edu/hbase/phyopt/oilfilm.html.

[83] Stanley Osher and James A. Sethian. "Fronts propogating with curvature dependent speed Algorithms based on Hamilton-Jacobi formulations". In: *Journal of Computational Physics* 79 (1988), pp. 12–49.

[84] Vegar Ottesen. [Online: accessed March 25th, 2019] CC BY 3.0. URL: `https://commons.wikimedia.org/w/index.php?curid=16957521`.

[85] T. C. Papanastasiou, N. Malamataris, and K. Ellwood. "A new outflow boundary condition". In: *International Journal for Numerical Methods in Fluids* 14 (1992), pp. 587–608.

[86] Janghoon Park, Keehyun Shin, and Changwoo Lee. "Roll-to-roll coating technology and its applications: A review". In: *International Journal of Precision Engineering and Manufacturing* 17 (2016), pp. 1–14.

[87] Linfa Peng et al. "Study on bubble defect in roll-to-roll UV imprinting process for micropyramid arrays. II. Numerical Study". In: *Journal of Vacuum Science & Technology B* 34 (2 2016), pp. 2166–2746.

[88] Kristin Pfeiffer et al. "Antireflection coatings for strongly curved glass lenses by atomic layer deposition". In: *Coatings* 7 (8 2017), p. 118.

[89] Ferdinand Ruprecht Pranckh. "Elastohydrodynamics in coating flows". University of Minnesota, 1989.

[90] Shravanthi Reddy and Roger T. Bonnecaze. "Simulation of fluid flow in the step and flash imprint lithography process". In: *Microelectronic Engineering* 82 (2005), pp. 60–70.

[91] Douglas J. Resnick, S. V. Sreenivasan, and C. Grant Wilson. "Step & flash imprint lithography". In: *Materials Today* February (2005), pp. 34–42.

[92] Osbourne Reynolds. "On the Theory of Lubrication and Its Application to Mr. Beauchamp Tower's Experiments, Including an Experimental Determination

of the Viscosity of Olive Oil". In: *Philosophical Transactions of the Royal Society of London* 177 (1886), pp. 157–234.

[93] Scott A. Roberts and P. Randall Schunk. "A reduced-order model for porous flow through thin, structured materials". In: *International Journal of Multiphase Flow* 67 (2014), pp. 25–36.

[94] Scott A. Roberts et al. "Multiphase hydrodynamic lubrication flow using a three-dimensional shell finite element model". In: *Computers & Fluids* 87 (2013), pp. 12–25.

[95] Evgenii S. Romm. *Fluid flow in fractured rocks.* [english trans. William R. Blake (1972)]. Moscow, Russia: Nedra Publishing House, 1966.

[96] Harry D Rowland and William P King. "Polymer deformation and filling modes during microembossing". In: *Journal of Micromechanics and Microengineering* 14 (2004), pp. 1625–1632.

[97] Harry D Rowland et al. "Impact of polymer film thickness and cavity size on polymer flow during embossing: towards process design rules for nanoimprint lithography". In: *Journal of Micromechanics and Microengineering* 15 (2005), pp. 2414–2425.

[98] Harry D Rowland et al. "Simulations of Nonuniform Embossing: The Effect of Asymmetric Neighbor Cavities on Polymer Flow During Nanoimprint Lithography". In: *Journal of Vacuum Science and Technology B* 23 (2005), pp. 2958–2962.

[99] P. A. Sachinger, P. R. Schunk, and R. R. Rao. "A Newton-Raphson pseudo-solid domain mapping technique for free and moving boundary problems: A finite element implementation". In: *Journal of Computational Physics* 125 (1996), pp. 83–103.

BIBLIOGRAPHY

[100] P. G. Saffman and F.R.S. Sir Geoffrey Taylor. "The penetration of a fluid into a porous medium or Hele-Shaw cell containing a more viscous liquid". In: *Proceedings of the Royal Society, Series A* 245 (1958), pp. 312–329.

[101] Luigi Sartor. "Slot coating: fluid mechanics and die design". University of Minnesota, 1990.

[102] P. R. Schunk et al. *Goma 6.0 - A Full-Newton Finite Element Program for Free and Moving Boundary Problems with Coupled Fluid/Solid Momentum, Energy, Mass and Chemical Species Transport: User's Guide.* Tech. rep. SAND2013-1844. Sandia National Laboratories, 2013.

[103] Robert Bruce Secor. "Operability of extensional rheometry by stagnation, squeezing and fiber-drawing flows: Computer-aided-analysis, viscoelastic characterization and experimental analysis". University of Minnesota, 1988.

[104] Kosta S. Selinidis et al. "Mask replication using jet and flash imprint lithography". In: *Journal of Micro/ Nanolithography, MEMS, and MOEMS* 10 (4 2011).

[105] Tatiana Sergen et al. "Measurement and modeling of Optical Performance of Wire Grids and Liquid-Crystal Displays Utilizing Grid Polarizers". In: *Journal of the Optical Society of America A* 19 (2002), pp. 1872–1885.

[106] Young Jae Shin. "Wire grid polarizer by angled deposition method using nanoimprint lithography". University of Michigan, 2014.

[107] Marcio da Silveira Carvalho. "Roll coating flows in rigid and deformable gaps". University of Minnesota, 1996.

[108] Lovejeet Singh et al. "Defect reduction of high-density full-field patterns in jet and flash imprint lithography". In: *Journal of Micro/Nanolithography, MEMS, and MOEMS* 10 (3 2011).

BIBLIOGRAPHY

[109] Shrawan Singhal, Ravikiran Attota, and S.V. Sreenivasan. "Residual layer thickness control and metrology in jet and flash imprint lithography". In: *Proceedings of SPIE*. Vol. 8324. 2012.

[110] skitterphoto.com. [Online: accessed February 27th, 2019]. URL: `https://www.pexels.com/photo/abalone-abstract-background-blue-375158/`.

[111] Werner Soedel. *Vibration of Shells and Plates*. New York: Marcel Dekker, Inc., 1981.

[112] S. V. Sreenivasan. "Nanoscale manufacturing enabled by imprint lithography". In: *MRS Bulletin* 33 (9 2008).

[113] Joe F. Thompson, Z. U. A Warsi, and C. Wayne Mastin. *Numerical Grid Generation Foundations and Applications*. New York, United States of America: Elsevier Science Publishing Co., Inc., 1985.

[114] Kazuyuki Usuki et al. "Design considerations for ultraviolet nanoimprint lithography resists". In: *Journal of Micro/Nanolithography, MEMS and MOEMS* 11 (3 2012).

[115] Banqiu Wu. "Next Generation Lithography for 22 and 16 nm Technology Nodes and Beyond". In: *Science China Information Sciences* 54 (5 2011), pp. 959–979.

[116] S. Wurm, F. Goodwin, and H. Yun. "EUVL Readiness for Pilot Line Insertion". In: *Solid State Technology* (Feb. 2009).

[117] R. D. Wyckoff and H. G. Botset. "The flow of gas-liquid mixtures through unconsolidated sands". In: *Journal of Applied Physics* 7 (1936), pp. 325–345.

[118] Shinya Yoshioka. *Scientific Image - Blue Morpho Butterfly Wing Microribs*. URL: `http://www.nisenet.org/catalog/scientific-image-blue-morpho-butterfly-wing-microribs` (visited on 03/01/2019).

[119] César Zarcone and Roland Lenormand. "Experimental determination of viscous coupling during two-phase flow in porous media". In: *Physics of Fluids A: Fluid Dynamics* 4 (8 1992), pp. 1611–1619.

[120] Olgierd Cecil Zienkiewicz and Robert L. Taylor. *The Finite Element Method.* Butterworth-Hienemann, 2000, pp. 474–476.